2-D Melting in Excimer-Laser Irradiated Polycrystalline Silicon Films

Vernon Keith Wong

Submitted in partial fulfillment of the
requirements for the degree
of Doctor of Philosophy
in the Graduate School of Arts and Sciences

COLUMBIA UNIVERSITY

2021

ABSTRACT

2-D Melting in Excimer-Laser Irradiated Polycrystalline Silicon Films

Vernon Keith Wong

This thesis examines the excimer-laser-induced melting of ELA-prepared silicon films using in situ transient reflectance and transmission analysis. The results clearly show that these polycrystalline films, which consist of columnar grains in contact with SiO_2, can melt in a largely and remarkably 2-D manner. Based on the presently and previously obtained experimental results, as well as considering the thermal, thermodynamic, and kinetic aspects of the melting-transition-relevant details, we suggest a model that consists of grain-boundary-initiated melting, followed by lateral melting proceeding into the transiently superheated interior of the grains. Additional experiments are performed which demonstrate how this 2-D melting behavior at least stems intrinsically from the presence in the material of melt-prone grain boundaries and superheating-permitting Si/SiO_2 interfaces.

Next, the phase and temperature evolutions of the irradiated films are investigated using a numerical simulation program, which incorporates key material, thermodynamic, and kinetic parameters. We find that the center portion of the grains

during (partial) melting (1) corresponds to, especially at the SiO_2-passivated surface, the hottest regions of the films during rapid heating, and (2) remains entirely solid throughout the thickness of the film, as the maximum temperature sustained in these unmelted solids remains well below the superheating limit of silicon at the Si/SiO_2 interface.

Lastly, we discuss, and substantiate with results obtained from numerical simulations, the role that the manifested dimensionality of melting plays in dictating the efficiency with which the ELA crystallization technique can generate microstructurally uniform polycrystalline materials. The current discovery regarding the 2-D nature of melting should be recognized and appreciated as a critical process-enabling element for ELA, as the scenario permits microstructure evolution of the grains to take place in an effective manner.

Table of Contents

List of Figures

Acknowledgments

I would like to thank several people who have given me their support over the past few years and have helped to make my time studying at Columbia University a wonderful experience. For your encouragement, generosity, and kindness, I am greatly indebted to you all. The creation of this thesis was made possible by our combined efforts.

First, I thank Professor James Im whose command of the technical matter and remarkable ability to teach will never cease to amaze me. I am very grateful to have had him serve as my doctoral advisor.

Next, I thank the past and present members of our research group. Dr. Jin Wang, Dr. Ying Wang, Dr. Alexander Limanov, Adrian Chitu, Wesley Hattan, Miao Yu, Wenkai Pan, Ruobing Song, Akhilesh Suresh, Dr. Insung Choi, and Dr. Paul van der Wilt. Thank you all for the fruitful discussions and collaborative work. I am excited to see where our paths take us and look forward to our reunion in the future.

I would also like to thank my friends from the Cliffs Climbing Community, El Quito Frisbee Group, and Zog Frisbee Team for providing much needed respite from the tribulations of graduate school.

And finally, I thank my family members and loving partner, Ellyson. I deeply appreciate your care and support. I am forever grateful to you all.

In dedication to my family and Ellyson

Chapter 1

Introduction

1.1 Introduction

The melting of solids into liquids is a longstanding topic of research. It is a basic transformation ubiquitous in nature and can play a critical role in several different material processes, including semiconductor fabrication, metal forging, food preservation, or polymer casting. An improved understanding of the melting transition in materials can certainly lead to profound implications across a variety of disciplines. This thesis examines the dynamics of melting during the excimer-laser-induced melt-mediated crystallization of silicon films - an important technology widely used in the manufacture of displays. These studies are both scientifically interesting and technologically relevant, as further characterization of the details of melting in these rapidly heated films is necessary for such crystallization techniques to advance to the next

level of productivity and capability.

1.2 Excimer-Laser Crystallization

Since the first reported experimental observation of excimer lasing in 1970 [5], much effort has been devoted to exploring the diverse applications enabled by the technology. Perhaps the most impactful application discovered is the excimer-laser-induced melt-mediated crystallization of silicon films, aptly known as excimer-laser crystallization (ELC). ELC techniques can generate high-quality polycrystalline silicon (poly-Si) films at relatively low processing temperatures required for the fabrication of electronic devices on low-thermal-budget substrates (e.g., inexpensive glass or flexible plastic) [6][7][8].

These techniques generally start by using an excimer-gas laser to irradiate a dehydrogenated amorphous silicon (a-Si) film deposited via chemical vapor deposition onto a SiO_2-coated substrate. Due to the high absorption coefficient of silicon in the ultraviolet wavelength range, in addition to the short pulse duration of the incident beam, most of the optical energy is absorbed within the first ten nanometers at the film surface [3] resulting in the rapid heating of the film without causing a significant rise in temperature at the substrate.

At sufficiently high incident beam energy densities, the temperature of the film can exceed the melting point of silicon permitting liquid to form. Rapid cooling of the film to the substrate below occurs upon termination of the beam, which can

trigger crystallization of the molten regions. The crystallized material is sensitive to many processing parameters (e.g., beam profile, film thickness, surface passivation), however, as will be discussed at length throughout this thesis, we suggest that the spatiotemporal extent of melting in the film is the primary factor which determines the final microstructure (since solidification simply follows in a predictable manner from the unmelted solids).

1.3 Technological Implications of Laser Crystallization

Much interest in the field of laser crystallization has led to the development of myriad ELC techniques [6][7][9]. It is for their unique ability to generate, at low processing temperatures, many different possible microstructures tailored for various applications that such techniques have been successfully implemented in the manufacture of advanced displays [10][11].

The display industry has long recognized that ELC-generated poly-Si films are desirable over their competing as-deposited a-Si counterparts as the active-channel material used in thin-film transistors (TFTs) comprising the backplane of displays. This is attributed to the lower density of defects present in the polycrystalline materials. Such defects, primarily grain boundaries, can act as local scattering sites which impede the flow of charge carriers resulting in a deleterious effect on device perfor-

mance [12]. In order to increase the electron mobility of the silicon film, a reduction in the population of grain boundaries, and thereby an increase in the average grain size, appears as a simple and obvious solution.

However, a new problem regarding device uniformity arises as the grain size approaches the effective size of the TFT active channel [13]. The variation in the total number of grain boundaries contained per TFT becomes exceedingly large leading to significant fluctuations in performance characteristics between devices. Here, we can now appreciate that control over both the grain size, as well as the grain size uniformity, is paramount in these poly-Si-based TFTs that serve as the critical pixel-controlling elements in advanced displays.

1.4 Excimer-Laser Annealing

In response to the growing demands for higher-performance displays, researchers have developed a pivotal ELC technique, referred to as excimer-laser annealing (ELA), aimed to address the issues mentioned above. ELA is a multiple-pulse-per-area partial-melting-based laser crystallization technique [4]. Beyond the initial pulse, which transforms an initial a-Si film into a "fine-grained" microstructure via explosive crystallization [14][15], the subsequent pulses are mostly incident upon, and induce (partial) melting and solidification of, small and columnar grains [16][17]. Each successive pulse leads to the gradual increase in the average grain size and evolution in the overall distribution of the grain size. For various reasons, in addition to this

distinct ability to produce poly-Si films consisting of relatively large and uniform grains, ELA has become the method-of-choice for creating the poly-Si films used in the TFT-based backplane of advanced displays.

It is surprising then that even though ELA has been investigated and developed for a long period of time, the basic melting-transition-related details of the ELA process have not yet been clearly deciphered. To better understand the dynamics of melting manifested during ELA of poly-Si films, we are presently conducting experimental and numerical studies on the subject matter.

1.5 Approach for the Work

In this thesis, we seek to investigate and clarify how silicon films consisting of columnar grains melt under excimer-laser irradiation. This study is performed using "ELA poly-Si films" on SiO_2 which have previously been optimally prepared using a state-of-the-art ELA system. Such industry-grade films are exceptional as they afford us the fortuitous opportunity to explore melting in an ultra-high-purity elemental system with a unique microstructure composed of large, uniform, and periodic grains devoid of intra-grain defects. Upon irradiation of a film, we capture the melting-transformation-related details using an in situ transient reflectance and transmission setup. The transparent glass substrate allows us to take reflectance measurements at the bottom surface (in addition to the usual top surface), as well as transmission measurements throughout the thickness of the film. The combination of in situ signals

provides critical spatiotemporal information pertaining to the laser-induced melting process.

The strategy of the present investigation is to first experimentally deduce if and how the manner in which silicon films melt is affected by the presence (or absence) of high-angle grain boundaries. Therefore, in our first set of experiments, we look at the contrasting ways in which melting transpires in both ELA poly-Si films and single-crystal silicon films, which are practically free of grain boundaries and obtained via a wafer-bonding process.

In contrast to the previous experiments, which involve the beam being incident at the top surface of the films, the next set of experiments focuses on experimentally investigating the melting behavior encountered for the case in which the ELA poly-Si films are irradiated from below through the SiO_2 substrate. Doing so enables us to avoid the formation of incident beam hot spots at the film surface (an inherent phenomenon in ELA that we will discuss later). As such hot spots can affect the local thermal profile of the film, we are interested in investigating the substrate-side irradiated melting transition of the films to examine the "intrinsic" situation in which such hot spots do not participate in the melting process.

We also investigate the role that film surface conditions plays in affecting melting. Some ELA poly-Si films were treated with a buffered hydrofluoric solution (BHF) used to remove any oxide layer typically present at the silicon surface prior to irradiation. This step allowed us to study the effect of SiO_2 surface passivation on melting by

comparing the results obtained from an otherwise identical film to that of a BHF-treated film.

Alongside the experiments, we employ a numerical program developed within our group called nDNS to simulate the phase transformations experimentally observed in irradiated ELA poly-Si films. Such simulations allowed us to quantitatively estimate the physical values critical to the melting process that would otherwise be difficult to extract via experiment. Considering the obtained experimental and simulation-based results, we discuss the present state and knowledge regarding the ELA crystallization technique, as well as the implications of our findings on those previous models used to describe ELA.

The main contributions of this thesis include (1) the systematic experiments and simulations carried out to identify the intrinsic melting mechanisms in columnar-grained poly-Si films under excimer-laser irradiation, and (2) the development of an updated melting model (consistent with present and previous results) that can now more accurately characterize the melting-and-solidification cycle encountered in silicon films during ELA.

1.6 Organization of the Thesis

The remainder of this thesis is organized into eight chapters. For references, a bibliography can be found at the end of the thesis.

Chapter 2 "Background and Motivation" provides an overview of the classical

thermodynamic and kinetic descriptions and concepts of melting relevant to this work. In the latter half of this chapter, we review the current state of the melt-mediated ELA crystallization technique and how it stands to benefit from an improved understanding of the rapid melting transition in columnar-grained poly-Si films.

Chapter 3 "Transient Reflectance Analysis of Irradiated Polycrystalline Silicon Films" first describes the experimental setup used throughout this thesis, and then presents the in situ transient reflectance and transmission signals measured during excimer-laser irradiation of ELA poly-Si films consisting of columnar grains. The signals clearly show that unmelted solid regions must exist throughout the thickness of the film even at the point where the film is almost completely melted. We suggest that such melting must proceed in a remarkably and largely 2-D manner.

Chapter 4 "The Significance of Grain Boundary Melting and SiO_2 Surface Passivation" presents results from experiments carried out under special conditions to explicitly study the effects of (1) incident beam "hot spots", and (2) film surface conditions on the melting transformation in the irradiated ELA poly-Si films.

Chapter 5 "A 2-D Grain Boundary Melting Model" introduces our proposed melting model used to describe the melting-and-solidification cycle in pulsed-laser irradiated columnar-grained poly-Si films. The model invokes prompt melt-initiation at grain boundary and grain junction regions, and subsequent lateral melting into the transiently superheated interior of the grains.

Chapter 6 "Numerical Analysis of Melting" describes the nDNS numerical simula-

tion program used to simulate the melting and solidification transformations in silicon films under pulsed-laser irradiation. A phase and thermal analysis is conducted and used to estimate critical phase-transformation-related physical values, such as the degree of superheating sustained in the films during rapid heating, that would otherwise be difficult to obtain experimentally.

Chapter 7 "Implications on Laser-Induced Melt-Mediated Crystallization" discusses the implications of our work on the ELA crystallization technique, as well as other melt-mediated crystallization processes, used extensively in the manufacture of displays. We discuss how the current discovery regarding the 2-D nature of melting in ELA poly-Si films (and the general concept of melting dimensionality) can be identified and appreciated as a critical process-enabling element of ELA.

Chapter 8 "Conclusions" summarizes the results of this thesis and future research directions are recommended.

Chapter 2

Background and Motivation

2.1 Introduction

The topic of melting has long been studied due to its fundamental and universal nature. In 1910, Lindemann proposed the first microscopic theory of melting [18] arguing that crystals melt upon the average amplitude of thermal vibrations of atoms exceeding a critical fraction of the interatomic distance; this is widely known as the Lindemann Criterion. Since then, several other theories of melting have emerged based on shear modulus, entropy, and nucleation considerations [19][20][21]. Some researchers have proposed that these seemingly disparate theories may be one in the same in predicting the temperature at which melting occurs [22]. These models, however, consider melting only in a perfect crystal heated to its theoretical superheating limit. The study of melting in real solids, which generally occurs at material inter-

faces and other defects at temperatures below the theoretical superheating limit of a perfect crystal, must be properly addressed.

Over the years, several near-equilibrium experimental, theoretical, and computational investigations have been performed to examine melting in polycrystalline solids [23]. However, the topic of rapid melting in polycrystalline films has been lacking especially in terms of experimental results. The complexity of such a melting process has led to various unresolved questions with profound scientific and technological implications. In this chapter, we provide a basic description of the melting transformation and the various melting mechanisms relevant to our studies of rapid melting in pulsed-laser irradiated poly-Si films under far-from-equilibrium conditions. We also discuss the current state of the ELA process, a melt-mediated laser crystallization technique used extensively in the manufacture of advanced displays, and how it stands to benefit from an improved understanding of the melting behavior in polycrystalline materials.

2.2 A Classical Description of Melting

At a given pressure, the solid and liquid phases of an elemental system can coexist in thermodynamic equilibrium at the equilibrium melting point (T_m) [3]. It is at T_m, as shown in Figure 2.1, that the Gibbs free energy of the solid and liquid phases are equal. For temperatures above T_m, melting is thermodynamically favored since the Gibbs free energy of liquid is less than that of solid. Conversely, a similar argument

can be made for solidification for temperatures below T_m.

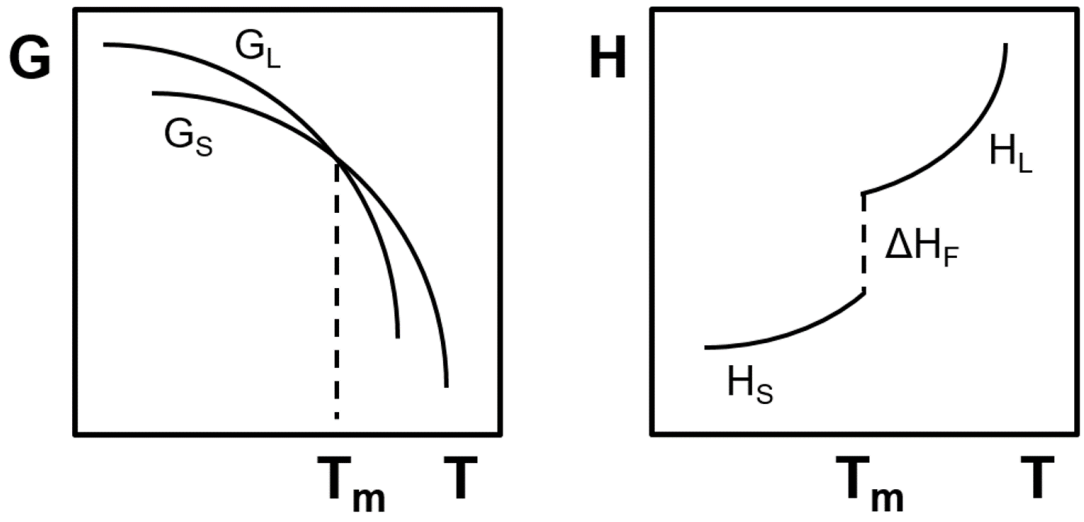

(a) (b)

Figure 2.1: Schematic illustrations of (a) the Gibbs free energy of the solid phase (G_S) and liquid phase (G_L), and (b) the enthalpy of the solid phase (H_S) and liquid phase (H_L) as a function of temperature, where T_m is the equilibrium melting point. A discrete change in enthalpy (ΔH_F) is observed at T_m because of the discontinuous nature of the melting and solidification transformations.

Since melting is a transformation that involves a discrete change in enthalpy, as depicted in Figure 2.1, it is considered a first-order discontinuous phase transition [24]. This change in enthalpy is consumed at the solid-liquid interface during melting, as melting is considered an endothermic process. Solidification, on the other hand, is an exothermic process since the change in enthalpy is released at the interface. Other discontinuities in physical parameters, including heat capacity and density, are also generally observed upon such first-order phase transformations. For the specific case of melting in silicon, a sudden increase in optical reflectance [25] and electrical conductivity [26] are induced owing to the fact that liquid silicon is metallic whereas

solid silicon is a semiconductor.

2.2.1 Classical Nucleation Theory

As mentioned above, melting is energetically favorable if the temperature of the solid rises above the equilibrium melting point. However, in order for the nucleation (or spontaneous formation) of liquids to occur within a solid volume, the solid must be heated to well above its equilibrium melting point. Classical nucleation theory (CNT), the current framework of which was significantly developed by Turnbull [27], and whose work builds upon the seminal contributions of others [28][29], can be applied to address this superheating phenomenon of solids by considering the various thermodynamic and kinetic factors involved.

According to CNT, the nucleation of liquid is a stochastic process involving random fluctuations in the local disordering of regions in an ordered solid matrix. The size of any one disordered region can randomly shrink (and even disappear), or grow to become a stable liquid nucleus depending largely on the thermodynamic conditions of the system. The critical energy barrier to creating such a liquid nucleus, assumed spherical in shape, homogeneously within a solid is given as [21]:

$$\Delta G^* = \frac{16\pi\sigma_{sl}^3}{3\left(\Delta G_{sl} + \Delta E\right)^2} \tag{2.1}$$

where σ_{sl} is the surface energy per unit area between the liquid nucleus and solid matrix (assumed isotropic for simplicity), ΔG_{sl} is the volumetric free energy difference

between the solid and liquid phases, and ΔE is the strain energy associated with forming a liquid nucleus within the rigid solid. The rate of generation of these nuclei is defined as the nucleation rate which can be approximated as:

$$I = I_0 \exp\left(-\frac{\Delta G^*}{kT}\right) \tag{2.2}$$

where I_0 is a kinetic prefactor, k is the Boltzmann constant, and T is the local temperature. The temperature at which homogeneous nucleation of liquid occurs should be far above the equilibrium melting point. Homogeneous nucleation has rarely, if ever, been experimentally observed (unless possibly under extreme non-transient conditions [30]). Heterogeneous nucleation of liquid readily occurs instead at material interfaces, such as surfaces and grain boundaries, at temperatures at or near the equilibrium melting point [31]. This is due to the considerable catalyzing effect of these interfaces (captured in a contact angle term, $f(\theta)$ where $0 < f(\theta) < 1$), which can severely reduce the free energy barrier associated with heterogeneous nucleation:

$$\Delta G^*_{het} = \Delta G^*_{hom} * f(\theta) \tag{2.3}$$

where ΔG^*_{het} and ΔG^*_{hom} are the critical free energy barriers to heterogeneous and homogeneous nucleation, respectively, and θ is the contact angle formed between the nucleus and heterogeneous interface. Due to the reduced barrier associated with heterogeneous nucleation, the nucleation and growth of liquids almost always occurs

heterogeneously. Figure 2.2 shows a schematic diagram illustrating the scenarios for homogeneous and heterogeneous nucleation.

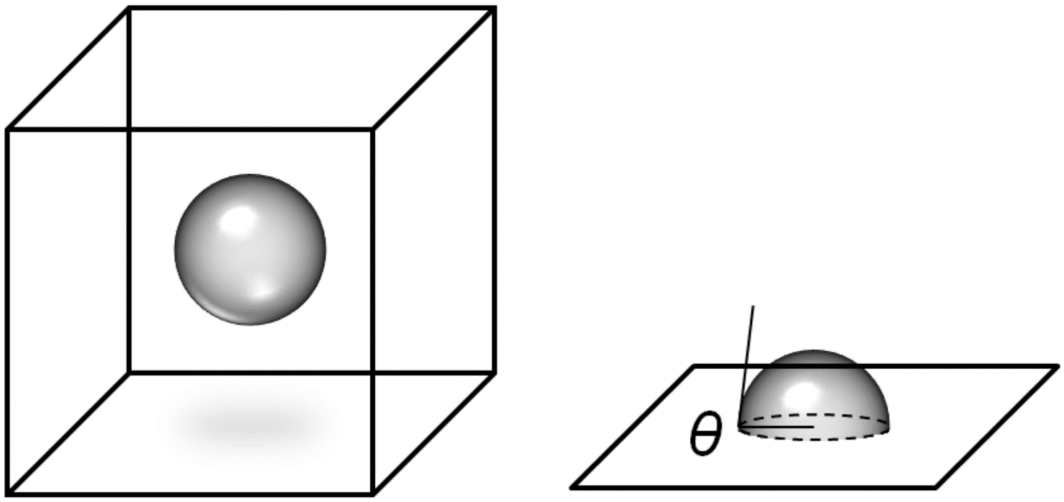

(a) (b)

Figure 2.2: Schematic diagram of (a) a homogeneously nucleated sphere in its host matrix, and (b) a heterogeneously nucleated spherical cap forming a contact angle of θ along a catalyzing interface in its host matrix.

2.2.2 Interface Response Function

Upon the formation of a solid-liquid interface, the velocity at which melting proceeds depends largely on the interfacial temperature. The interface response function (IRF), an important relation which can capture the kinetics of melting (or solidification) under far-from-equilibrium conditions, is used to describe the interfacial motion in response to superheating (or undercooling) of the interface. According to Turnbull *et al.* [32], the IRF is given as:

$$v(T) = v_0 \exp\left(-\frac{Q}{kT}\right)\left[1 - \exp\left(-\frac{\Delta G_{sl}}{kT}\right)\right] \tag{2.4}$$

where, according to diffusion limited theory [1], T is the interfacial temperature, v_0 is a kinetic prefactor, Q is an activation energy for the self-diffusion of atoms near the interface, k is the Boltzmann constant, and ΔG_{sl} is the difference in Gibbs free energy per atom between the solid and liquid phases.

At temperatures near the equilibrium melting point, ΔG_{sl} can be approximated as:

$$\Delta G_{sl} = \frac{\Delta H_F \Delta T}{T_m} \tag{2.5}$$

where ΔH_F is the latent heat of fusion, $\Delta T = T_m - T$, and T_m is the equilibrium melting point. When ΔG_{sl} is sufficiently small, the bracketed term in equation 2.4 can be re-written using a Taylor series expansion:

$$v(T) = v_0 \exp\left(-\frac{Q}{kT}\right)\left(\frac{\Delta G_{sl}}{kT}\right) \tag{2.6}$$

and then further simplified by combining equations 2.5 and 2.6 into a function linearly dependent on ΔT:

$$v(T) = c * \Delta T \tag{2.7}$$

where c is an approximate constant that can be extracted from experimental data. By convention, $v(T)$ is positive and negative for solidification and melting,

respectively.

Stolk *et al.* successfully derived a quantitative IRF for silicon by considering the experimentally obtained limits on the velocity of melting and solidification for silicon discovered from their own work and those reported by others [1]. Their IRF data is reproduced in Figure 2.3. As can be seen, separate IRF curves exist for both the crystalline silicon (c-Si) phase and amorphous silicon (a-Si) phase. Figure 2.3 requires that (1) a-Si melts at a lower temperature than that of c-Si, and (2) amorphous solidification (i.e., amorphization) be obtained under a large degree of supercooling; both cases have been confirmed experimentally [33][34][35].

2.2.3 Gibbs-Thomson Equation

A solid generally begins to melt as its temperature reaches the equilibrium melting point. However, various factors including sample size and material defects (or lack thereof) can significantly alter the effective temperature at which melting initiates. One such factor is the local curvature in the heated solid, which can lead to a variation in the chemical potential, and consequently, the local equilibrium melting point across the curved surface or interface. This curvature effect is commonly referred to as the Gibbs-Thomson effect. In the context of this thesis, it refers to the observation that a smaller crystal of higher curvature (or larger crystal of lower curvature) can be in thermodynamic equilibrium with its melt at a lower (or higher) temperature than the bulk equilibrium melting point. That is, the local equilibrium melting point of a solid

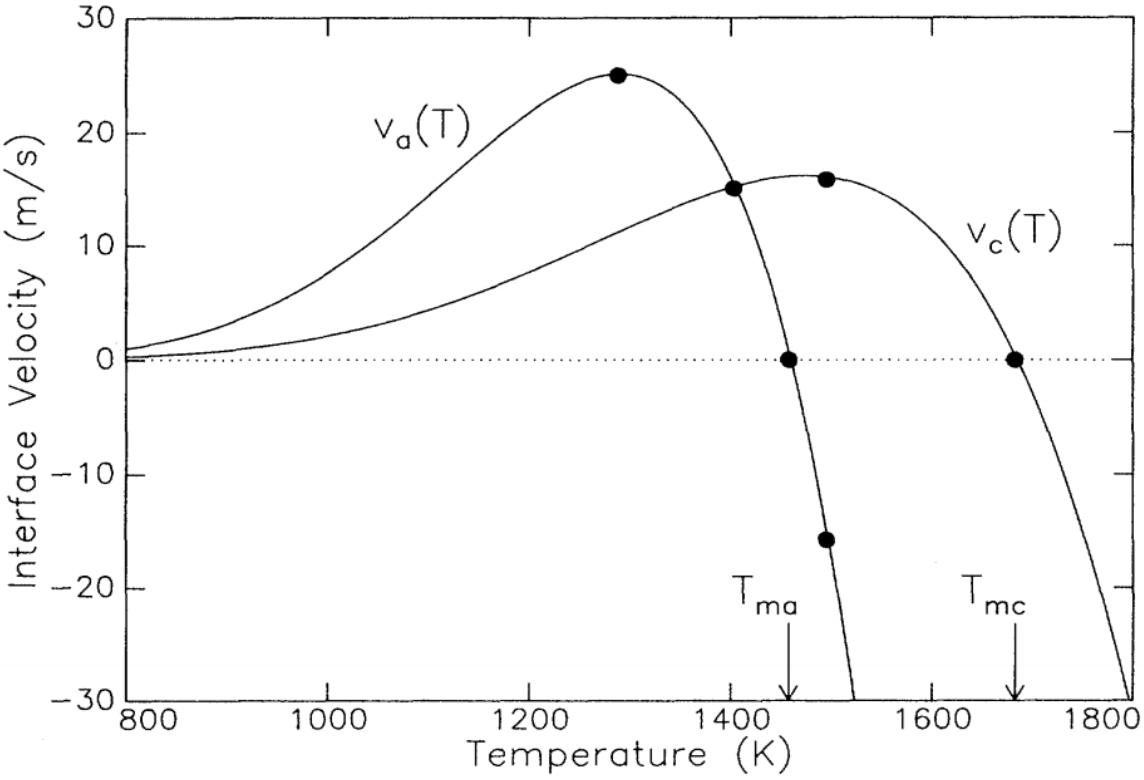

Figure 2.3: Interface response function for c-Si ($v_c(T)$) and a-Si ($v_a(T)$) derived from available experimental data, which are marked as solid points in the figure. $T_{m,c}$ and $T_{m,a}$ represent the equilibrium melting temperatures of c-Si and a-Si, respectively. This figure is adapted from [1].

can be increasingly depressed or elevated with decreasing or increasing size of the solid [36], respectively. Derived from the earlier work of Gibbs [37], the Gibbs-Thomson effect is described by the following equation of the general form:

$$T_m^{local} = T_m \left(1 - \frac{2\sigma_{sl}}{\Delta H_F}\rho(x)\right) \tag{2.8}$$

where T_m^{local} is the local equilibrium melting point, T_m is the bulk equilibrium melting point, σ_{sl} is the solid-liquid interfacial free energy per unit area, ΔH_F is the

enthalpy of fusion per unit volume, and $\rho(x)$ is the local curvature of the solid, which is a function of the size of the solid, x. Depending on the sign of the local curvature, the local equilibrium melting point may be either depressed or elevated.

2.3 Various Melting Sites in Polycrystalline Solids

The inevitable presence of material defects, such as surfaces, grain boundaries, and solid-solid heterophase interfaces, can greatly affect the way melting proceeds in real materials. This is especially true in partial-melting-based laser crystallization techniques. To better understand the melting behavior in solids during such materials processes, we must establish some insight on how melting can initiate heterogeneously at these high-excess-free-energy sites. In this section, we review melting at material defects relevant to the experiments performed in this thesis.

2.3.1 Surface Melting

Melting often initiates promptly at the surface of a solid [38]. In addition to the fact that most solids are heated externally, this can be attributed to the relatively high free energy [39] and large available area associated with the surface. Previous investigations suggest that the melting transition begins via surface pre-melting occurring at temperatures well below the equilibrium melting point (followed by discontinuous melting) [40]. As such, it is incredibly challenging to superheat a solid well above its equilibrium melting point for an extended period (i.e., non-transient superheating)

since it is typically precluded by melting at the surface.

Surface melting can be described, in a thermodynamic sense, as the wetting of a solid surface by a thin layer of its own liquid as the solid is heated to its equilibrium melting point. Figure 2.4 depicts this situation. In terms of the interfacial energies involved, it is expressed as:

$$\sigma_{sv} > \sigma_{sl} + \sigma_{lv} \tag{2.9}$$

where σ_{sv}, σ_{sl}, and σ_{lv} are the interfacial energies of the solid-vapor, solid-liquid, and liquid-vapor interfaces, respectively. These interfacial energies are a function of temperature ($\sigma(T)$). If equation 2.9 is satisfied at a temperature below the equilibrium melting point, surface pre-melting is said to occur whereby a "quasi-liquid" layer is formed at the surface with properties intermediate between those of a solid and liquid. Such a layer becomes increasingly disordered and grows in thickness as the temperature of the solid rises. When the temperature of the solid reaches the equilibrium melting point, the more familiar discontinuous melting process ensues and the disordered layer behaves as a bulk liquid.

The surface energies involved in equation 2.9 are also orientation dependent ($\sigma(\theta)$), as shown in Figure 2.5. While most heated surfaces exhibit pre-melting, as described above, researchers have reportedly observed superheating at surfaces with particular crystallographic orientation under extremely high heating rates [41][42]. Those exceptional heating rates are far beyond the range of most heating sources, including

(a) (b)

Figure 2.4: Schematic diagram of a (a) solid in contact with vapor, and (b) liquid layer formed at the surface of the solid upon surface melting.

the excimer laser used in the experiments presented in this thesis. For the purposes of our work, it is assumed that discontinuous melting at the silicon film free surface (for all orientations) initiates at or very near the bulk equilibrium melting point of silicon (1685 K). It should be noted that surface pre-melting is not detected with our current experimental setup.

2.3.2 Grain Boundary Melting

Grain boundaries are a common type of material defect whose presence has long been known to influence how a solid melts [31]. Chalmers, in 1940, [43], conducted one of the earliest investigations on the topic of grain boundary melting and concluded that melting readily initiates at grain boundaries at temperatures very near the equilibrium melting point. Since then, a large body of evidence has grown which supports this notion of grain-boundary-initiated melting. [44][45][46][47].

However, the type of grain boundary is also a significant detail that must be

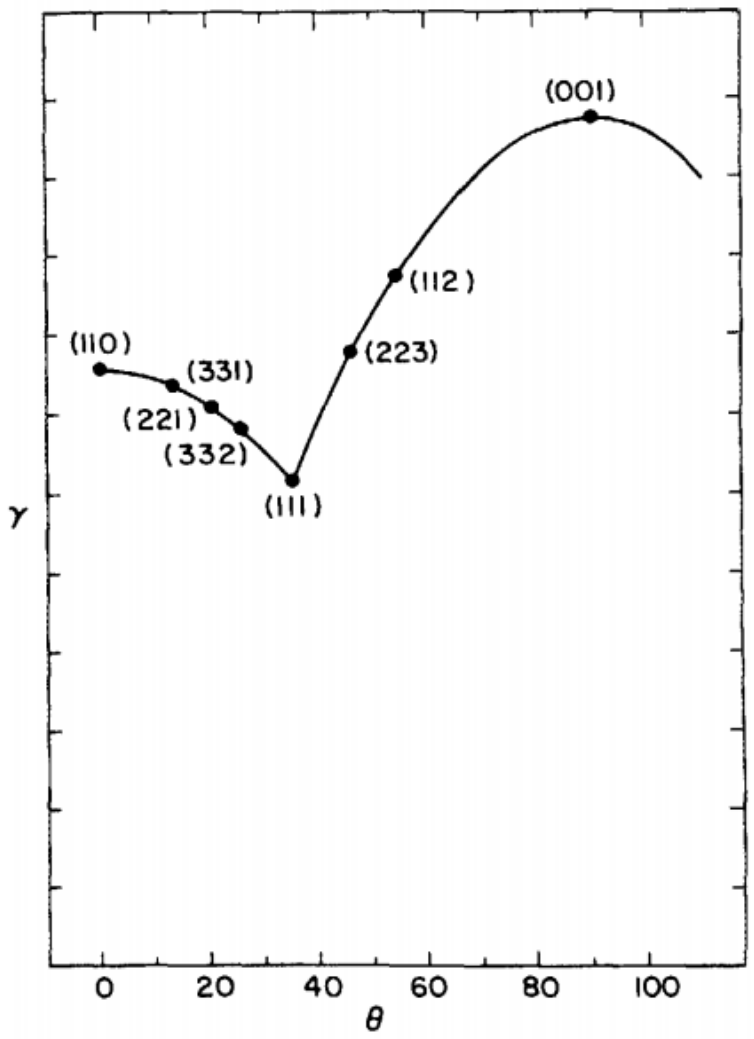

Figure 2.5: Relative surface energy, γ, as a function of surface orientation, θ, in cubic materials (adapted from [2]).

considered when characterizing the tendency for grain boundaries to melt. The degree of crystallographic misorientation between two neighboring crystals can determine the free energy of their grain boundary interface, as shown in Figure 2.6. This can affect the condition that determines whether melting is thermodynamically favored to initiate at grain boundaries. Such a condition is given in equation 2.10:

$$\sigma_{gb} > 2\sigma_{sl} \tag{2.10}$$

where σ_{gb} is the grain boundary energy and σ_{sl} is the interfacial energy of the solid-liquid interface. The grain boundary energy $\sigma_{gb}(T, \theta)$ is a function of both temperature (T) and misorientation (θ). Experimentally, it has been shown that equation 2.10 is generally satisfied at temperatures very near the equilibrium melting point for general high-angle grain boundaries under near-equilibrium conditions. However, not much information is available regarding the topic of grain boundary melting under far-from-equilibrium conditions. As such, the results obtained in the present work can be appreciated as helping to fill this gap of knowledge. Figure 2.7 shows a schematic diagram depicting grain boundary melting.

In addition to experiment, researchers have demonstrated via molecular dynamics simulations that, indeed, high-angle grain boundaries in silicon and other elemental solids begin to melt when heated to their respective equilibrium melting point [48]. However, some theoretical results suggest that low-excess-free-energy grain boundaries, such as low-angle or coherent twin grain boundaries, can sustain a significant

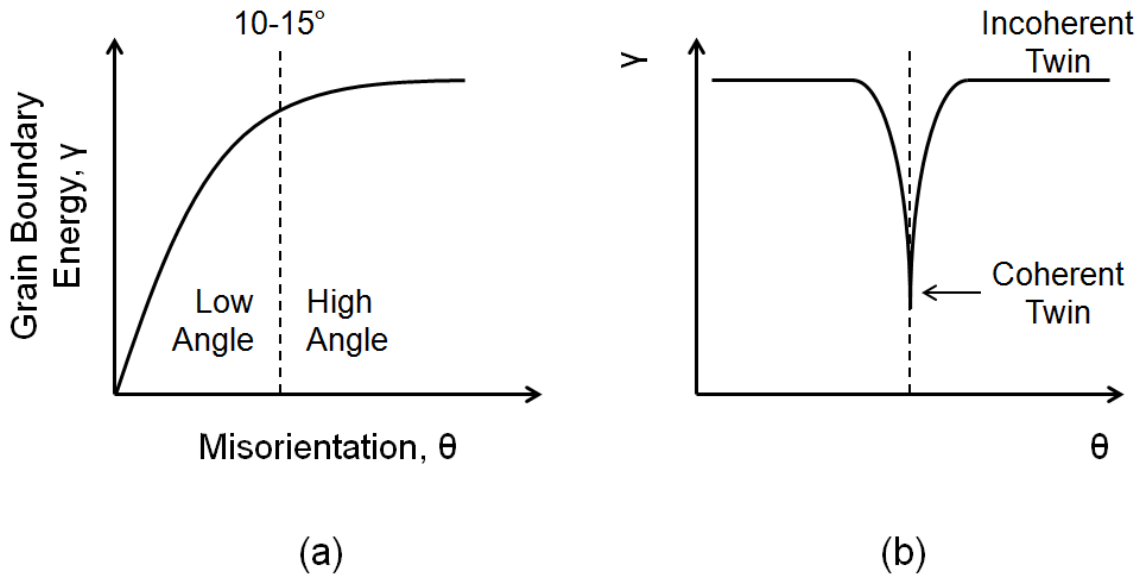

Figure 2.6: Schematic diagrams generally illustrating the (a) grain boundary energy, and (b) twin-boundary energy as a function of misorientation. This figure is adapted from [3].

degree of superheating [49]. Along this same line of thought, using nucleation theory, researchers have demonstrated the existence of a substantial energy barrier that may inhibit the nucleation of liquid at these particular low-energy grain boundaries [50][51].

The microstructure of the columnar-grained poly-Si films investigated in this thesis consists primarily of general high-angle grain boundaries, which are, unlike previous investigations involving low near-equilibrium heating rates, heated very rapidly with a pulsed laser. Therefore, we expect melting at these grain boundary regions takes place at a temperature at least at or above the equilibrium melting point. It should be noted that the field of research regarding superheating and pre-melting at grain

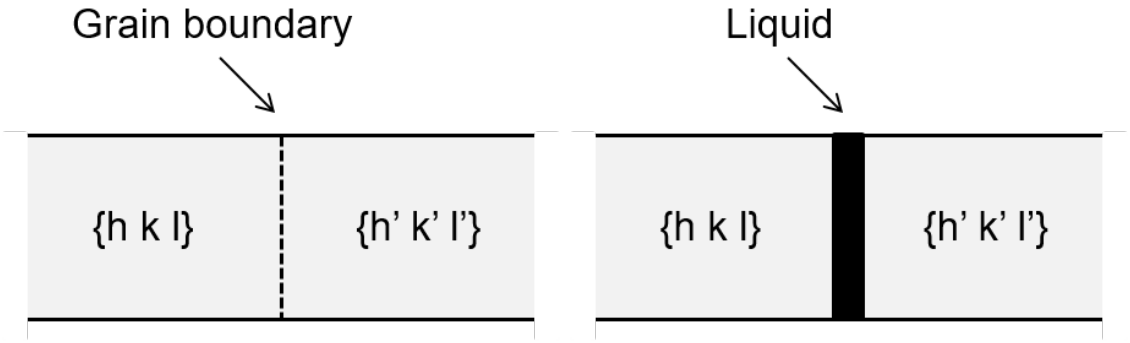

Figure 2.7: Schematic diagram of two solids with different crystallographic orientations ($\{hkl\}$ and $\{h'k'l'\}$) (a) sharing a grain boundary, and (b) separated by a liquid layer formed at the grain boundary upon complete grain boundary melting.

boundaries remains fraught with ambiguity. The lack of experimental evidence in the field is partially attributed to the myriad difficulties involved in studying melting at such buried interfaces.

2.3.3 Melting at Solid-Solid Heterophase Interfaces

In addition to surfaces and grain boundaries, we must consider the solid-solid heterophase interface (in our case, the Si-SiO_2 interface) as yet another material defect affecting the melting transition of the silicon films on SiO_2 studied in this thesis. The stability of the heterophase interface against melting is highly dependent upon its structure, chemical composition, and other relevant material properties. For example, at high-excess-free-energy interfaces, such as in incoherent or mechanically stressed interfaces, little to no substantial superheating is expected since it is rather energetically favorable for the interface to readily melt [23]. Conversely, low-excess-

free-energy interfaces can sustain a significant degree of superheating [52][53]. Recently, we have experimentally discovered that the Si-SiO_2 interface may be one such interface capable of sustaining hundreds of degrees of superheating [54][55]. We will discuss this point in detail later in this chapter.

The poly-Si films examined in this work are obtained from industrial sources and possess a device-grade quality (i.e., high purity and planar) Si-SiO_2 interface. We presume the interface is quite stable and likely capable of resisting melting at temperatures far above the equilibrium melting point of bulk crystalline silicon. One focus of this thesis is to more closely investigate the effect of the Si-SiO_2 interface, especially that interface formed between the native surface oxide layer and the silicon film, on melting. This new information may considerably benefit the microelectronics industry since practically every silicon-based transistor uses a gated oxide layer. It may also contribute to the greater scientific field of melting at the solid-solid heterophase interface.

2.3.4 Internal Melting

Thus far, we have discussed melting at several common material defects present in polycrystalline solids. Those varied defects can behave as melt triggering sites that largely affect the melting transition. However, we must also consider internal melting, or melting within the bulk of a crystal, since polycrystalline materials can be viewed as being comprised of many individual crystals or grains. The formation of liquid

within the bulk of a crystal requires substantial superheating and corresponds to a fundamental melting mechanism of great scientific importance.

Several theoretical models have been proposed to describe the phenomenon of superheating and subsequent internal melting with emphasis placed on investigating the superheating limit of a crystal [56]. Among the several theoretical criteria for melting, the Lindemann and Born criteria are those most frequently applied. The Lindemann criterion invokes melting due to an atomic vibrational instability [18], whereas the Born criterion is based on a vanishing elastic shear modulus causing the crystal to lose all rigidity and subsequently melt [19]. Other models include entropy-driven and volume-driven melting instabilities that occur at a critical superheating temperature where the entropy and volume of the solid and liquid phases are equal, respectively [20][57]. However, these predicted upper limits of superheating have not been experimentally observed.

Nucleation models derived from classical nucleation theory have also been used to describe internal melting [21]. These models have generated superheating limits lower than those previously mentioned, and thus suggest internal melting may be a nucleation-limited process. In regard to superheating in rapidly heated silicon films via pulsed-laser irradiation, estimates using nucleation theory indicate that such films can be superheated to at least 200 K above the equilibrium melting point [55]. In addition to the work presented here, much progress continues to be made in studying the superheating limit of solids (and subsequent internal melting) with recent efforts

even demonstrating that the limits of superheating described by Lindemann, Born, and nucleation theory may all be one in the same [22].

2.4 Melt-Mediated Crystallization of Silicon Films

The major focus of this thesis is to examine the pulsed-laser-induced melting transition in poly-Si films. These studies are of utmost importance for the development of various melt-mediated Si-film-based laser-crystallization processes where the very details and extent of melting can largely determine the resulting microstructure of the irradiated films. The final processed microstructure is critical since it affects the performance of the devices fabricated on such films. In addition to its evident technological relevancy, silicon films are an ideal platform for studying fundamental phase transformations since (1) silicon is the most thoroughly studied material in the world, (2) various unique polycrystalline microstructures can be generated via several well-established techniques [9][58][59], and (3) high-purity device-grade films are readily obtained via standard industry practices, whereby such films enable the study of melting in a practically contaminant-free elemental system. In this section, we introduce the basic transformation pathways relevant to melting and solidification in laser irradiated silicon films, especially as it pertains to the critical ELA process used in the manufacture of advanced displays.

2.4.1 Partial and Complete Melting Regimes During Excimer-Laser Processing

The excimer-laser-induced melting (and subsequent crystallization) of silicon films can be characterized into different melting regimes determined by the maximum depth of melting achieved during laser irradiation [16]. The maximum melting depth depends primarily on the incident beam energy density among several factors (e.g., film thickness, substrate thermal conductivity). At low energy densities, the irradiated film undergoes partial melting such that a continuous unmelted bottom layer remains in contact with the top layer of liquid silicon. Upon cooling to below the equilibrium melting point, vertical solidification proceeds from the solid-liquid interface into the liquid regions. At high laser energy densities, on the other hand, the film is completely melted and there does not exist any solid silicon to promptly seed solidification (the inert SiO_2 substrate does not seed solidification) as in the partial melting case. Instead, solidification occurs via the nucleation and growth of solids in the fully molten film, which requires cooling to well below the equilibrium melting point of silicon [35][60][61].

The energy density threshold separating the transition between partial and complete melting is referred to as the complete melting threshold (CMT). For energy densities just below the CMT, a narrow sub-regime exists where unmelted islands survive the melting process. These isolated crystals grow, upon cooling to below the equilibrium melting point, laterally into their neighboring liquid regions and can

attain exceedingly large grain sizes much greater than the film thickness. This melting sub-regime is called the super-lateral growth (SLG) regime [62]. Schematics of all three melting regimes showing different maximum melt depths are displayed in Figure 2.8.

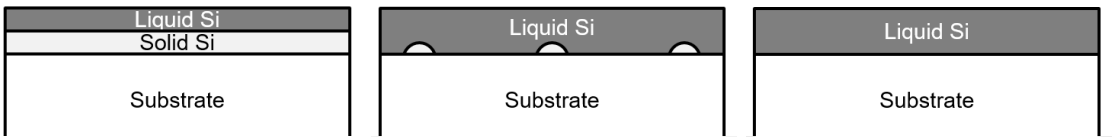

(a) (b) (c)

Figure 2.8: Schematic diagrams of a silicon film at the maximum extent of melting within the (a) partial melting regime, (b) near-complete melting or SLG regime, and (c) complete melting regime.

From the above discussion, it is clear that the extent of melting in silicon films during laser irradiation essentially dictates the subsequent solidification pathway (and resulting microstructure) taken by the film. We point out, however, that the presence of grain boundaries in the irradiated material can significantly affect the melting and solidification scenarios mentioned above, as will be examined in this thesis. As such, it can be useful to categorize the various existing melt-mediated crystallization techniques by their operating melting regimes. For instance, the mixed-phase solidification process (a technique capable of generating large and highly textured grains) [63] and the ELA process [4] both function in the partial melting regime (in contrast, the sequential lateral solidification [7] process operates in the complete melting regime). We will examine the phase-transformation-related details of some of these processes in the following sections.

2.4.2 Mixed-Phase Solidification

Mixed-phase solidification (MPS) is a beam-induced crystallization technique that can generate a unique polycrystalline microstructure consisting of large, uniform, and highly textured grains. While researchers have demonstrated its viability using various heating sources [64], MPS is generally conducted using a continuous-wave (CW) laser operating in the visible-green wavelength regime which is repeatedly scanned over the surface of an initially amorphous or small-grained silicon film encapsulated in SiO_2. With each scan, the average grain size increases, as well as the fraction of (100)-surface-textured grains. This microstructure evolution is explained by considering the interplay between (1) the change in reflectance between the solid and liquid phases of silicon, and (2) the dynamically balanced yet continuously changing surroundings of stable coexisting superheated solid and supercooled liquid regions.

The relatively "long pulse duration" (viewed as effectively infinite) of the CW laser while it is incident on and scanning the film (as well as the long absorption distance of solid silicon in the visible-green wavelength regime) lends the process to a near-equilibrium and near-isothermal environment. Under such conditions, it is observed that melting initiates at grain boundaries, followed by melting proceeding laterally in the films. The asymmetric rates of melting and solidification, dictated by local thermal and thermodynamic conditions, for individual grains results in the shrinkage (and full elimination) of some grains and the growth of others. These are the factors that underlie the overall grain evolution observed in MPS and the details of which we

leverage to support the findings of the present thesis. Here, it is important to identify that these MPS-based results (associated with melting in poly-Si films) arise from a near-equilibrium process, whereas the results of this thesis examines rapid melting in pulsed-laser irradiated poly-Si films under far-from-equilibrium conditions.

2.4.3 Excimer-Laser Annealing

Another method used to generate poly-Si films is the all-important ELA crystallization technique used in display manufacturing [4]. It is a partial-melting-based excimer-laser crystallization process that can produce poly-Si films consisting of uniform and columnar grains on low-thermal-budget substrates. The resulting material is well-suited for the fabrication of TFTs on temperature-sensitive and inexpensive substrates, such as glass or plastics.

In general, the ELA process utilizes a xenon-chloride excimer-gas laser operating at a 308-nm wavelength. Typically, the laser beam is first optically homogenized and shaped to form a high-aspect-ratio line beam (1.6 m $\times$ 0.6 mm) with top-hat profile, and then incident upon, and scanned across, the surface of a precursor a-Si film such that twenty or so pulses are deposited per area on the film. Each subsequent pulse induces (partial) melting of the film, followed by grain enlargement upon solidification. With increasing shot number, the average grain size increases (and eventually soft saturates to a value near the wavelength of the incident irradiation) resulting in the grain size distribution becoming more narrow. Plan-view TEM images of the

microstructure evolution observed in a typical twenty-shot ELA process is shown in Figure 2.9.

Surface damage, which occurs when the rapidly heated film reacts with an oxygen-rich atmosphere [65], is mitigated by irradiating the film in a controlled inert environment. The multiple-shot irradiation process is further optimized, regarding processing speed and throughput, by matching the high pulse-repetition frequency of the laser to the beam-translation velocity resulting in (1) the optimal overlap between subsequent pulses, and (2) each area of the film receiving the necessary twenty or so pulses in a rapid and efficient manner. Additional details of the ELA process can be found elsewhere [66][67][10].

As we have stated before, the melting portion of the pulsed-laser-induced melting-and-solidification cycle can be identified as being the critical step that dictates the microstructure evolution realized during ELA (since solidification simply follows in a predictable manner from the unmelted solid regions), and microstructural quality of the resulting material. However, despite the fact that ELA has been investigated and utilized for many years, the melting-transformation-related details of ELA have not yet been clearly deciphered. We suggest that these basic details should be characterized and established in order for the crystallization technique to advance to the next level of productivity and capability. Doing so can be appreciated as a timely exercise in that the material-performance-related demands of the growing ultra-high-resolution display market are not so easily met by the current version of ELA. Al-

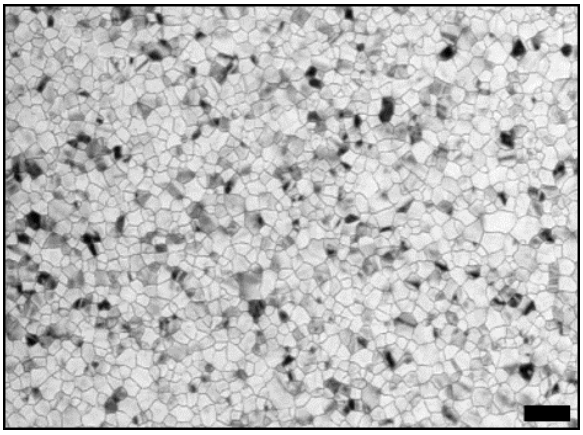

(a)

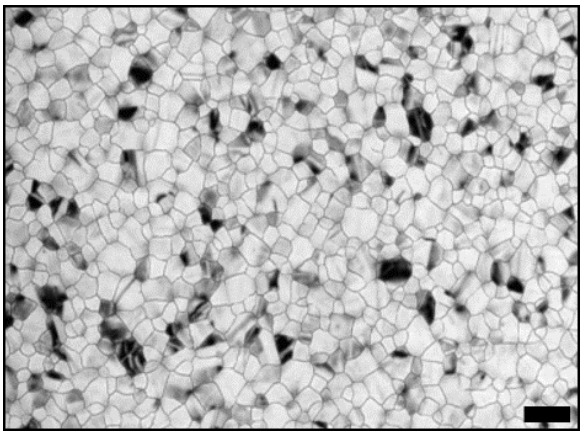

(b)

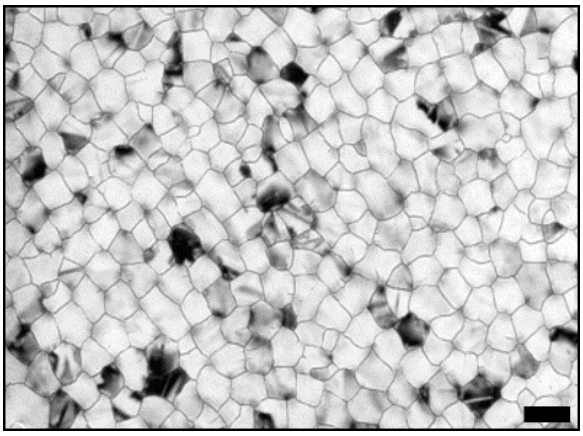

(c)

Figure 2.9: Plan-view TEM images showing the microstructure evolution of a silicon film undergoing a typical ELA process after (a) 12, (b) 16, and (c) 20 pulses. Light defect etching was applied before TEM imaging to enhance grain boundary contrast. The scale bar is 0.5 um.

though ELA has proven to be more than sufficient for lower-resolution products, it often ends up generating microstructurally non-uniform films that lead to commensurately non-uniform displays, which, in turn, lowers the manufacturing yields of the displays.

2.4.4 Unresolved Problems in Previous ELA Models

Many contradictory models have been proposed describing the ELA process [68][17][69][70][71]. While it is understood that ELA operates in the partial melting regime, additional information pertaining to the melting transition remain unclear (or contested), such as (1) the location at which melting initiates, or (2) the manner in, or degree to which, liquid expands in the rapidly heated silicon films. We will examine these very details in this thesis using a combination of experimental and numerical simulation-based investigations.

A variety of process-related details must be considered when studying how these irradiated poly-Si fims "intrisically" melt. Such details may include variations in the film thickness [72][4], surface-scattering-induced "hot spots" resulting in a non-uniform or periodic heating profile of the film [73][74], and presence of different material defects (e.g., free surfaces, grain boundaries, grain junctions) comprising the heterogeneous nature of the polycrystalline films [75]. The passivation of the silicon film surface can also play a significant role in affecting the melting transformation [54]. In the work presented here, we are dutifully cognizant of these relevant factors

as we conduct our investigations. Systematic studies of such melting mechanisms are very much needed to resolve the longstanding discrepancies that exist across various models of the ELA process.

2.4.5 Relevant Previous Investigations

In a past effort to investigate the phase transformation mechanisms involved during ELA processing of silicon films, we have concluded, based on the TEM microstructure analysis of multiple-shot irradiated poly-Si films, that localized complete melting of the film must at least take place at and near the grain boundaries [17]. It was suggested, furthermore, that the asymmetric extent of melting and/or solidification between the adjacent grains, as influenced by various physical and thermodynamic factors (e.g., grain size, orientation, thickness, defect density), will then eventually lead to the apparent growth of some grains and effective shrinkage and/or full elimination of the other grains. Such phase-transformation-related details underlie the microstructure evolution observed in ELA, which is described by a gradual increase in the average size and enhancement in uniformity of the grains.

Additionally, we have come to appreciate, based on recent results obtained in substrate-side irradiated single-crystal silicon films, the relatively melt-resistant nature of the Si/SiO_2 interface [54]. It was estimated that the rapidly heated silicon at the interface can sustain several hundreds of degrees of superheating before the onset of melting, whereas in contrast, melting at the free surface of the film readily tran-

spires at much lower temperatures (presumably at or near the equilibrium melting temperature). It was also found that internal melting within the crystalline bulk of the film does not occur even at the highest heating rates obtained, which suggests a greater superheating limit for crystal regions than that of the superheating-permitting Si/SiO_2 interface. The present work will build on this hierarchy of superheating limits and incorporate general high-angle grain boundaries into the analysis.

We leverage these previously obtained findings to guide the present work in examining the melting transition in pulsed-laser irradiated poly-Si films using new and advanced experimental and computational methods.

2.4.6 Motivation and Research Strategy

Due to its scientific importance and technological relevancy, the melting of polycrystalline films is a fundamental topic of study where an improved understanding would surely lead to profound implications across various disciplines. For instance, the basic dynamics of melting in poly-Si films during ELA processing have not yet been clearly deciphered and require further understanding. Moreover, fundamental investigations of rapid melting at grain boundaries, solid-solid heterophase interfaces, and other material defects have been severely lacking [23].

In this thesis, we examine rapid melting in a polycrystalline microstructure by performing pulsed-laser-induced melting experiments on columnar-grained poly-Si films generated via ELA processing. It is notable that the films used in this work are ob-

tained from industry sources and are of device-grade quality to ensure that the results presented here capture the universal behavior of melting in polycrystalline materials. During irradiation of the films, in situ transient reflectance and transmission measurements are collected, which allow us to obtain critical spatiotemporal details of the melting transition with nanosecond time-resolved resolution. Numerical simulations are performed alongside the experiments, which allow us to quantitatively estimate critical physical parameters that would otherwise be difficult to ascertain via experiments alone.

The motivation of this work is two-fold: (1) to improve our understanding of the technologically important ELA process by more closely examining melting in pulsed-laser irradiated poly-Si films consisting of columnar grains, and (2) to experimentally address some fundamental questions pertaining to rapid melting in heterogeneous films.

Chapter 3

Transient Reflectance Analysis of Irradiated Polycrystalline Silicon Films

3.1 Introduction

In this chapter, we present experimental results demonstrating the 2-D nature of melting and solidification in rapidly heated poly-Si films consisting of small and columnar grains. Such results were obtained via pulsed-laser irradiation of ELA-prepared poly-Si films on SiO_2 substrates, where the spatiotemporal details of the laser-induced phase transformations were tracked using in situ frontside and backside transient reflectance (FTR and BTR, respectively) and transient transmission (TT) analysis

techniques. The measured FTR, BTR, and TT signals revealed that neither the top (front) nor bottom (back) surfaces of the films underwent complete surface melting even at relatively high incident energy densities up to the CMT, or the threshold at which the irradiated films are fully molten throughout. Such observations are explained as a result of localized complete melting transpiring promptly at the columnar grain boundary and grain junction regions, followed by 2-D melting proceeding laterally into the transiently superheated interior of the unmelted grains.

3.2 Experimental Setup

The samples used in the experiments described throughout this thesis were prepared via ELA processing (using a state-of-the-art ELA system and procedure) of 50-nm-thick a-Si films deposited via plasma-enhanced chemical vapor deposition on SiO_2-coated glass substrates. The microstructure of the resulting ELA-processed films, referred to henceforth as ELA poly-Si films, consists largely of 300-nm grains with surface protrusions at the columnar grain boundary and grain junction regions [4]. These protrusions can be seen in the AFM surface morphology plots given in Figure 3.1 and Figure 3.2. A plan-view TEM image of a sample of the ELA poly-Si films is shown in Figure 3.3. Low-magnification TEM-based crystallographic-orientation mapping did not show any preferred grain texture in the films studied here.

A schematic diagram of the pulsed-laser system used to irradiate the ELA poly-Si films is given in Figure 3.4. The laser source used was a xenon-chloride gas excimer

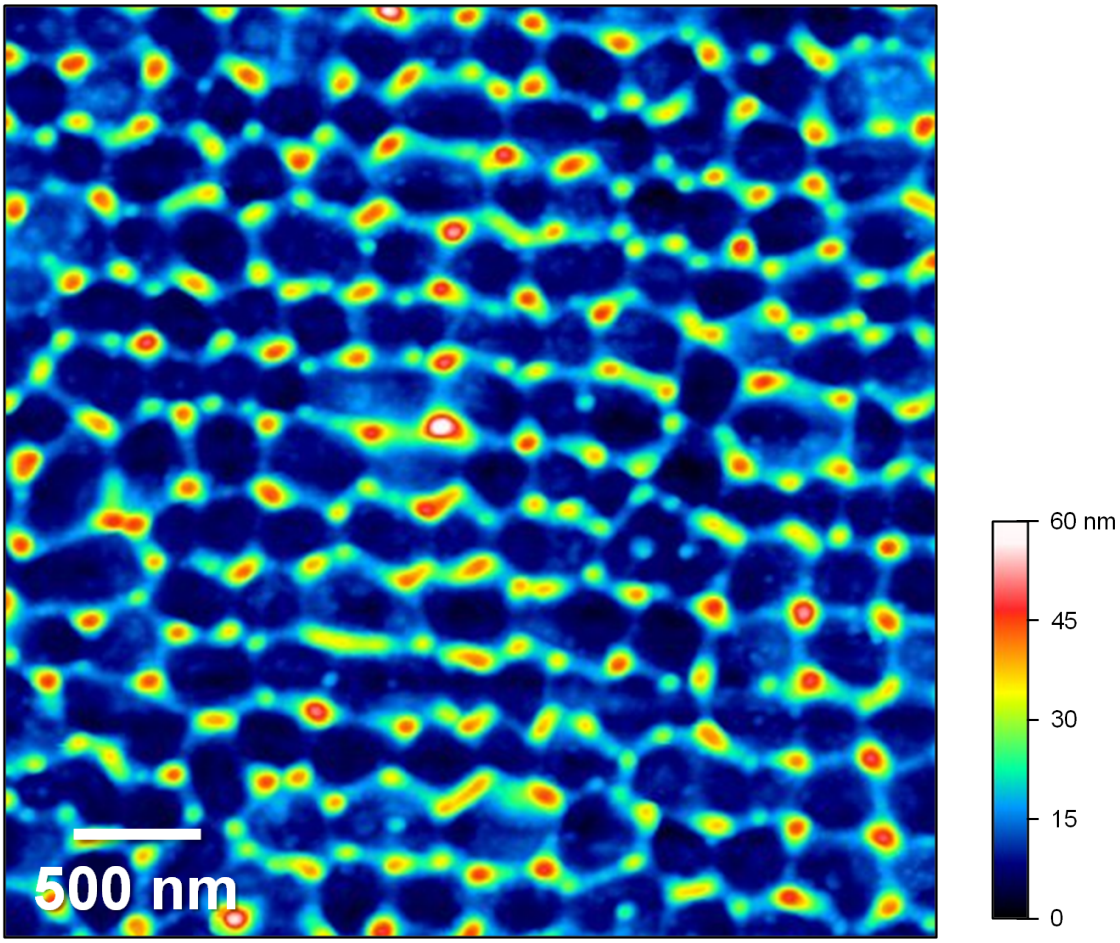

Figure 3.1: 2-D AFM surface morphology plot of a sample of the ELA poly-Si films. The color-coded scale bar represents film surface height.

laser operating at a 308-nm wavelength and with a 30-ns pulse duration at full-width half-maximum (FWHM). Due to the high absorption coefficient of silicon in the ultraviolet wavelength range, the majority of the optical energy of the incident beam was absorbed within the first ten nanometers at the irradiated film surface [76] and subsequently converted into thermal energy used to rapidly heat the film.

In order to investigate the effect of different heating rates on melting, we varied the pulse duration of the incident beam between 30 ns at FWHM and 240 ns at

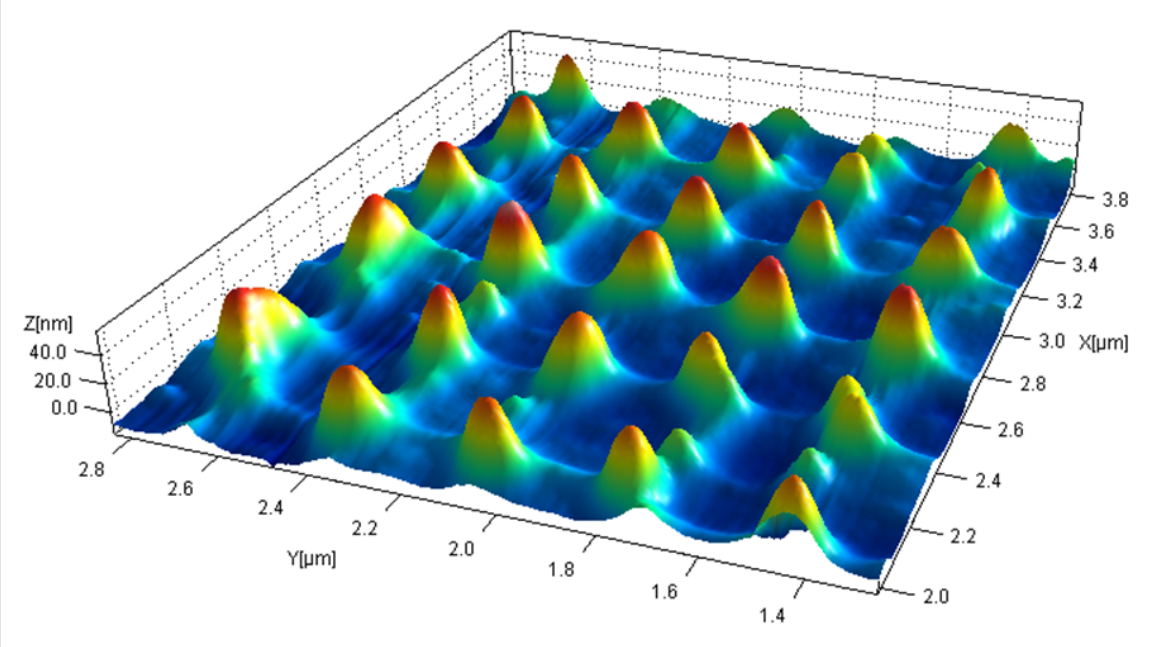

Figure 3.2: 3-D AFM surface morphology plot of a sample of the ELA poly-Si films.

FWHM. This was accomplished by re-directing the beam through an optical pulse duration extender, a device composed of a plurality of mirrors and graded-reflectivity beamsplitters used to extend the optical path length for a portion of the beam. A variable-plate attenuator was used to finely control the energy density of the incident beam, which was then monitored using a calibrated pyroelectric energy meter. After attenuation, the beam was passed through an array of beam-shaping optics including a telescope, homogenizer, field lens, and projection lens with 5× de-magnification. This resulted in a spatially homogeneous and uniform beam profile. A patterned mask was used to further define the spot size of the beam, which was set to 1 × 1 mm^2 at the irradiated film surface. Prior to irradiation, the films were translated and brought into focus with the pulsed laser using a computer-controlled sub-micron-

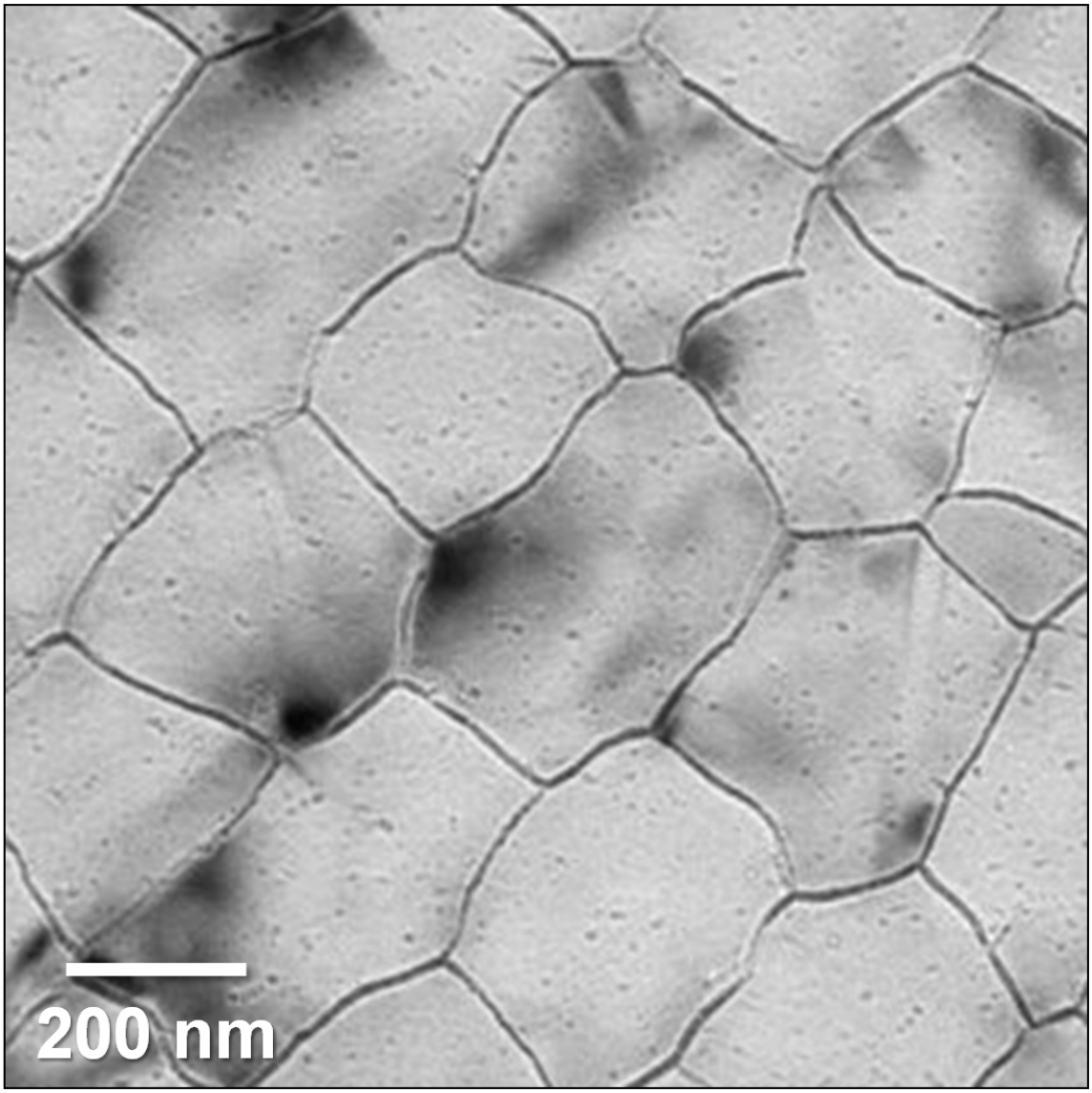

Figure 3.3: Plan-view TEM image of a sample of the ELA poly-Si films. The sample was prepared via a standard lift-off method. Light defect etching was applied before TEM imaging to enhance grain boundary contrast.

precision translation stage. All experiments were conducted in open air conditions and at room temperature.

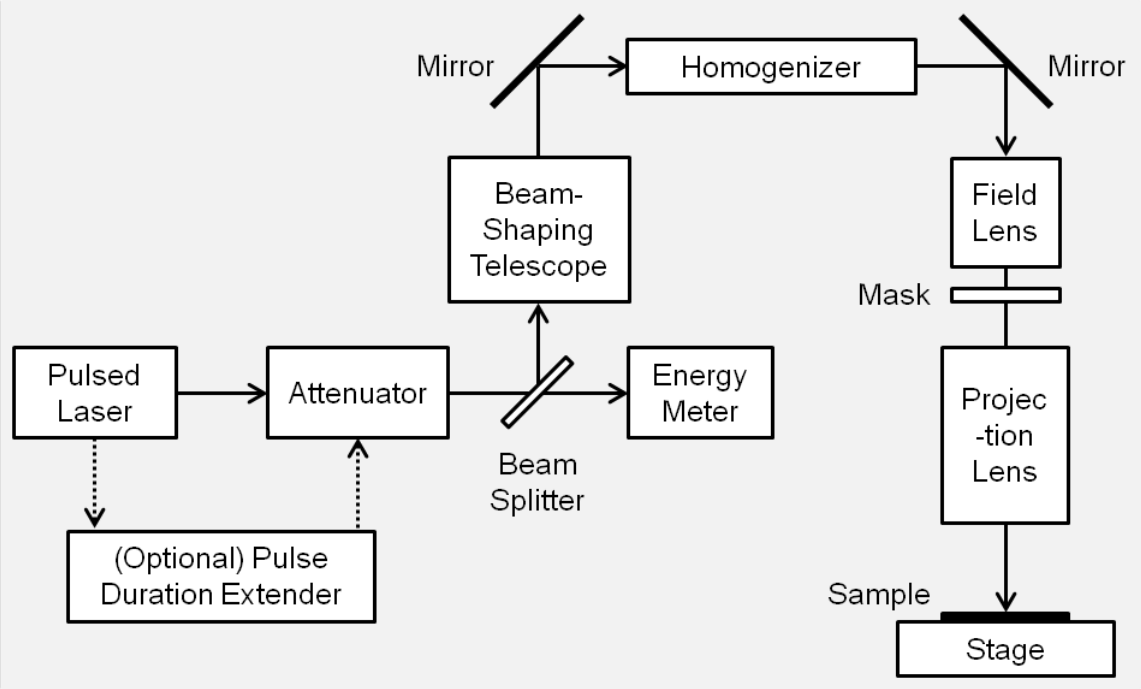

Figure 3.4: Schematic diagram illustrating the pulsed-laser system used in the experiments presented throughout this thesis.

The irradiated ELA poly-Si films sat on a SiO_2 substrate, the transparent nature of which enabled us to obtain more spatially comprehensive in situ information on how melting proceeded in the films by examining (1) the BTR signals measured at the film/substrate interface, along with the usual FTR signals measured at the film surface, and (2) the TT signals measured throughout the thickness of the films. Such signals were obtained using CW diode lasers operating at the 670-nm wavelength. The diode lasers were incident on the films at approximately 50° with respect to the surface normal. Upon reflection from (or transmission through) the films, the

diode laser beams were then focused onto a set of silicon-based rapid-response photodetectors with a 1-ns characteristic rise time. The photodetectors were equipped with ultraviolet filters used to block stray excimer-laser light from saturating the photodetectors. It was assumed that the transient reflectance and transmissions signals were collected from an area of the film under uniform irradiation since (1) the diode-laser-probed areas (75×300 um^2) were much smaller than, and meticulously centered at, the relatively large spot size of the incident beam (1×1 mm^2), and (2) the beam-shaping optics of the pulsed-laser system had already produced a highly spatially homogeneous and uniform incident beam profile.

The FTR, BTR, and TT signals were measured in situ and stored using a multiple-channel digital oscilloscope (500 MHz). Careful attention was paid during data collection to (1) ensure the signals were synchronously collected relative to each other and the triggering incident beam, and (2) minimize any artificial delay between FTR, BTR, and TT signal acquisition. A Savitsky-Golay filter was employed to smoothen the measured data and increase the signal-to-noise ratio by removing high-frequency noise components.

The present work relies greatly on these time-resolved in situ transient reflectance and transmission signals. Such signals can reveal critical spatiotemporal details associated with the rapid phase transformations occurring in the irradiated silicon films. Figure 3.5 schematically illustrates the expected variations in the transient reflectance and transmission signals corresponding to the simple and idealized 1-D and 2-D par-

tial melting and solidification scenarios (undergoing identical melt fraction versus time evolutions). In the perfectly 1-D case, the planar solid/liquid interface proceeds vertically downwards (upwards) upon melting (solidification), whereas in the perfectly 2-D case, the interface instead travels laterally outwards (inwards) upon melting (solidification). Small black (white) arrows are used to depict the direction of the solid/liquid interface during melting (solidification) in Figure 3.5.

When interpreting such reflectance and transmission signals, one must consider primarily the effects that arise from (1) the higher reflectivity of metallic liquid silicon than that of solid silicon [25], and (2) thin-film interference effects [77] that arise either from the dynamic change of the thickness of the solid in the case of 1-D melting of the film (captured in Figure 3.5), or changes in the temperature-dependent refractive indices of the film during solid-phase heating (not depicted in Figure 3.5).

In contrast to Figure 3.5, which illustrates the cases pertaining to partial melting, Figure 3.6 schematically shows the expected variations in the FTR, BTR, and TT signals corresponding to the idealized 1-D and 2-D *complete* melting scenarios. The process of solidification is omitted in Figure 3.6.

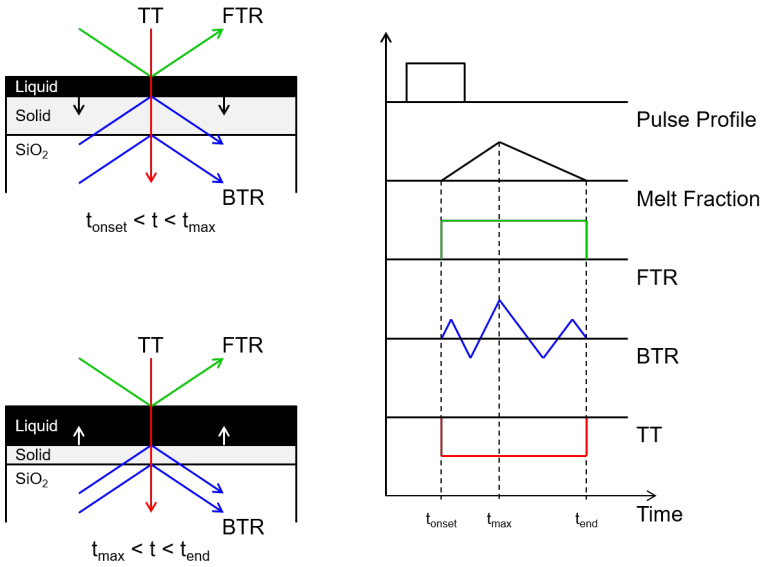

(a)

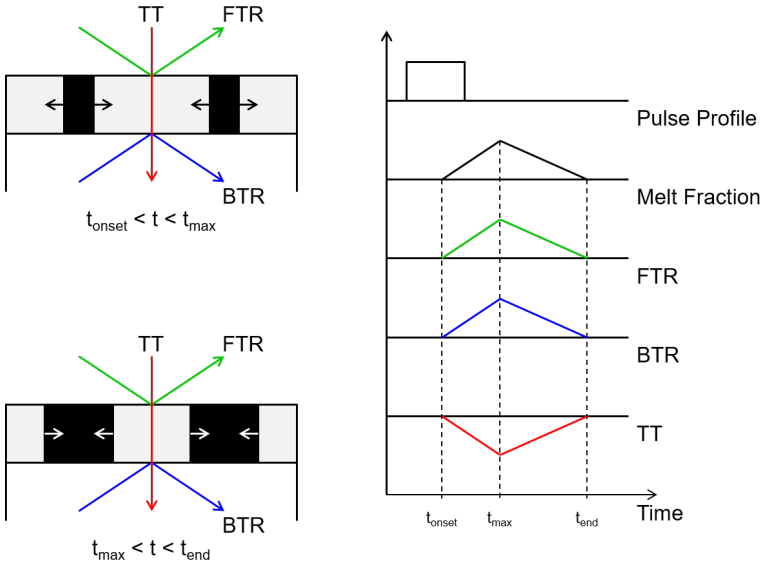

(b)

Figure 3.5: Schematic diagram illustrating the perfect (a) 1-D, and (b) 2-D melting and solidification scenarios for a silicon film on SiO_2 undergoing pulsed-laser-induced partial melting. Corresponding FTR, BTR, and TT signals, as well as melt fraction, are plotted as a function of time relative to the incident laser pulse profile. The onset and end of melting occur at times t_{onset} and t_{end}, respectively, and the maximum extent of (partial) melting occurs at time t_{max}. Changes in the temperature-dependent refractive indices of the film and skin depth effects are neglected for simplicity.

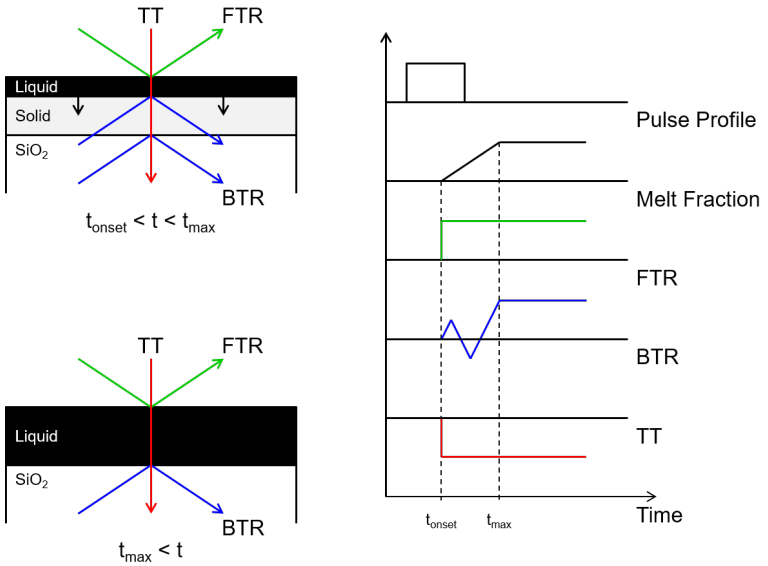

(a)

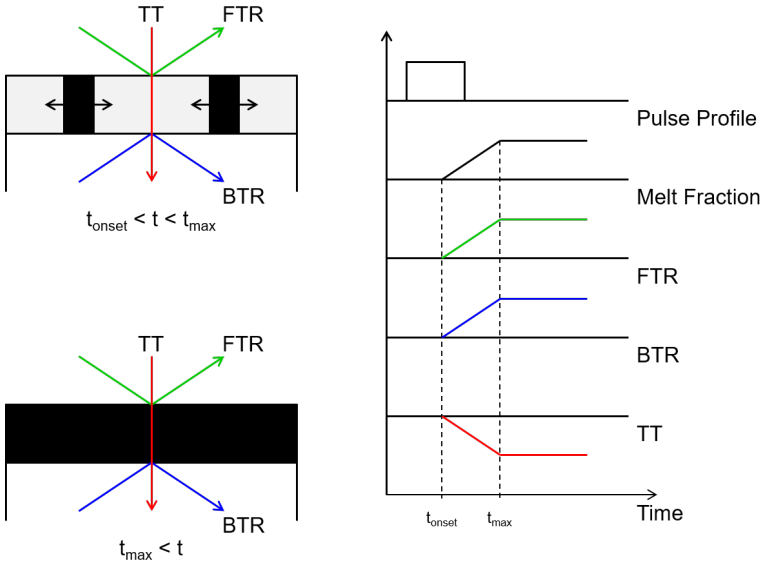

(b)

Figure 3.6: Schematic diagram illustrating the perfect (a) 1-D, and (b) 2-D melting scenarios for a silicon film on SiO_2 undergoing pulsed-laser-induced complete melting (subsequent nucleation-initiated solidification is not shown here). Corresponding FTR, BTR, and TT signals, as well as melt fraction, are plotted as a function of time relative to the incident laser pulse profile. The onset of melting occurs at time t_{onset} and complete melting of the film occurs at time t_{max}, after which the film remains completely molten until nucleation-initiated solidification takes place (not shown here). Changes in the temperature-dependent refractive indices of the film and skin depth effects are neglected for simplicity.

3.3 Experimental Results

3.3.1 Melting in ELA Poly-Si Films Using a Pulsed-Extended Beam Profile

We first present experimental results obtained using the incident beam passed through the optical pulse duration extender. The resulting beam, shown in Figure 5.7(b), consists of a single-pulse profile with a pulse duration of 240 ns at FWHM (minor fluctuations overlaid on top of the primary pulse profile are artifacts of the pulse extender).

Figure 3.7(a) shows FTR, BTR, and TT signals that were obtained from irradiating the ELA poly-Si film using such a pulse-extended incident beam at an energy density just below the CMT. The signals here, and subsequent presented signals, are normalized to the CMT and positioned for easy visual comparison. Based upon the aforementioned transient reflectance and transmission signal considerations enumerated above, we identify the initial oscillation (i.e., rise and drop) observed in the FTR and BTR signals, as well as the initial gradual reduction in the TT signal, as arising from simple solid-phase heating, whereas the subsequent variations in the signals are attributed to actual melting and solidification proceeding largely in a 2-D manner.

Figure 3.8 shows FTR, BTR, and TT signals that were obtained using a pulse-extended incident beam at various energy densities. At energy densities above the CMT, the appearance of the plateau in the signals indicates that the films have

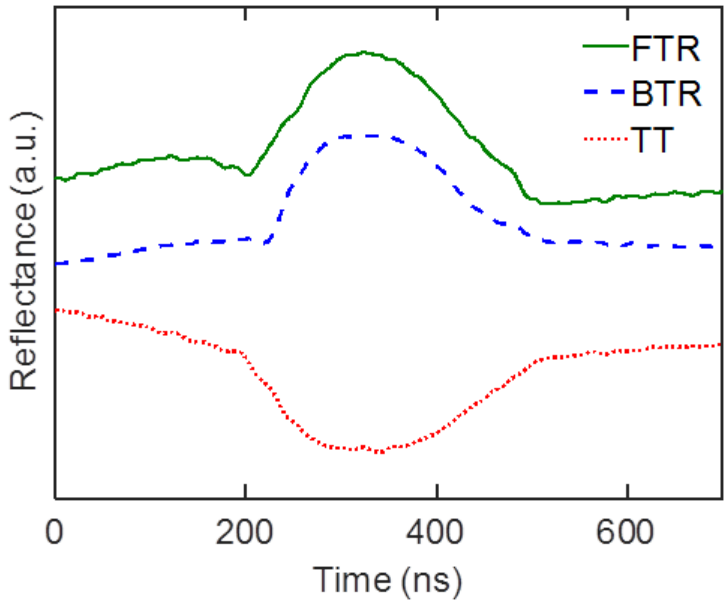

(a)

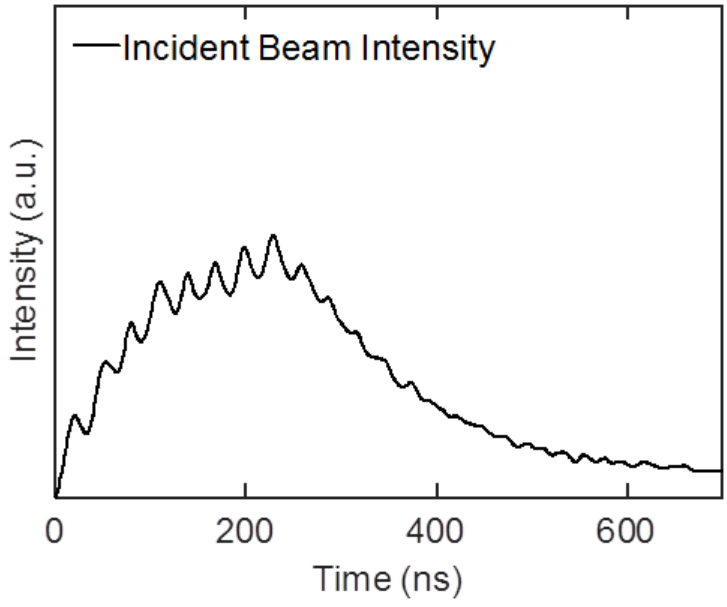

(b)

Figure 3.7: (a) In situ FTR, BTR, and TT signals measured during irradiation of the ELA poly-Si film at 0.98 CMT. (b) Experimentally extracted time-dependent intensity profile of the pulse-extended incident beam.

become fully molten (i.e., prompting the FTR, BTR, and TT signals to saturate where they remain until the nucleation of solids triggers the onset of solidification, and thus causing the FTR and BTR signals to drop and the TT signals to rise [78]). The most striking feature corresponds to the absence of a plateau observed in the FTR signals even when the films are irradiated with relatively high incident energy densities up to the CMT. This indicates, along with the matching TT profiles, that the irradiated film surface is not fully melted nearly up to the point in time at which complete melting starts to be substantially manifested.

In contrast, Figure 3.9(a) shows FTR and BTR signals that were obtained from irradiating a single-crystal silicon film on SiO_2 (the details of which are described in [55]) using the same pulse-extended incident beam at an energy density below the CMT. Beyond the initial oscillation caused by solid-phase heating, the prompt appearance of a plateau in the FTR signal signifies that the irradiated film surface undergoes complete surface melting. Subsequent oscillations observed in the BTR signal are ascribed to thin-film interference effects arising from the creation and movement of a planar solid/liquid interface propagating down towards the substrate (during melting) and up towards the film surface (during solidification) in a largely 1-D manner. Such prominent signal features, when compared to those measured in a nearly identically irradiated ELA poly-Si film (shown in Figure 3.9(b)), suggest that the presence, or absence, of grain boundaries can greatly affect the melting and solidification transformations in pulsed-laser irradiated silicon films.

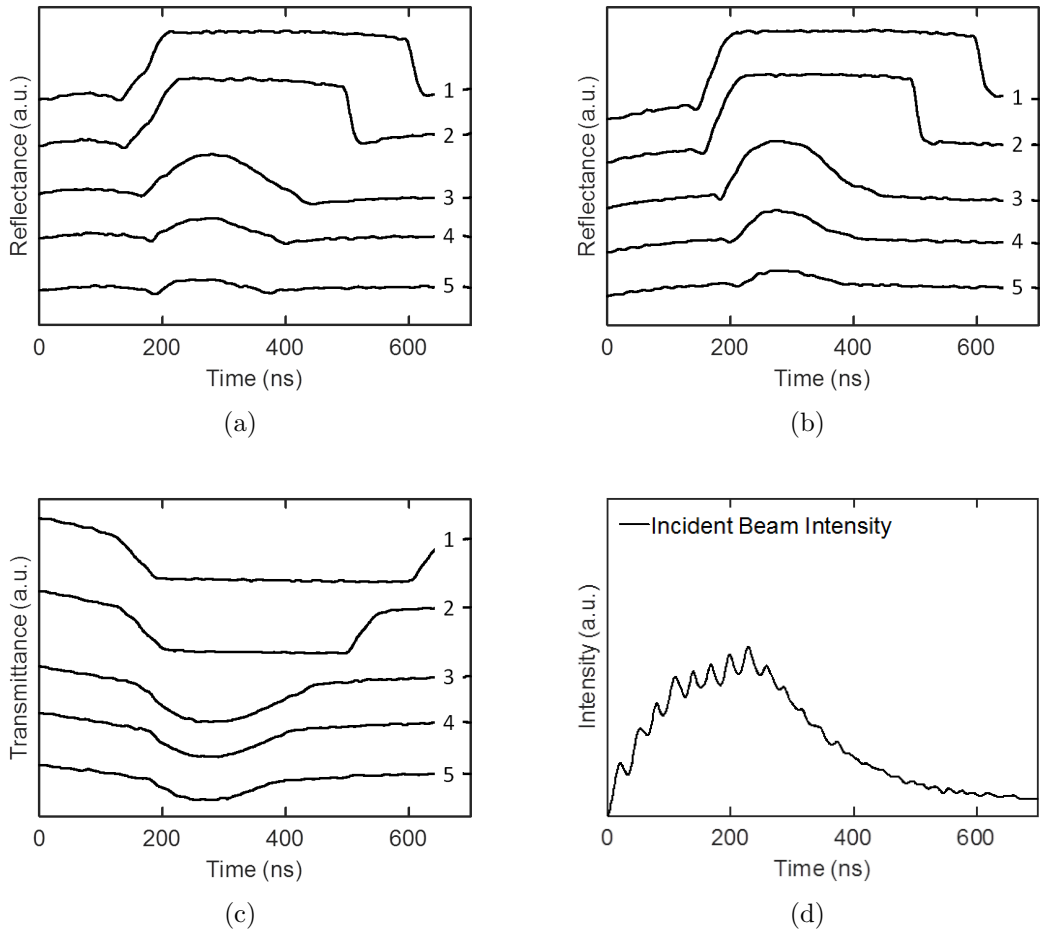

Figure 3.8: In situ (a) FTR, (b) BTR, and (c) TT signals measured during irradiation of the ELA poly-Si films at various incident energy densities. The corresponding energy densities (normalized to the CMT) are: (1) 1.26, (2) 1.10, (3) 0.92, (4) 0.85, and (5) 0.81 CMT. (d) A representative profile of the pulse-extended incident beam.

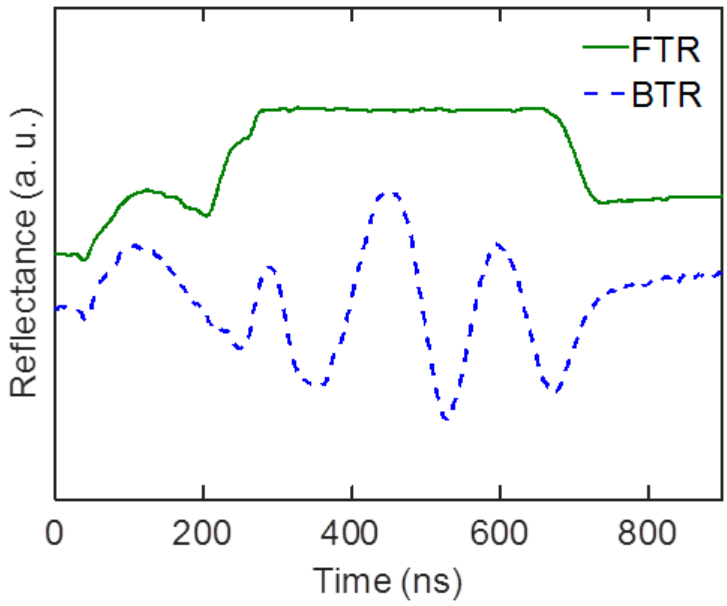

(a)

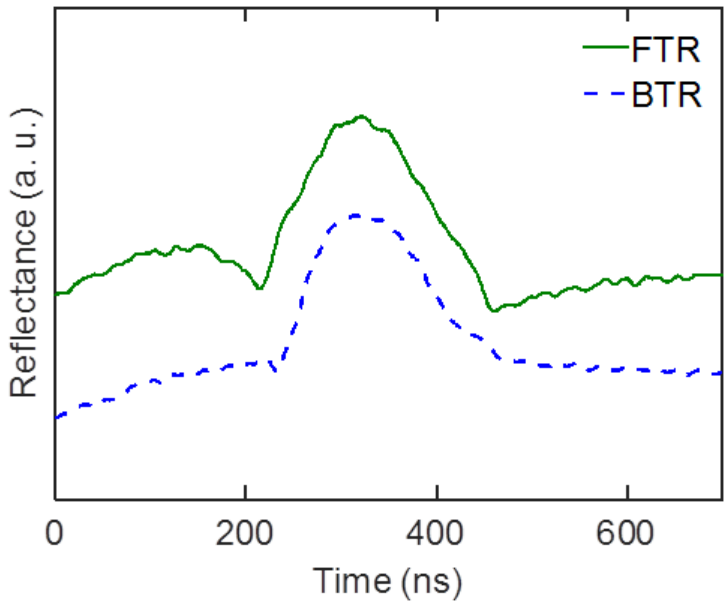

(b)

Figure 3.9: In situ FTR and BTR signals measured during irradiation of (a) the 200-nm-thick single-crystal silicon film, and (b) the 50-nm-thick ELA poly-Si film both at 0.89 CMT. A representative profile of the pulsed-extended incident beam is shown in Figure 5.7(b).

Surface melt fractions at the top (surface-side) and bottom (substrate-side) surfaces of the irradiated ELA poly-Si films can be estimated from the collected FTR and BTR signals, respectively (keeping in mind that the absolute value of the FTR and BTR signals increases with increasing melt fraction and saturates upon complete surface melting). Figure 3.10 shows the approximated maximum melt fraction sustained at the surface-side and substrate-side of the irradiated ELA poly-Si films at various energy densities using the pulse-extended beam. At energy densities below the partial-melting threshold (PMT), or the threshold at which liquid begins to form, melting is not observed at either the surface-side nor substrate-side of the film. However, at energy densities even just above the PMT, melting is observed (i.e., melt fraction > 0) at both the surface-side and substrate-side of the film. This observation, in combination with the fact that the irradiated surface-side of the film is never fully melted (i.e., melt fraction < 1) even at energy densities up to the CMT, shows that melting in these irradiated ELA poly-Si films does not proceed in a simple 1-D manner.

3.3.2 Melting in ELA Poly-Si Films Using an Unmodified Beam Profile

Next, we present experimental results obtained using the incident beam with an unmodified beam profile (i.e., non-pulse-extended). Such a beam profile, shown in Figure 5.7(a), is similar to the profile used during actual ELA processing and is

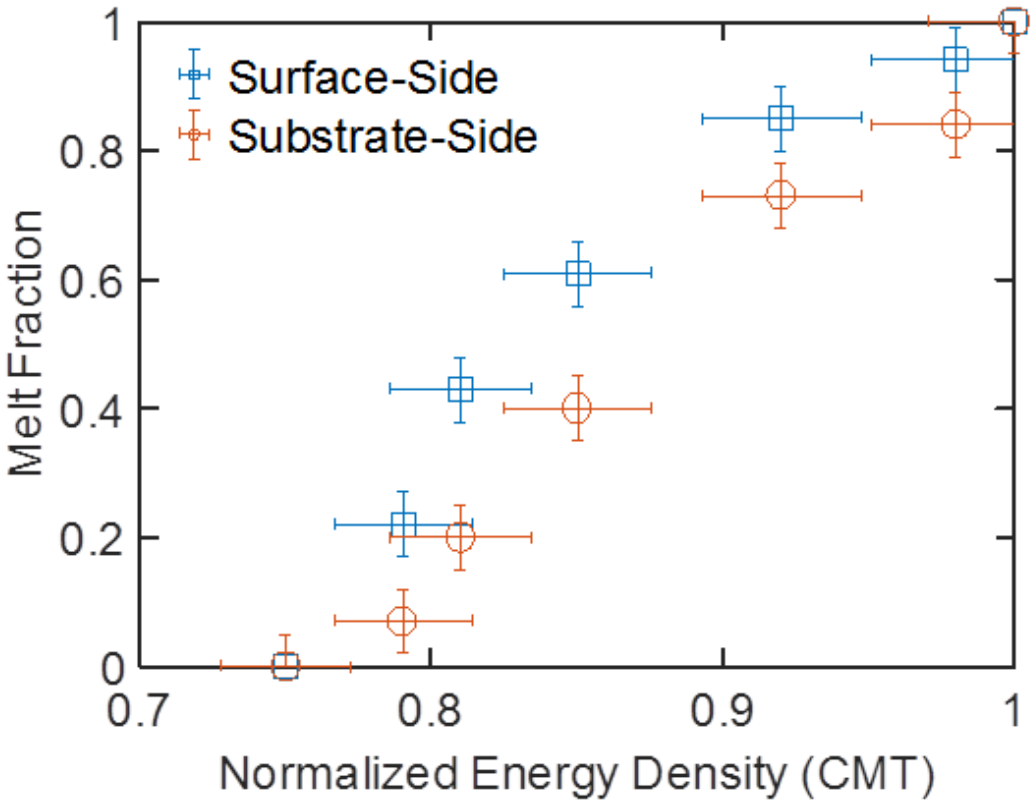

Figure 3.10: Maximum surface-side and substrate-side melt fractions extracted from in situ FTR and BTR signals, respectively. Such signals were measured during irradiation of the ELA poly-Si films at various energy densities using the pulse-extended beam. A representative profile of the pulse-extended incident beam is shown in Figure 5.7(b).

characterized by a 30-ns primary pulse at FWHM, followed by secondary and tertiary pulses. The magnitude of these non-primary pulses, relative to the primary pulse, increases with increasing age of the xenon-chloride laser gas.

Figure 3.11(a) shows FTR, BTR, and TT signals that were obtained from irradiating the ELA poly-Si film at an energy density just below the CMT. Again, we identify the initial oscillation observed in the FTR and BTR signals, as well as the gradual

reduction in the TT signal, as arising from changes in the temperature-dependent refractive indices of the film during solid-phase heating. Subsequent variations in the signals are attributed to actual melting and solidification occurring largely in a 2-D manner. The additional variations in the signals can be precisely and trivially correlated to the measured time-dependent intensity profile of the incident beam shown in Figure 5.7(a).

Figure 3.12 shows FTR, BTR, and TT signals that were obtained at various energy densities. Once more, a plateau is observed in the signals that were obtained at energy densities above the CMT, which signifies that the films have undergone complete melting. This saturation in signal persists until the onset of nucleation-initiated solidification causes the FTR and BTR signals to drop and the TT signal to rise. However, note the marked absence of such a plateau in the FTR signals (as well as in the corresponding BTR and TT signals) even at energy densities just below the CMT. This lack of plateau indicates that the irradiated film surface is not fully melted (1) even at relatively high incident energy densities up to the CMT, and (2) despite the short-pulse and rapid-heating nature of the incident beam used here (relative to the previously discussed pulse-extended beam cases).

In contrast, Figure 3.13(a) shows FTR and BTR signals that were obtained from irradiating a single-crystal silicon film on SiO_2 at an energy density just below the CMT. As was observed in the pulse-extended beam experiments, a plateau in the FTR signal promptly appears upon irradiation, thus indicating that the irradiated

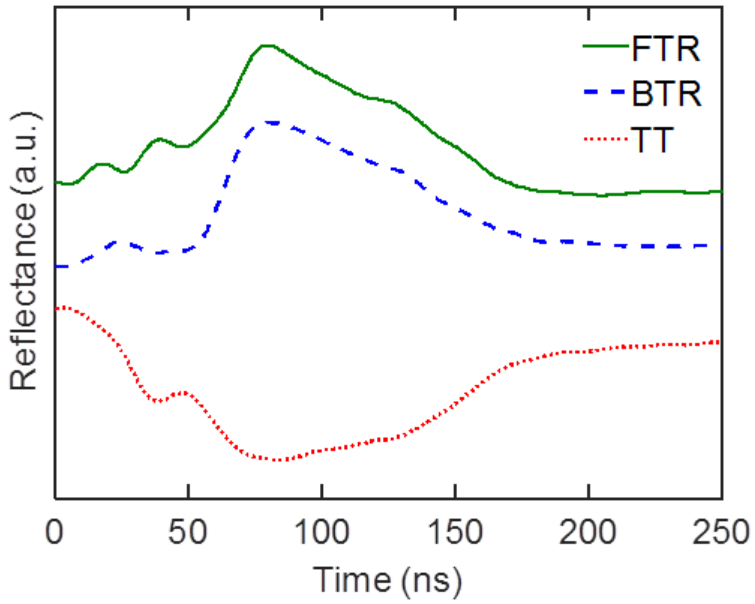

(a)

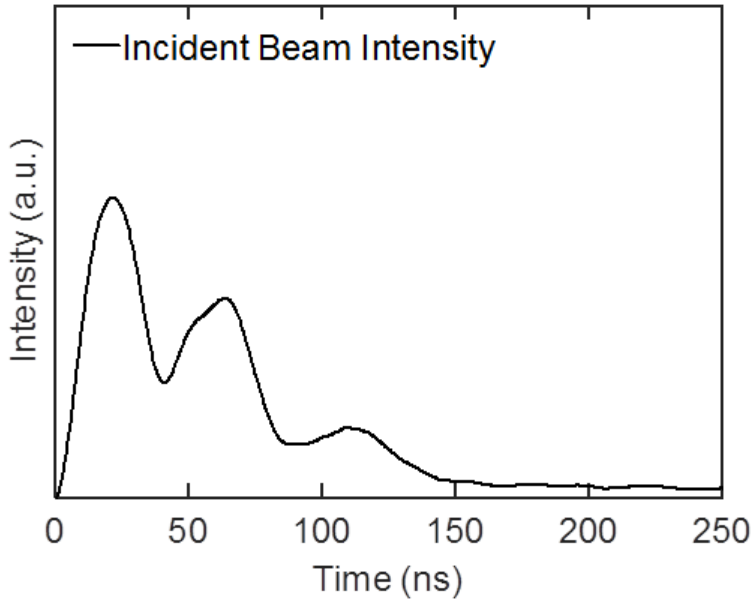

(b)

Figure 3.11: (a) In situ FTR, BTR, and TT signals measured during irradiation of the ELA poly-Si film at 0.96 CMT. (b) Experimentally extracted time-dependent intensity profile of the incident beam.

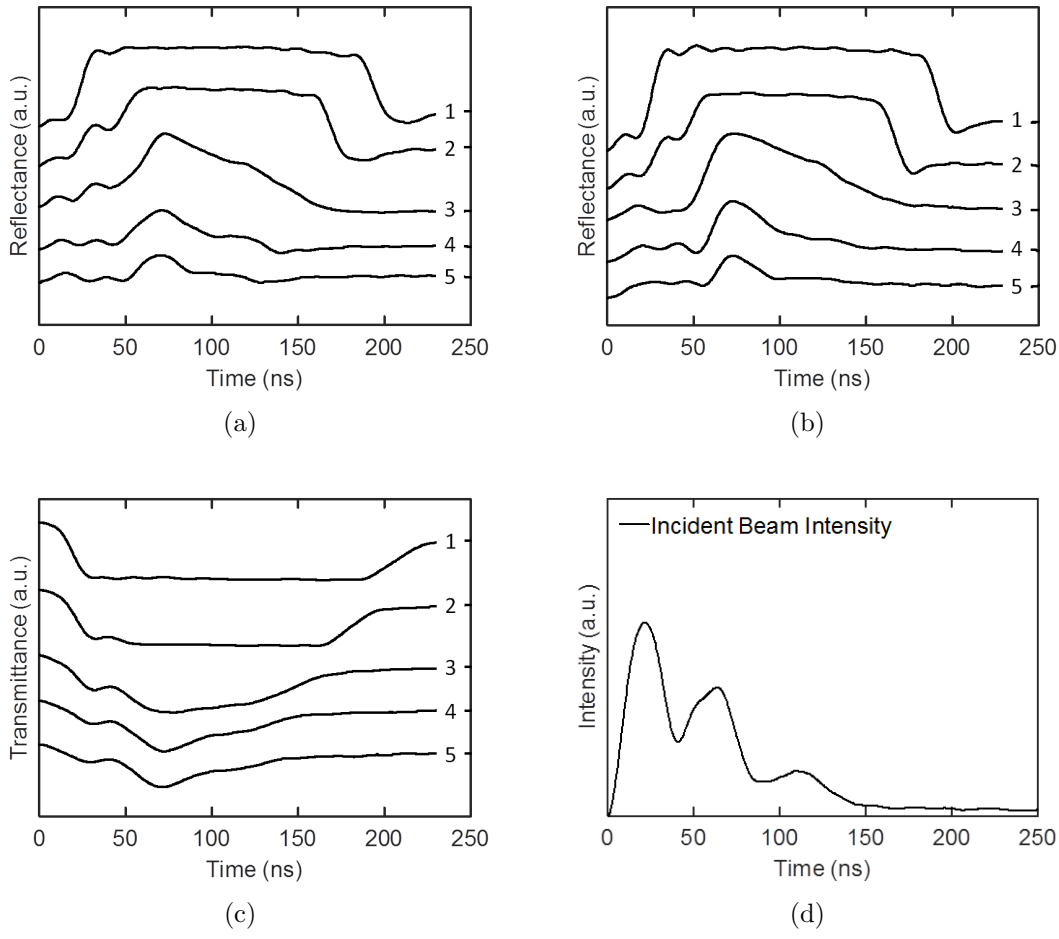

Figure 3.12: In situ (a) FTR, (b) BTR, and (c) TT signals measured during irradiation of the ELA poly-Si films at various incident energy densities. The corresponding energy densities (normalized to the CMT) are: (1) 1.32, (2) 1.17, (3) 0.96, (4) 0.87, and (5) 0.81 CMT. (d) A representative profile of the incident beam.

surface of the film readily undergoes complete melting even though the energy of the incident beam was kept below the CMT. The FTR plateau formation is followed by oscillations in the BTR signal caused by thin-film interference effects arising from a planar solid/liquid interface propagating in a predominately 1-D manner. Distinct signal features such as these are starkly different to the signals obtained in the almost identically irradiated ELA poly-Si films, which are shown in Figure 3.13(b). Such results affirm the significant role grain boundary and grain junction regions can play in affecting the pulsed-laser-induced melting and solidification behavior of these columnar-grained silicon films.

Figure 3.14 shows the approximated maximum melt fraction sustained at the surface-side and substrate-side of the irradiated ELA poly-Si films at various energy densities. Such data are extracted from corresponding FTR and BTR signals measured during irradiation. It is important to note that despite using a shorter pulse duration incident beam here (30-ns at FWHM), resulting in increased heating rates and greater temperature gradients across the thickness of the film, the irradiated film surface does not fully melt even at energy densities up to the CMT (i.e., surface-side melt fraction < 1). Such findings underlie the very basis of this thesis, which argues not for a 1-D, but instead, for a 2-D melting model in irradiated ELA poly-Si films whereby localized complete melting takes place throughout the film thickness, followed by lateral 2-D melting.

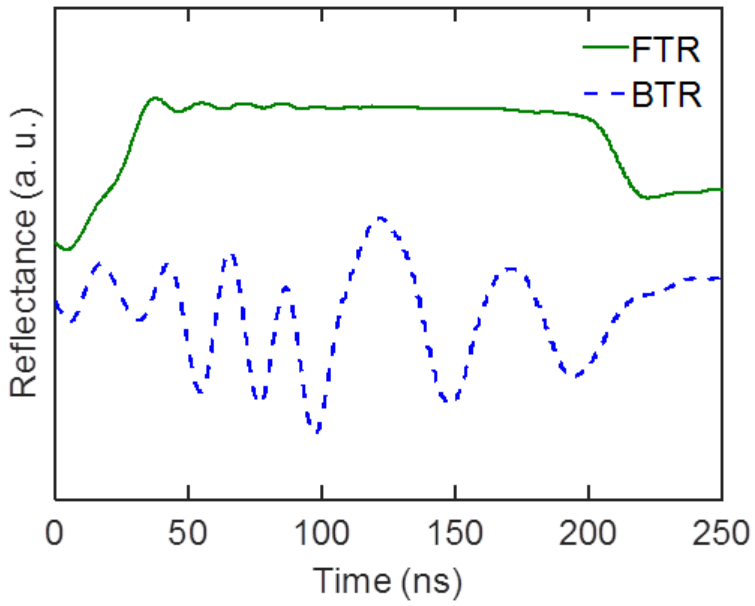

(a)

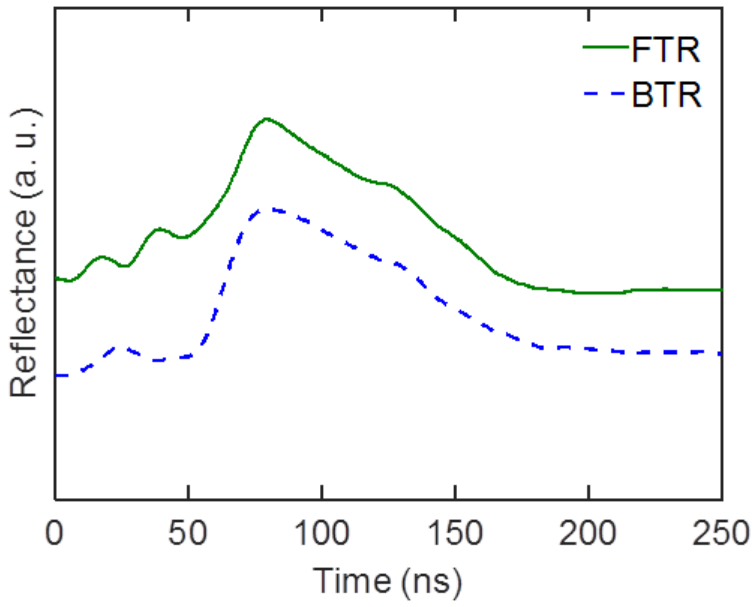

(b)

Figure 3.13: In situ FTR and BTR signals measured during irradiation of (a) the 200-nm-thick single-crystal silicon film, and (b) the 50-nm-thick ELA poly-Si film both at 0.96 CMT. A representative profile of the incident beam is shown in Figure 5.7(a).

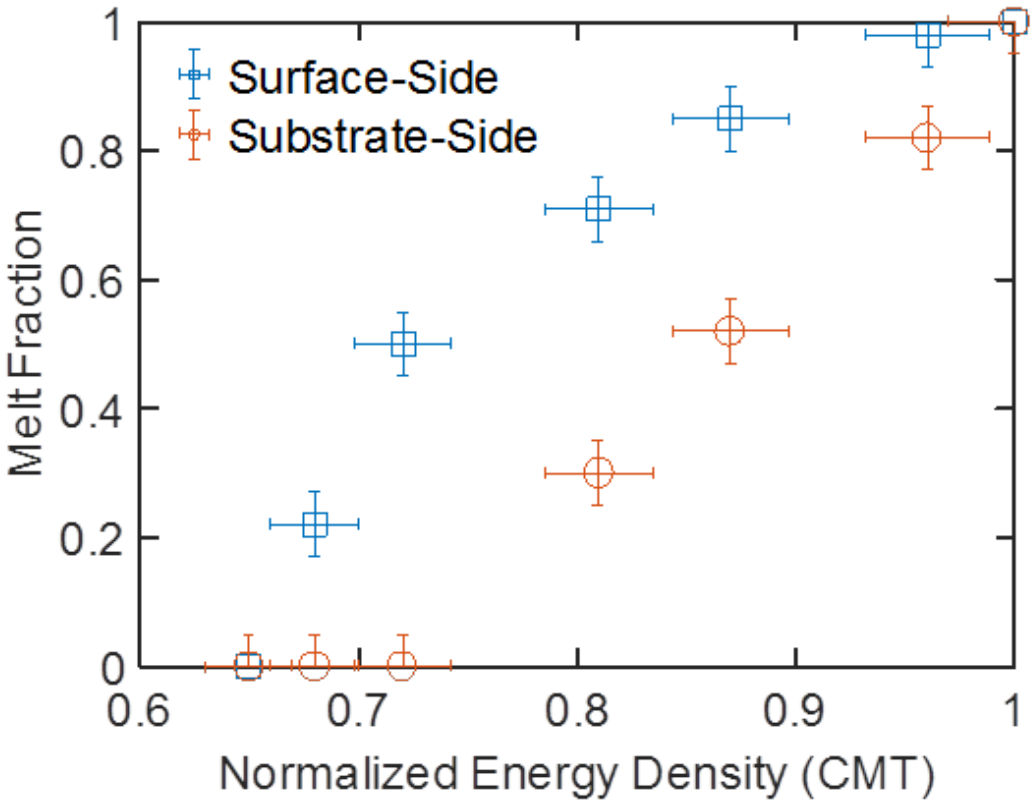

Figure 3.14: Maximum surface-side and substrate-side melt fractions extracted from in situ FTR and BTR signals, respectively. Such signals were measured during irradiation of the ELA poly-Si films at various energy densities. A representative profile of the incident beam is shown in Figure 5.7(a).

3.4 Discussion

We conclude from the experimental results presented above that the melting and solidification transformations in pulsed-laser irradiated ELA poly-Si films occur in a remarkably and largely 2-D manner. This nature of the ELA process represents, based on considering the extent of understanding regarding the mechanism of melting and solidification as manifested in previously published articles on melt-mediated

crystallization of polycrystalline films, the most salient finding of this thesis. We currently consider that appreciating this 2-D nature of melting is an important step for understanding and mastering the ELA process.

The 2-D melting behavior observed in these poly-Si films composed of small and columnar grains is in stark contrast to the predominantly 1-D melting behavior observed in single-crystal silicon films under identical irradiation conditions. Previously, we have recognized that simple 1-D melting of small-columnar-grained poly-Si films cannot possibly lead to the gradual microstructure evolution observed in the ELA process as the continuous bottom solid layer consisting of unmelted portions of grains will then simply regrow epitaxially and vertically to fully recover the pre-melting microstructure [17]. Instead, we have suggested, based on TEM analysis of the microstructure evolution observed in multiple-pulse irradiated poly-Si films, that localized complete melting of the films must at least take place at and near the columnar grain boundaries. It was suggested, furthermore, that the asymmetric extent of melting and/or solidification between adjacent grains, as influenced by various physical and thermodynamic factors, such as grain size, orientation, thickness, and defect density, for example, will then eventually lead to the apparent growth of some grains, and the effective shrinkage and/or full elimination of others. These are the factors that underlie the gradual increase in the average grain size and subsequent evolution in the overall grain size distribution with each pulse-induced melting-and-solidification cycle encountered in ELA.

The current discovery regarding the 2-D nature of melting in ELA poly-Si films is firstly consistent with the above suggestions. Secondly, it adds to the argument that, during the melting transition, at least some portion of the unmelted columnar grains, which according to the above suggestions must correspond to the interior of the grains, remains entirely solid throughout the thickness of the film. This is manifested by the striking absence of a plateau in the FTR signals, as well as the BTR and TT signals, during (partial) melting of the films. Figure 3.15 schematically illustrates an interpretation of the evolution of events that, we argue, transpire during asymmetrical and predominately 2-D melting between grains in irradiated columnar-grained poly-Si films. This 2-D melting behavior may be argued and appreciated as stabilizing and extending the degree to which lateral melting of the grains occurs in ELA poly-Si films. That, in turn, will enable and facilitate the microstructure evolution of the grains observed in the ELA process, where, with repeated irradiation of the films, one observes (1) a gradual increase in the average grain size, and (2) the alignment and arrangement of the grain boundaries to form a rather unusual polycrystalline microstructure consisting of relatively regular and periodic grains (as affected by the laser-induced periodic surface structures (LIPSS) effect [73]). Indeed, we suggest, as will be described in detail later in this thesis, that the present "2-D melting model" can now provide a comprehensive and consistent explanation for how the formation of local hot spots via beam scattering resulting from the non-planar surface morphology of the columnar grains can gradually, iteratively, and cyclically assist (and be also

assisted by) the lateral melting process (which leads to the subsequent formation of surface protrusions in the last-to-laterally-solidify grain boundary and grain junction regions) to enable the periodic formation of 300-nm grains [79].

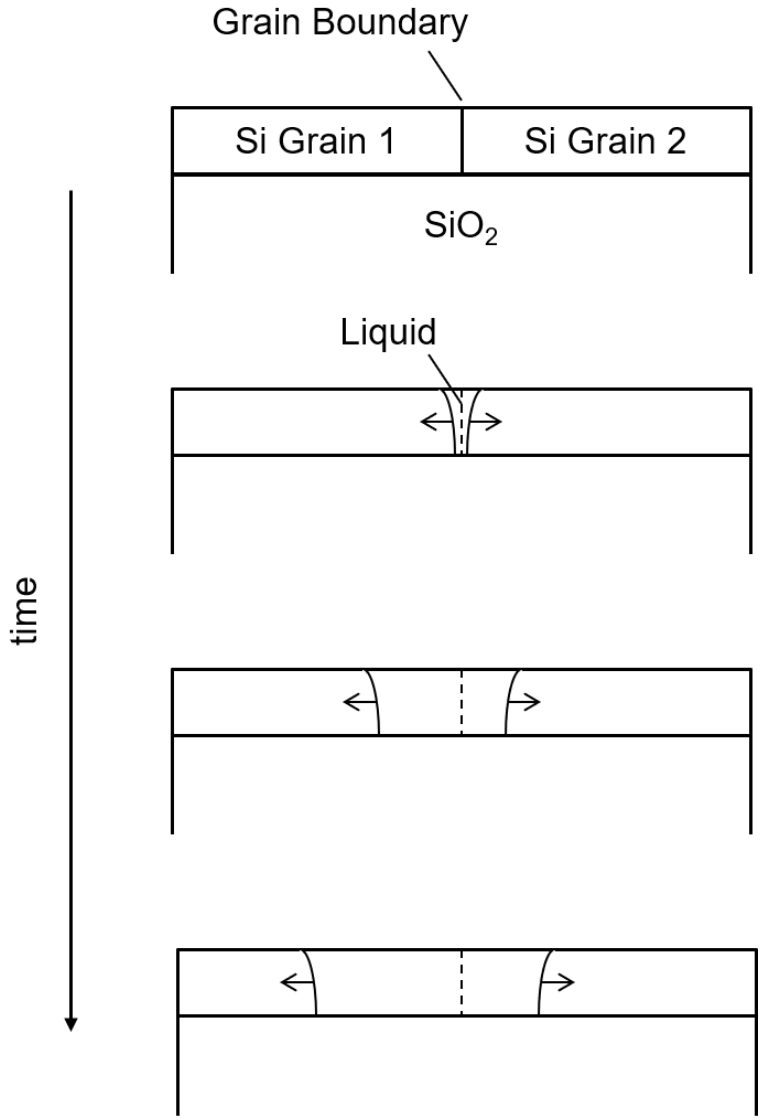

Figure 3.15: A schematic diagram illustrating asymmetrical and predominately 2-D melting between grains in a columnar-grained poly-Si film.

As was discussed previously [17][58], it is not difficult to account for the aggres-

sive participation of grain boundaries and grain junctions in initiating the melting transition. High-angle grain boundaries and grain junctions represent high-excess-free-energy sites where liquid can preferentially and heterogeneously form with very little thermodynamic resistance. Enhanced absorption of the incident beam at grain boundaries may also support this notion [80]. In contrast, an important but less self-evident element of our suggested model corresponds to the superheating of the interior of the columnar grains during 2-D melting of the ELA poly-Si films. The expected thermal profile dictates that, due to (1) the beam being "incident on the grains" during the melting phase of the process, (2) the grain boundaries melting at least near, or possibly slightly above, the equilibrium melting point, (3) the rapid interface movement reflecting that a non-negligible degree of superheating is taking place, and (4) the interfacial decalescence transpiring at the melt-front (as melting is an endothermic process), there must transiently be substantial superheating at the grain interiors. The greatest degree of superheating is expected at the top and center portions (away from the heat-consuming melting interfaces initiated at the boundaries of the grains) of the grains during the melting phase of the irradiated films. Quantitative analysis of the temperature profile of ELA poly-Si films under pulsed-laser irradiation (and the degree to which superheating proceeds in individual grains) are presented in Chapter 6.

3.5 Summary

In summary, we show via transient reflectance and transmission analysis that ELA-prepared poly-Si films consisting of small and columnar grains melt in a remarkably and largely 2-D manner upon pulsed-laser irradiation. We attribute this 2-D melting behavior to (1) localized complete melting transpiring promptly at melt-prone grain boundary and grain junction regions, and (2) subsequent melting proceeding laterally into the transiently superheated interior of the unmelted grains. We suggest that this 2-D nature of melting should be recognized and appreciated as being a critical process-enabling element of the ELA process, as it facilitates the gradual microstructure evolution observed in multiple-pulse irradiated poly-Si films.

Chapter 4

The Significance of Grain Boundary Melting and SiO_2 Surface Passivation

4.1 Introduction

As was discussed in the previous chapter, the presence (or absence) of grain boundary and grain junction regions in silicon films plays a dominant role in affecting the manner in which pulsed-laser-induced melting proceeds. However, in addition to grain boundaries, other factors inherent to the ELA process, such as incident beam "hot spots" and/or passivating surface layers, can also influence the melting transition (as discussed below). In order to gain a more comprehensive understanding of the

fundamental melting mechanisms involved during ELA, we examine here the impact of these factors (hot spots and surface passivation) on melting in poly-Si films under pulsed-laser irradiation.

We begin this chapter by first investigating melting in ELA poly-Si films under uniform irradiation conditions, where incident beam hot spots are purposely mitigated at the irradiated film surface. The generation of hot spots is commonplace in a wide variety of materials under laser irradiation [73] and created via coupling between the incident beam and non-planar surface features, such as protrusions or depressions, at the surface of the film [81].

In an aim to preclude hot spots from our melting experiments (as these hot spots will inevitably participate in affecting the local thermal profile of the irradiated films and, as a result, can assist the films to melt in a more 2-D manner), we irradiate our samples through the bottom transparent SiO_2 substrate (i.e., substrate-side irradiation), which, we assume, lends itself to a more uniform deposition profile of the incident beam energy at the flat silicon film/SiO_2 substrate interface. This is in contrast to the experiments of Chapter 3 where samples were irradiated at the top film surface (i.e., surface-side irradiation) containing periodic surface protrusions at the grain boundary and grain junction regions, and, thus, resulted in the formation of periodic hot spots. In situ transient reflectance and transmission measurements reveal that despite the absence of incident beam hots, melting continues to proceed in a remarkably 2-D manner in these uniformly irradiated (via substrate-side irradiation)

ELA poly-Si films.

In the latter half of this chapter, we investigate the effects of a passivating surface oxide layer (i.e., native SiO_2 layer) on melting during ELA processing of silicon films. Recent work has demonstrated the ability for the Si/SiO_2 interface to sustain a large degree of superheating [55] prior to liquid initiation, which may promote 2-D melting behavior in irradiated films. Therefore, we examine the melting transition in ELA poly-Si films pre-treated with BHF solution, which serves to remove and prevent the reformation of the surface oxide layer prior to pulsed-laser irradiation. In situ FTR, BTR, and TT measurements show that despite the complete etching of the surface oxide layer (and subsequent creation of a melt-prone free surface, which is presumably conducive for melting to take place in a 1-D manner initiated via prompt complete surface melting), melting in these BHF-treated ELA poly-Si films transpires in a predominately 2-D manner. We argue that some degree of deviation from the perfect 1-D melting scenario should be expected because of (1) hot-spot creation due to incident beam scattering at the film surface (via surface-side irradiation), and (2) the non-uniform heterogeneous nature of the polycrystalline film surface as it contains grain boundaries and grain junctions.

The findings of this work lead us to conclude that it is primarily the microstructure of these thin and polycrystalline films consisting of small and columnar grains that largely determines the manner in which pulsed-laser-induced melting proceeds. While other various factors such as incident beam hot spots and passivating surface layers

can, to some degree, affect the melting process, it is, we find, the presence of grain boundary and grain junction regions that constitutes the dominant (and intrinsic) mechanism of melting in the ELA process.

4.2 Experimental Setup

The experiments described in this chapter were performed using the same ELA poly-Si film samples, pulsed-laser system, and in situ transient reflectance and transmission setup described in the previous chapter. All samples were irradiated in open air conditions and at room temperature.

In the first set of experiments, the ELA poly-Si films, as well as transient reflectance and transmission measuring probes, were arranged in such a way to enable substrate-side irradiation of the films, where the incident beam energy is first transmitted through the transparent bottom SiO_2 substrate and then deposited at the flat silicon film/SiO_2 substrate interface. This unconventional irradiation configuration avoids the generation of hot spots and thereby produces a more uniform thermal profile at the irradiated buried interface. Figure 4.1 schematically illustrates this substrate-side irradiation configuration, in addition to the usual surface-side irradiation configuration, along with the direction of the FTR, BTR, and TT measuring probes used. Film surface roughness is not depicted for the sake of simplicity.

The next set of experiments were carried out on ELA poly-Si films pre-treated with BHF solution used to first remove and then subsequently prevent the reformation of

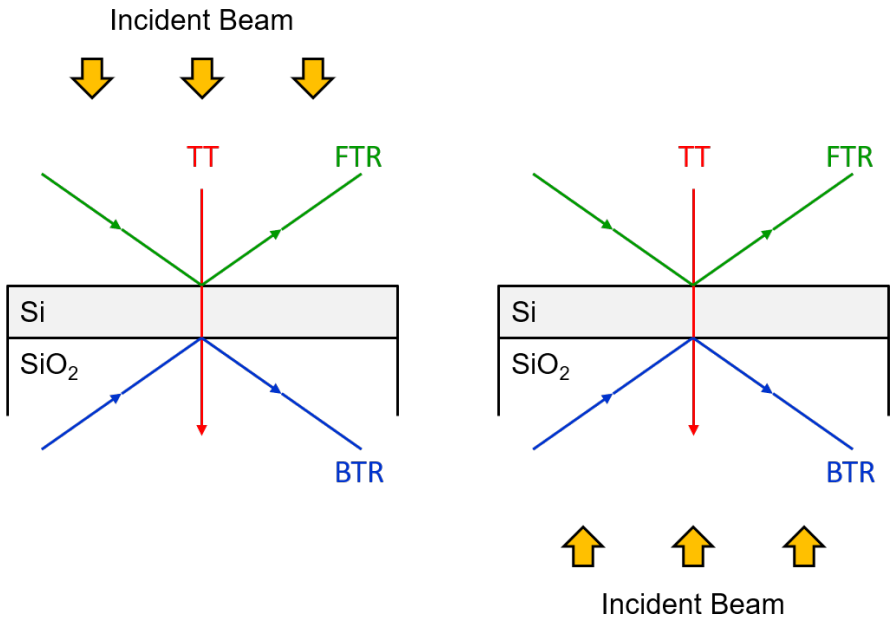

Figure 4.1: Schematic diagrams illustrating and contrasting the (a) usual surface-side irradiation configuration, and (b) unconventional substrate-side irradiation configuration for a silicon film on a transparent SiO_2 substrate. The direction of the FTR, BTR, and TT measuring probes are depicted for both configurations. Film surface roughness is not depicted for the sake of simplicity.

any oxide layer at the surface of the film prior to irradiation. The treatment consisted of fully immersing the films in a BHF solution for approximately 120 seconds, after which the film surface becomes completely hydrophobic (an indication that the pre-existing surface oxide layer of the film had been fully etched away leaving behind a free surface). In situ FTR, BTR, and TT signals were obtained during surface-side irradiation of both BHF-treated and "as-is" (non-treated) films. Distinct changes in the collected signals between the two cases are identified and discussed later.

4.3 Experimental Results

4.3.1 The Effect of Incident Beam Hot Spots on Melting

We begin by first presenting the experimental results obtained during substrate-side irradiation of the ELA poly-Si films. Again, this irradiation configuration was employed to create a uniform heating profile at the flat Si/SiO_2 interface. BHF solution pre-treatment of the samples was not used in this set of experiments.

Figure 4.2 shows FTR, BTR, and TT signals that were obtained from irradiating the ELA poly-Si film through the bottom SiO_2 substrate at an energy density just below the CMT. The signals here, and subsequent presented signals, are normalized to the CMT and positioned for easy visual comparison. Based upon the transient reflectance and transmission signal considerations discussed in Chapter 3, we identify the initial oscillation (i.e., rise and drop) observed in the FTR and BTR signals, as well as the initial gradual reduction in the TT signal, as arising from simple solid-phase heating, whereas the subsequent variations in the signals are attributed to actual melting and solidification proceeding largely in a 2-D manner. The additional variations in the signals can be precisely and trivially correlated to the measured time-dependent intensity profile of the incident beam (having a primary pulse followed by secondary and tertiary pulses), as shown in Figure 4.3(d). In contrast to the surface-side irradiation experiments of Chapter 3, the BTR signals here show an earlier rise (indicating the onset of melting) than the FTR signals due to the beam being incident

at the film/substrate bottom interface.

Figure 4.3 shows FTR, BTR, and TT signals that were obtained during irradiation of the films through the bottom SiO_2 substrate at various energy densities. At energy densities above the CMT, the appearance of the plateau in the signals indicates that the films have undergone complete melting, prompting the FTR, BTR, and TT signals to saturate where they remain until the nucleation of solids triggers the onset of solidification, and thus causing the FTR and BTR signals to drop, as well as the TT signals to rise. The most critical feature corresponds to the absence of a plateau in the BTR signals even when the films are substrate-side irradiated with relatively high energy densities up to the CMT. This indicates, along with the matching TT profiles, that the bottom interface of the film is not fully melted nearly up to the point in time at which complete melting starts to be substantially manifested. Moreover, melting in these ELA poly-Si films, whereby incident beam hot spots are purposely mitigated via substrate-side irradiation (resulting in a more uniform heating profile at the flat Si/SiO_2 interface), continues to appear 2-D in nature. This is similar to the way melting proceeds in the surface-side irradiated films described in Chapter 3).

Figure 4.4 shows the approximated maximum melt fraction sustained at the surface-side and substrate-side of the ELA poly-Si films irradiated through the bottom SiO_2 substrate at various energy densities. Such data are calculated by normalizing the (maximum) reflectance signal values measured during partial melting of the films to the (maximum) reflectance signal values measured during complete melting of

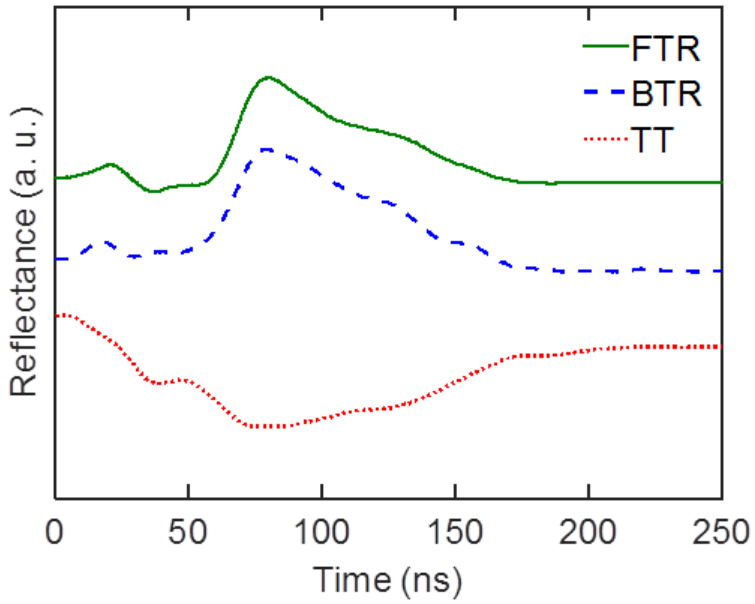

(a)

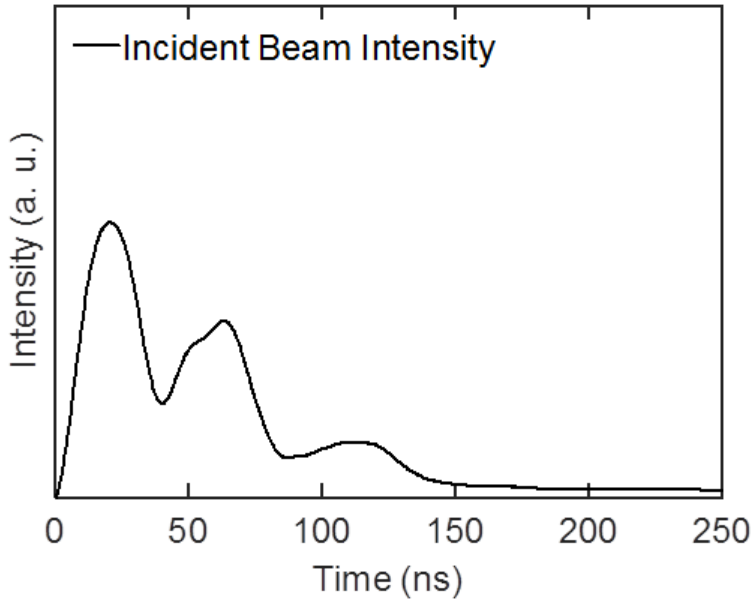

(b)

Figure 4.2: (a) In situ FTR, BTR, and TT signals measured during substrate-side irradiation of the ELA poly-Si film at 0.96 CMT. (b) Experimentally extracted time-dependent intensity profile of the incident beam.

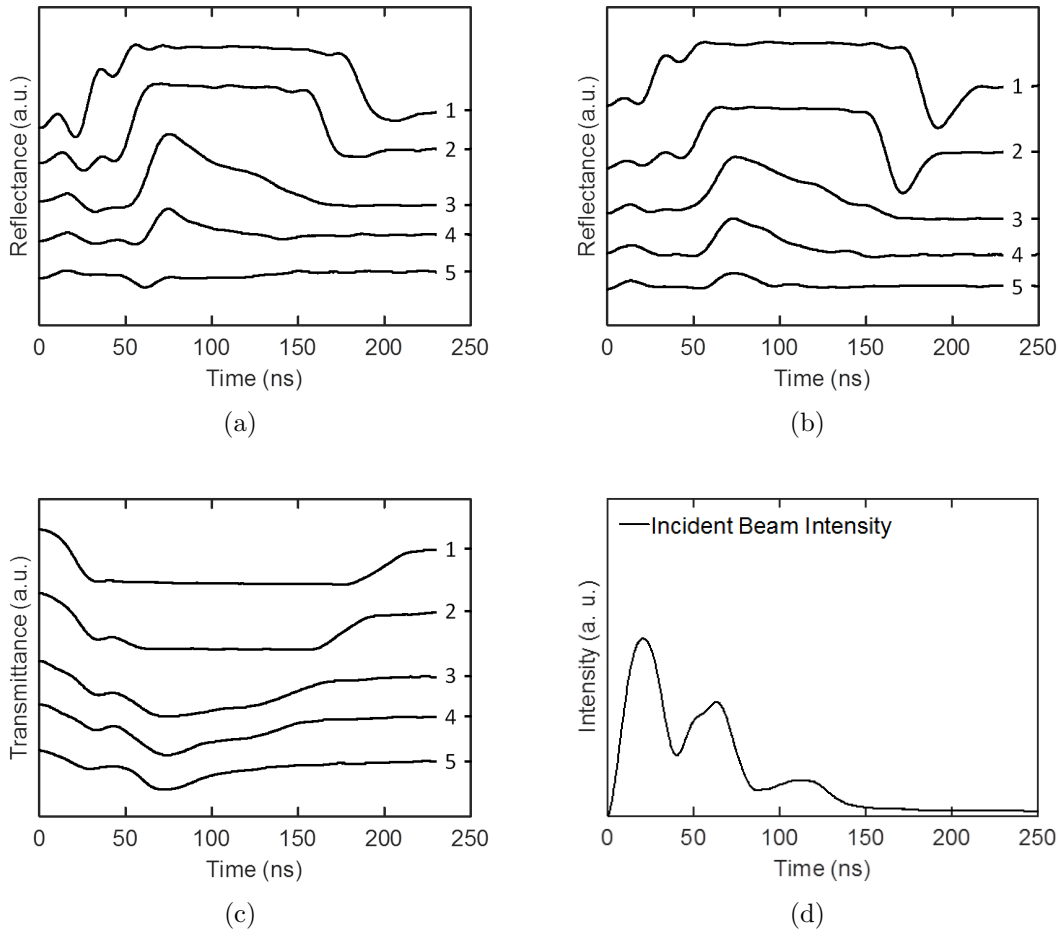

Figure 4.3: In situ (a) FTR, (b) BTR, and (c) TT signals measured during substrate-side irradiation of the ELA poly-Si films at various incident energy densities. The corresponding energy densities (normalized to the CMT) are: (1) 1.30, (2) 1.12, (3) 0.96, (4) 0.85, and (5) 0.77 CMT. (d) A representative profile of the incident beam.

the films, as described in Chapter 3. Due to the beam being incident on the bottom interface of the film, the substrate-side melt fraction is greater than that of the surface-side melt fraction for each individual energy density. The lack of complete melting at the bottom interface (i.e., substrate-side melt fraction ¡ 1.0), even at relatively high energy densities near the CMT, is consistent with the notion that melting in these small-columnar-grained polycrystalline films proceeds in a predominately 2-D manner. The results of these substrate-side irradiation experiments show that a non-uniform heating profile, as affected by incident beam hot spots, is not directly nor intrinsically responsible for the 2-D melting behavior observed in pulsed-laser irradiated ELA poly-Si films.

4.3.2 BHF Treatment

Next, we present experimental results obtained using ELA poly-Si films pre-treated with BHF solution prior to surface-side irradiation. The BHF solution was used to remove any oxide layer present at the surface of the film.

Figure 4.5(a) shows FTR, BTR, and TT signals that were obtained from irradiating the BHF-treated ELA poly-Si film at an energy density just below the CMT. Based on thin-film interference considerations, we attribute the initial oscillation observed in the FTR and BTR signals, and initial gradual reduction in the TT signal, to simple solid-phase heating of the film. Subsequent variations in the signals closely track the measured time-dependent intensity profile of the incident beam and are attributed

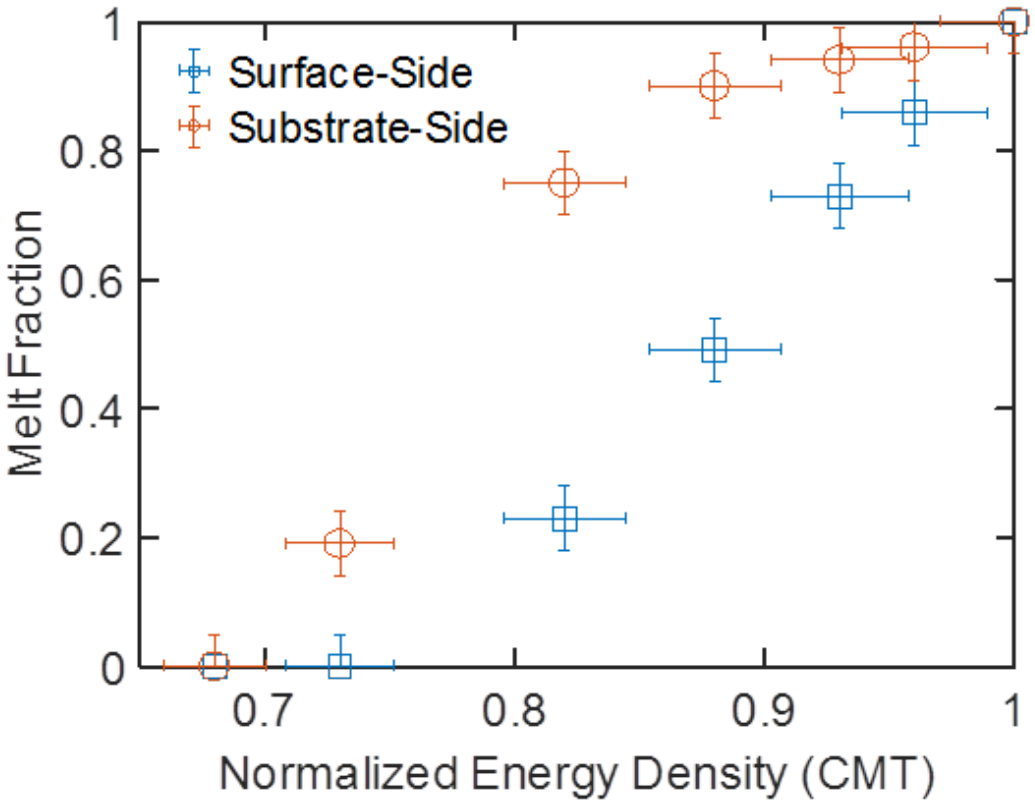

Figure 4.4: Maximum surface-side and substrate-side melt fractions extracted from in situ FTR and BTR signals, respectively. Such signals were measured during substrate-side irradiation of the ELA poly-Si films at various energy densities. A representative profile of the incident beam is shown in Figure 4.3(d).

to actual melting and solidification proceeding in a 2-D manner. The additional variations in the signals can be precisely and trivially correlated to the measured time-dependent intensity profile of the incident beam shown in Figure 4.6(d).

Figure 4.6 shows FTR, BTR, and TT signals that were obtained during irradiation of the BHF-treated films at various energy densities. At energy densities above the CMT, the appearance of the plateau in the signals signifies that the films have undergone complete melting, which subsequently prompts the FTR, BTR, and TT signals

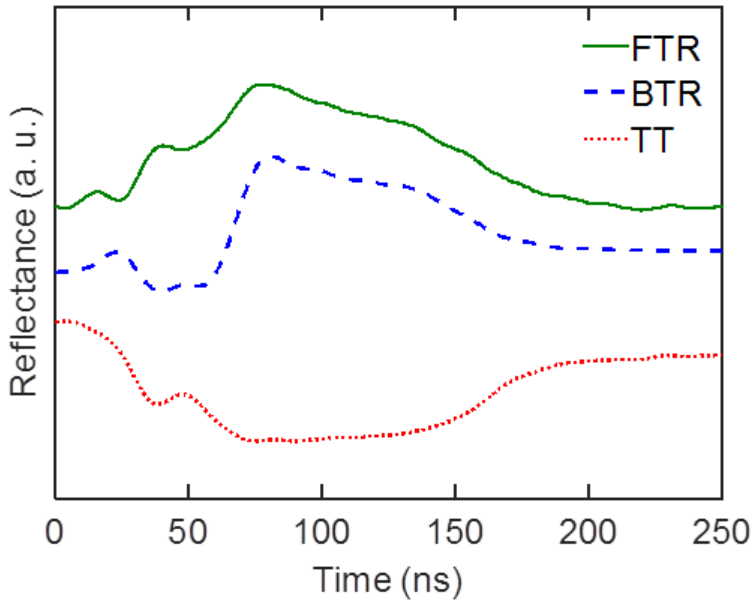

(a)

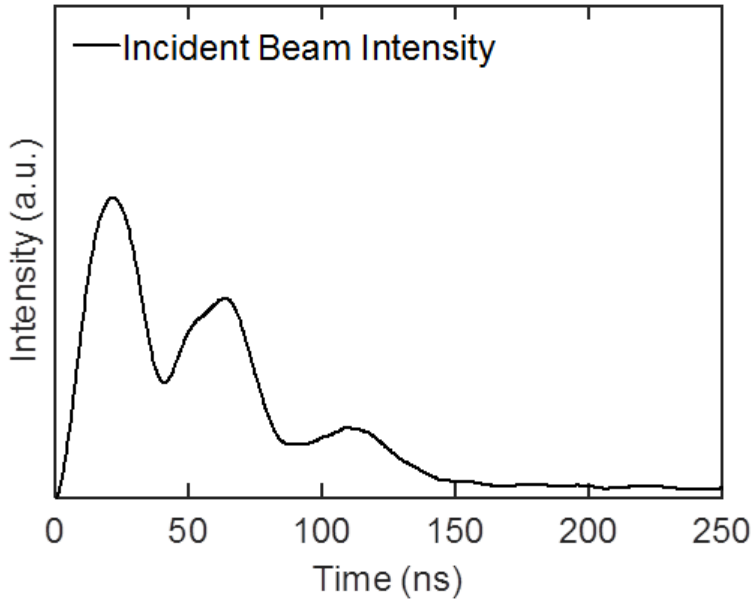

(b)

Figure 4.5: (a) In situ FTR, BTR, and TT signals measured during irradiation of the BHF-treated ELA poly-Si film at 0.97 CMT. (b) Experimentally extracted time-dependent intensity profile of the incident beam.

to saturate where they remain until solidification via the nucleation and growth of solids causes the FTR and BTR signals to drop and the TT signals to rise. The most striking feature corresponds to the absence of a plateau in the FTR signals even when the films (1) contain a melt-prone free surface (via BHF treatment prior to irradiation), and (2) are surface-side irradiated at relatively high energy densities up to the CMT. This indicates, along with the matching TT profiles, that the irradiated surface of the film (devoid of a surface oxide layer) is not fully melted nearly up to the point in time at which complete melting starts to be substantially manifested.

The effect of BHF treatment of the films, and the subsequent creation of a free surface prior to irradiation, is most evident in the FTR and BTR signals obtained at energy densities above the CMT. Figure 4.7 shows FTR and BTR signals that were obtained from irradiating (a) "as-is" (non-treated), and (b) BHF-treated ELA poly-Si films at an energy density above the CMT. Upon complete melting of the films, the FTR and BTR signals quickly rise to saturated values forming plateaus. Figure 4.7(a) shows FTR and BTR saturation occurs almost simultaneously in time for the as-is case. The measured signals reveal that the onset of complete melting at the top and bottom surfaces of the film, which are both similarly in contact with a passivating SiO_2 layer, occurs virtually at the same time. In contrast, Figure 4.7(b) shows FTR saturation occurs distinctly earlier than BTR saturation for the BHF-treated case. This is attributed to the melt-prone nature of the irradiated free surface undergoing complete melting well before any substantial melting takes place at the bottom surface

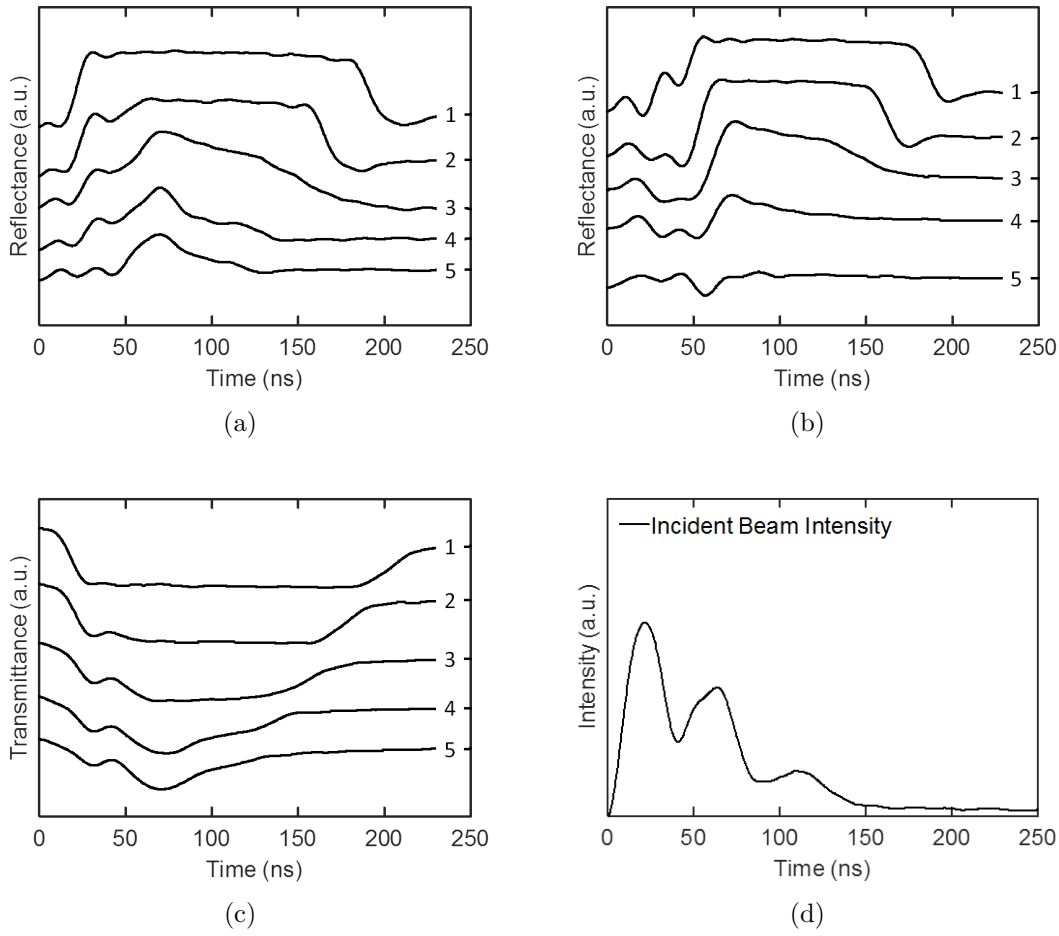

Figure 4.6: In situ (a) FTR, (b) BTR, and (c) TT signals measured during irradiation of the BHF-treated ELA poly-Si films at various incident energy densities. The corresponding energy densities (normalized to the CMT) are: (1) 1.26, (2) 1.10, (3) 0.97, (4) 0.86, and (5) 0.76 CMT. (d) A representative profile of the incident beam.

of the film, which is stabilized by the relatively melt-resistant Si/SiO_2 interface [54].

Figure 4.8 shows the approximated maximum melt fraction sustained at the surface-side and substrate-side of the BHF-treated ELA poly-Si films irradiated at various energy densities. Such data are calculated from the measured FTR and BTR signals, as discussed in Chapter 3. First, we observe the surface-side melt fraction is greater than the substrate-side melt fraction for all energy densities above the PMT and below the CMT. This is consistent with the incident beam irradiating and initially heating the top surface of the film. Second, despite the presence of a melt-prone free surface (via BHF treatment of the film prior to irradiation), we do not observe complete melting at the irradiated film surface (i.e., surface-side melt fraction < 1.0) even at relatively high incident energy densities near the CMT. This deviation from the somewhat expected 1-D melting behavior (where prompt and complete surface melting takes place) is attributed to (1) the heterogeneous nature of the film surface containing grain boundary and grain junction regions, and (2) incident beam hot spots resulting in a periodic surface heating profile. Both the presence of grain boundaries and hot spots at the surface of the film can assist melting to proceed in a more 2-D manner.

Figure 4.9 plots the difference between the maximum surface-side and substrate-side melt fractions, ΔMelt Fraction, for both BHF-treated and as-is films at various energy densities. Recall, that in the limit of perfect 1-D and 2-D (partial) melting, ΔMelt Fraction is equal to 1.0 and 0.0, respectively. As such, the larger ΔMelt

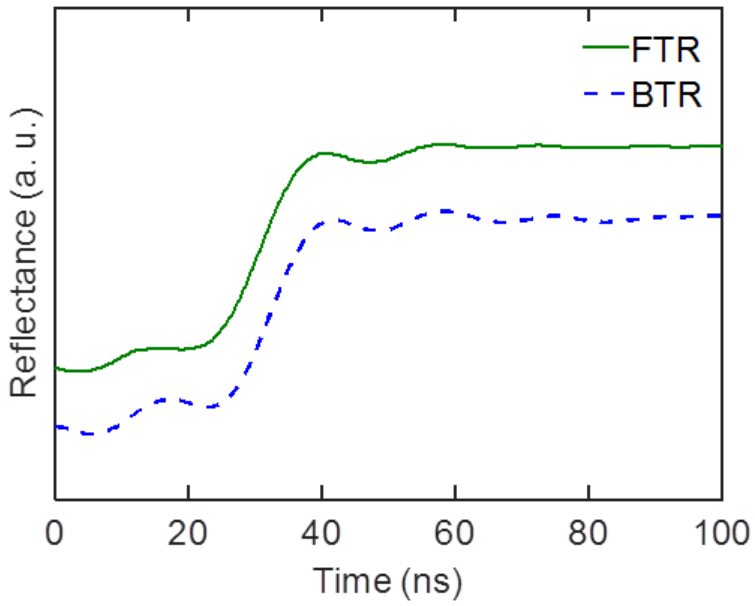

(a)

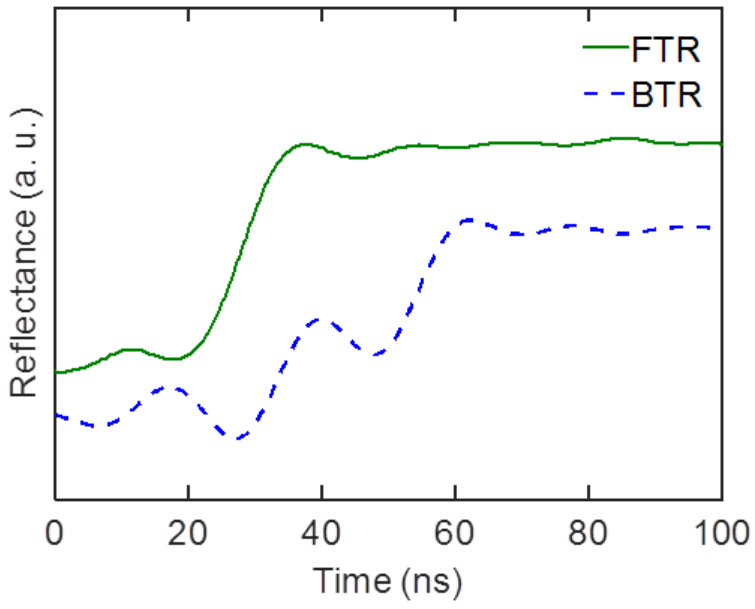

(b)

Figure 4.7: In situ FTR and BTR signals measured during irradiation of the (a) "as-is" (non-treated), and (b) BHF-treated ELA poly-Si films at similar normalized energy densities well above the CMT (1.32 and 1.26 CMT, respectively). A representative profile of the incident beam is shown in Figure 4.6(d)

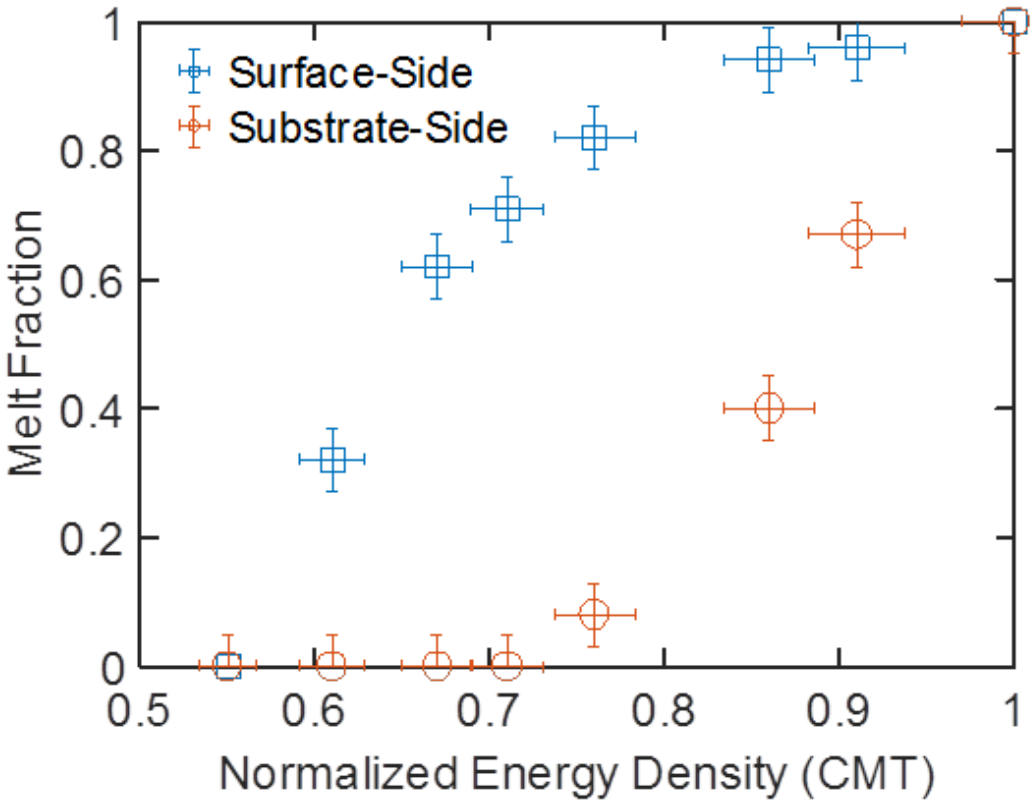

Figure 4.8: Maximum surface-side and substrate-side melt fractions extracted from in situ FTR and BTR signals, respectively. Such signals were measured during irradiation of the BHF-treated ELA poly-Si films at various energy densities. A representative profile of the incident beam is shown in Figure 4.6(d).

Fraction values corresponding to the BHF-treated films is consistent with the notion that melting in these films, while 2-D in nature overall, is measurably more 1-D than in as-is films.

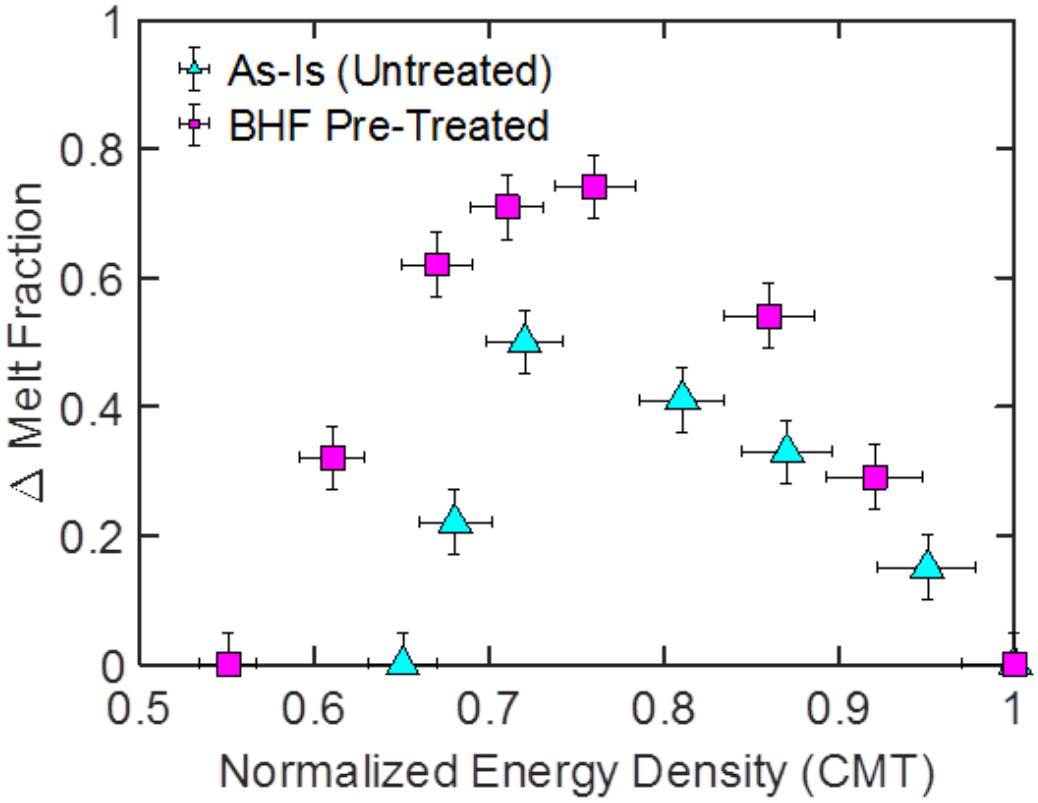

Figure 4.9: Difference in maximum surface-side and substrate-side melt fractions, ΔMelt Fraction, calculated from in situ FTR and BTR signals, respectively. Such signals were measured during irradiation of the BHF-treated and as-is ELA poly-Si films at various energy densities

4.4 Discussion

4.4.1 2-D Melting Under Uniform Irradiation

We concluded in the previous chapter that melting proceeds in a predominately 2-D manner in pulsed-laser irradiated ELA poly-Si films. However, those films were irradiated at the top surface of the film containing surface protrusions, which scatter light to create incident beam hot spots. As these hot spots will affect the local heating

profile of the films and, as a result, can "extrinsically" assist the films to melt in a more 2-D manner, we became interested in examining the melting transition of the films under uniform irradiation conditions to investigate the "intrinsic" situation in which such hot spots do not participate in the melting process.

The creation of incident beam hot spots is commonly observed in a wide range of materials under laser irradiation [74]. A theory based on laser-induced periodic surface structures (LIPSS) has long been developed, which explains the creation of hot spots as arising from coupling between the incident irradiation and pre-existing surface roughness [73]. The periodicity of the generated hot spots is determined primarily by the wavelength and angle of incidence of the incoming beam with respect to the irradiated surface. The resulting periodic heating and temperature profile can trigger inhomogeneous melting and solidification, and in the case of pulsed-laser irradiated silicon films, the difference in volumetric density between liquid silicon and solid silicon causes the formation of surface protrusions at the last places to solidify. Such protrusions increase the roughness of the film surface and further enhance the scattering of light (and thus, generation of hot spots) upon additional irradiations of the film.

The surface protrusions observed in ELA-processed silicon films are understood to result from this LIPSS phenomenon and occur at grain boundary and grain junction regions [4]. They possess a characteristic periodicity of 308 nm, which is primarily determined by the wavelength of the XeCl excimer laser used to process the initially a-

Si films (see the surface morphology images obtained via AFM in Chapter 3). While the location and intensity of the incident beam hot spots at the film surface have not yet been established, the experiments presented here, nonetheless, show that a periodic irradiation profile (which may lead to increased heating at film protrusions coincident with grain boundaries and grain junctions, or, oppositely, increased heating at thinner regions of the film corresponding to grain centers) is not required for pulsed-laser-induced 2-D melting in ELA poly-Si films.

The mitigation of incident beam hot spots was achieved by irradiating the films through the bottom SiO_2 substrate to deposit the majority of the beam energy at the bottom Si/SiO_2 interface. Light scattering effects, as described by LIPSS, is essentially eliminated due to the bottom interface lacking any appreciable morphological character [72]. The results of these uniform irradiation experiments, devoid of hot spots, show that melting in these irradiated films continues to proceed in a predominately 2-D manner. That is, the presence of hot spots, which can extrinsically assist the films to melt in a more 2-D fashion, is not fundamentally responsible, nor required, for 2-D melting to occur in these small-columnar-grained polycrystalline films. Instead, we affirm it is the presence of columnar grain boundaries, and subsequently argue for a grain-boundary-initiated melting model, which determines the manner in which melting proceeds. This result is meaningful for identifying the possible causes that could affect the dimensionality of melting and is especially critical regarding those models which invoke a hot-spot-induced periodic heating profile to account for

the lateral melting and subsequent microstructure evolution in silicon films during ELA processing [71].

4.4.2 Melting Under Various Surface Conditions

Next, we discuss the experimental results comparing the melting behavior in ELA poly-Si films with and without BHF treatment prior to irradiation. Such experiments were conducted to examine the significance of a passivating SiO_2 layer on the melting transition.

The results obtained from irradiating "as-is" films (or films without BHF treatment prior to irradiation and, thus, containing a passivating SiO_2 layer at the top film surface) show that melting proceeds in a predominately 2-D manner. As was briefly discussed in Chapter 3, this 2-D melting character of the films arises intrinsically as a result of the propensity of the grain boundaries to melt more readily than silicon at the Si/SiO_2 interface (at least presumably for high-angle non-special grain boundaries). The model used to describe this melting transition consists of melting first initiating via local and prompt complete melting of the grain boundary and grain junction regions upon irradiation. As the incident beam continues to heat the film, the liquid regions grow as their melting fronts propagate laterally inwards towards the center of the unmelted grains. During this time, these grain centers, which are contacted on both the top surface and bottom surface with SiO_2, continue to rise in temperature during solid-phase heating and experience a large degree of transient

superheating without melting (as evidenced by the lack of a plateau in the transient reflectance and transmission signals during partial melting of the films).

We presently consider that this superheating scenario is entirely possible specifically for the case in which the surface of the ELA poly-Si film is passivated with a SiO_2 layer (e.g., native oxide layer), which provides a melt-resistant Si/SiO_2 interface. On the one hand, we have previously demonstrated that substantial superheating of silicon can be transiently achieved at the Si/SiO_2 interface [54], and, on the other hand, we observe that the melting behavior of an otherwise identical ELA poly-Si film becomes definitively less 2-D in character when the film is treated with BHF solution prior to being irradiated (note, however, that some degree of deviation from the perfect 1-D melting scenario is expected as a result of (1) hot spot creation due to beam scattering at the surface protrusions, and (2) the non-uniform heterogeneous nature of the polycrystalline film surface as it contains grain boundaries and grain junctions). These experimental results both substantiate that transient superheating of the grain interior can take place during partial melting of the "as-is" ELA poly-Si films. Physically and thermodynamically, this indicates that the Si/SiO_2 interface is relatively stable and that the magnitude of interfacial energies between the oxide and silicon free surface must be relatively small (compared to either the free surface energies or high-angle grain boundary energies). Available data regarding the values of these quantities is found to be consistent with the above statement derived from our experimental results [82][83][84].

In fact, as the above statement reveals, in addition to establishing the foundation for eventual mastering and subsequent optimization of the ELA process, the present findings reported thus far in this thesis can also be identified as contributing scientifically in providing much sought after experimental results in the longstanding fundamental topic of preferential melting at grain boundaries and other high-excess-free-energy sites including free surfaces and Si/SiO_2 interfaces. Furthermore, the present work builds on, and is consistent with, a recently performed investigation involving the melting of a single-crystal silicon film on SiO_2 [55], which has revealed (1) the melt-resistant nature of the Si/SiO_2 interface (i.e., the interface is capable of kinetically withstanding a substantial degree of superheating), and (2) the melt-prone nature of the silicon free surface, which was found to melt readily and presumably at or near the equilibrium temperature.

Lastly, we conclude by appreciating the critical role of the film surface conditions during ELA processing, as we can clearly recognize now that the melt-resistant passivating SiO_2 layer reduces the degree to which surface melting takes place, thereby enhancing the overall 2-D nature of melting in these thin and small-columnar-grained poly-Si films. This is important since we have previously identified 2-D melting as the process-enabling element of the ELA process, which permits microstructure evolution of the grains to take place in an effective manner.

4.5 Summary

In this chapter, we examined the significance of two essential components of the ELA process and their effects on melting: (1) incident beam hot spots, and (2) passivating SiO_2 surface layers.

We first presented transient reflectance and transmission-based experimental results, which explicitly demonstrated that ELA poly-Si films irradiated through the bottom SiO_2 substrate melt in a predominately 2-D manner, despite the purposeful mitigation of incident beam hot spot generation. These findings lead us to conclude that such hot spots (formed via beam scattering at surface protrusions, and which result in a periodic energy deposition and heating profile) are not solely nor intrinsically responsible for the 2-D nature of melting and solidification observed in ELA-processed silicon films. Instead, we affirm it is the microstructure of these polycrystalline films, comprised of small and columnar grains, that constitute the fundamental mechanism behind the observed 2-D melting behavior, whereby grain boundary melting is followed by 2-D lateral growth of the liquid into the transiently superheated interior of unmelted grains.

In the latter half of this chapter, we address the impact of a passivating SiO_2 surface layer on the pulsed-laser-induced melting transition in ELA poly-Si films. We show via transient reflectance and transmission analysis that the irradiated surface of the films melts more readily when the SiO_2 layer at the film surface is removed via BHF solution prior to irradiation. Nevertheless, we observe that these BHF-treated

films, which contain a melt-prone free surface, continue to melt in a surprisingly and largely 2-D manner (though less 2-D in extent than the melting behavior observed in similarly irradiated "as-is" films (untreated) that are still passivated with a SiO_2 layer at the film surface) as evidenced by the lack of a plateau in the FTR, BTR, and TT signals even at energy densities up to the CMT. Some degree of deviation away from 1-D melting can be expected in the films (which are surface-side irradiated) as a result of (1) the formation of incident beam hot spots (via beam scattering at surface protrusions), and (2) the non-uniform heterogeneous nature of the polycrystalline film surface as it contains grain boundary and grain junction regions. The conclusions made here help us to recognize and appreciate the significant role of a passivating SiO_2 layer at the surface of the films during ELA processing. Clearly, melting becomes more 2-D in nature when the silicon at the surface of the film is in contact with a SiO_2 layer, which, as we will discuss in greater detail later in this thesis, assists the microstructure evolution obtained in ELA.

Chapter 5

A 2-D Grain Boundary Melting Model

5.1 Introduction

Thus far, we have experimentally investigated the pulsed-laser-induced melting transition in ELA poly-Si films under various configurations. Our findings reveal that while several process-related details (e.g., pulse duration, incident beam hot spots, and surface passivation) can affect the dimensionality of melting, the films in any case melt in a remarkably and largely 2-D manner.

In this chapter, we suggest a model used to describe this 2-D melting (and solidification) behavior, which consists of grain-boundary-initiated melting, followed by lateral melting into the transiently superheated interior of the columnar grains. We

also devise a melting dimensionality diagram that can graphically map out the 1-D-dominated and 2-D-dominated melting regimes in the melt fraction parameter space. Finally, we discuss the implications of our melting model, whereby grain boundary melting remains a principal tenet of the model, in regard to those models previously proposed to describe the ELA process.

5.2 Melting at Grain Boundary and Grain Junction Regions

Over the years, several experimental, theoretical, and computational investigations have demonstrated the propensity for the melting transition in a variety of materials to begin at grain boundaries [43][45][23]. It is not difficult to account for the aggressive participation of grain boundary and grain junction regions in initiating the melting transition, as they represent high-excess-free-energy sites where liquid can preferentially and heterogeneously form with very little thermodynamic resistance. Such findings appear to be consistent in across various material systems and under different heating regimes, including laser-irradiated silicon films [17][58].

The melting experiments presented in this thesis were performed on polycrystalline films consisting primarily of high-angle grain boundaries. These films were generated via ELA processing (of initially 50-nm-thick a-Si films) using a state-of-the-art ELA system and method, which resulted in the formation of periodic 300-nm columnar

grains having surface protrusions located at the grain boundaries. The surface of the films was passivated with a SiO_2 layer at the top, while the film bottom was in contact with a SiO_2 substrate below. Images (captured via AFM and TEM) of the microstructure of the ELA poly-Si films can be found in Chapter 3.

Under pulsed-laser irradiation, melting in these films occurs in a predominately 2-D manner and is initiated by melting at the grain boundaries. We attribute the 2-D melting character of the films as arising largely and intrinsically as a result of the propensity of the grain boundaries to melt more readily than the silicon at the oxide interface (as evidenced by a lack of plateau in the FTR, BTR, and TT signals, which indicates that the SiO_2-passivated film surface does not fully melt even at energy densities up to the CMT). This finding is consistent with our previous microstructure-analysis-based suggestion that the microstructure evolution realized in ELA must involve at least local complete melting at grain boundaries [17]. As we will discuss in greater detail later, it is this localized complete melting at the columnar grain boundaries (resulting in the formation of liquid throughout the thickness of the films), and the subsequent extent of localized melting of silicon at the bottom Si film/SiO_2 interface, that primarily determines the extent of grain boundary displacement during ELA processing.

Previous studies have attributed the melt-initiated behavior of grain boundaries to non-uniform heating of the films during ELA processing. Recall, incident beam hot spots are generated at the irradiated surface upon beam scattering at non-planar sur-

face features (i.e., surface protrusions). If one assumes the location of these hot spots coincide with grain boundary regions, it is reasonable to attribute the melt-prone nature of grain boundaries in pulsed-laser irradiated poly-Si films to simple and localized heating. However, as we have demonstrated in Chapter 4 via the substrate-side irradiation of ELA poly-Si films, which results in uniform heating of the bottom film surface, the irradiated films continue to melt in a 2-D manner despite the mitigation of incident beam hot spots. We conclude from these experiments that (1) hot spots are not intrinsically responsible for 2-D melting (although, if present, they can assist melting to become more 2-D in nature, and (2) it is actually the presence of melt-prone grain boundaries, and subsequent grain-boundary-initiated melting, that constitutes the intrinsic mechanism responsible for the observed 2-D melting behavior.

Figure 5.1 schematically illustrates the 2-D nature of melting in a surface-side irradiated poly-Si film composed of columnar grains. Melting initiates at the grain boundary region nearest the irradiated surface, followed by prompt and complete melting of the grain boundary. Liquid is formed throughout the thickness of the film to create relatively columnar solid/liquid melting interfaces. As the film continues to heat, the melting fronts propagate laterally into the unmelted grain regions.

5.3 Superheating at the Interior of Grains

Another subtle, yet critical, element of our proposed model corresponds to the superheating of the interior of a grain during grain-boundary-initiated melting and

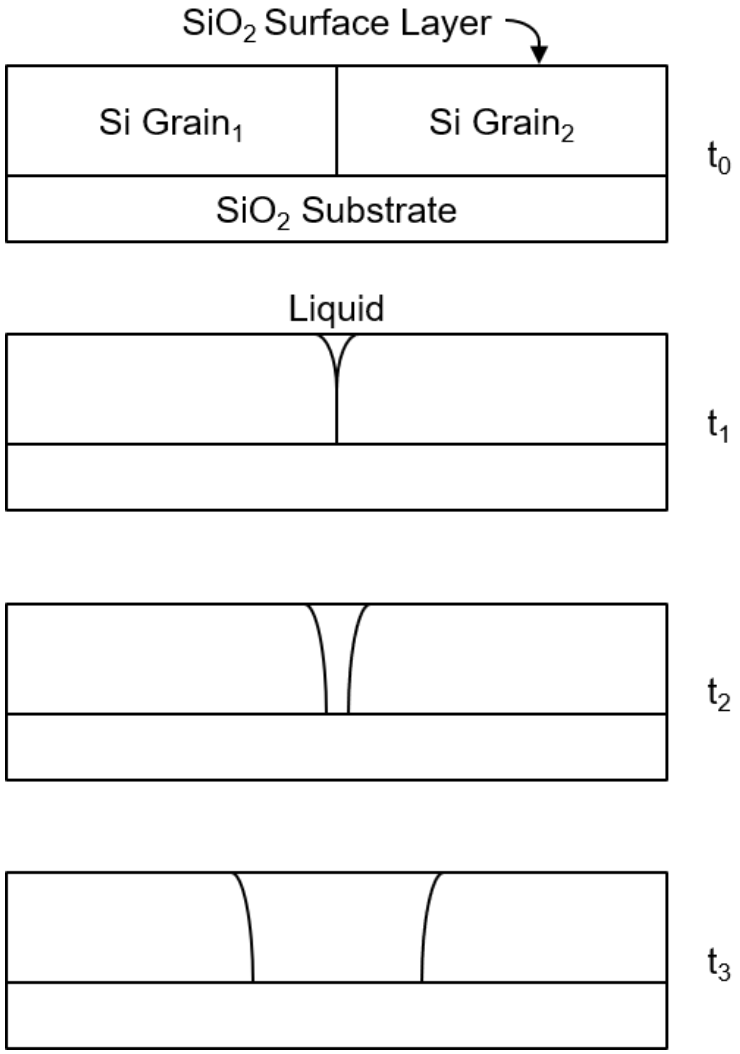

Figure 5.1: Cross-sectional schematic diagrams illustrating the time evolution of grain-boundary-initiated melting and subsequent lateral melting of a surface-side irradiated poly-Si film consisting of columnar grains. The film surface is passivated with a thin SiO_2 layer. Surface protrusions are ignored for the sake of simplicity.

subsequent 2-D lateral melting towards the grain center. The expected temperature profile of the ELA poly-Si film dictates that a substantial degree of transient superheating must take place within the unmelted portions of the grains, especially at the top and center regions (away from the heat-consuming melting interface) of the film, during pulsed-laser-induced melting. The appearance of superheating at the grain centers can be explained as resulting for the following reasons.

First, the beam is incident on the grains, and continuously heating the unmelted portions of the grains, even during the (partial) melting phase of the irradiation process. Next, the initiation of melting at the grain boundaries and grain junctions begins at least near, and possibly slightly above, the equilibrium point. And finally, the rapid lateral movement of the melting interface towards the grain center (even as interfacial decalescence transpires at the endothermic melt front) reflects that a non-negligible degree of superheating must be happening.

This scenario in which the unmelted grain center undergoes transient superheating is entirely possible specifically for the case in which the surface of the ELA poly-Si film is passivated with a SiO_2 layer. We have recently induced and demonstrated that substantial superheating of silicon can be transiently achieved at the Si/SiO_2 interface [54]. Additionally, the transient reflectance and transmission-based results of Chapter 4 showed that the melting behavior of an otherwise identical ELA poly-Si film becomes definitively more 1-D when the film is pre-treated with BHF solution used to remove the surface oxide layer prior to irradiation. (Some degree of deviation

from the perfect 1-D melting scenario in such films containing a free surface is expected because of (1) hot spot creation due to light scattering at the surface protrusions, and (2) the non-uniform heterogeneous nature of the poly-Si film surface as it contains grain boundaries and grain junctions). Such results underscore the presence of a passivating SiO_2 layer, which assists the ELA poly-Si films to melt in a more 2-D manner, as it enables melting to preferentially initiate at grain boundaries rather than at the melt-resistant silicon stabilized at the oxide interface.

In the next chapter, we will use a custom numerical simulation package (developed within our group) to examine the extent of superheating in polycrystalline films that melt in a 2-D manner under pulsed-laser irradiation. The findings of those simulations substantiate the melting model described here, as well as provide more quantitative information regarding the physical values essential to our 2-D melting model (e.g., degree of superheating, melting interface velocity, total melt fraction).

5.4 Dimensionality of Melting

We have qualitatively described the melting behavior observed in irradiated ELA poly-Si films as being a mostly 2-D process involving grain-boundary-initiated melting, followed by lateral melting into the transiently superheated center of the grains. However, it can be fruitful to obtain a more quantitative description of the dimensionality of melting. We can define such a parameter by first considering the perfect 1-D and 2-D melting scenarios as the boundary conditions to melting dimensionality.

The perfect 1-D melting scenario is described as the case in which the surface of the film undergoes prompt and localized complete melting, followed by vertical propagation of the solid/liquid melting interface towards the unmelted bottom of the film, as is schematically illustrated in Figure 5.2. The local melt fractions measured at the top and bottom surfaces of the film during (partial) 1-D melting is 1.0 and 0.0, respectively.

On the other hand, Figure 5.3 illustrates the perfect 2-D melting scenario where liquid is initially formed throughout the thickness of the film, followed by the solid/liquid melting interfaces moving laterally outwards towards the unmelted regions of the film. In the case of (partial) 2-D melting, the local melt fractions measured at the top and bottom surfaces of the film are equal. For both the perfect 1-D and 2-D melting scenarios, we assume that the solid/liquid melting interfaces are linear.

Having clarified the perfect 1-D and 2-D melting scenarios, we can take the next step by defining an "intermediate" melting scenario (between 1-D and 2-D melting), which we refer to as 1.5-D melting. For the case of a polycrystalline film consisting of uniform columnar grains, and assuming that melting in the film (1) initiates at the grain boundary regions nearest the irradiated surface of the film, and then (2) grows along both the film surface and grain boundary surface without liquid nucleation triggering at the superheated grain center, we define 1.5-D melting as the scenario in which the extent of melting measured along the film surface (or bottom surface of the film) is equal to the extent of melting measured along the grain boundary (or

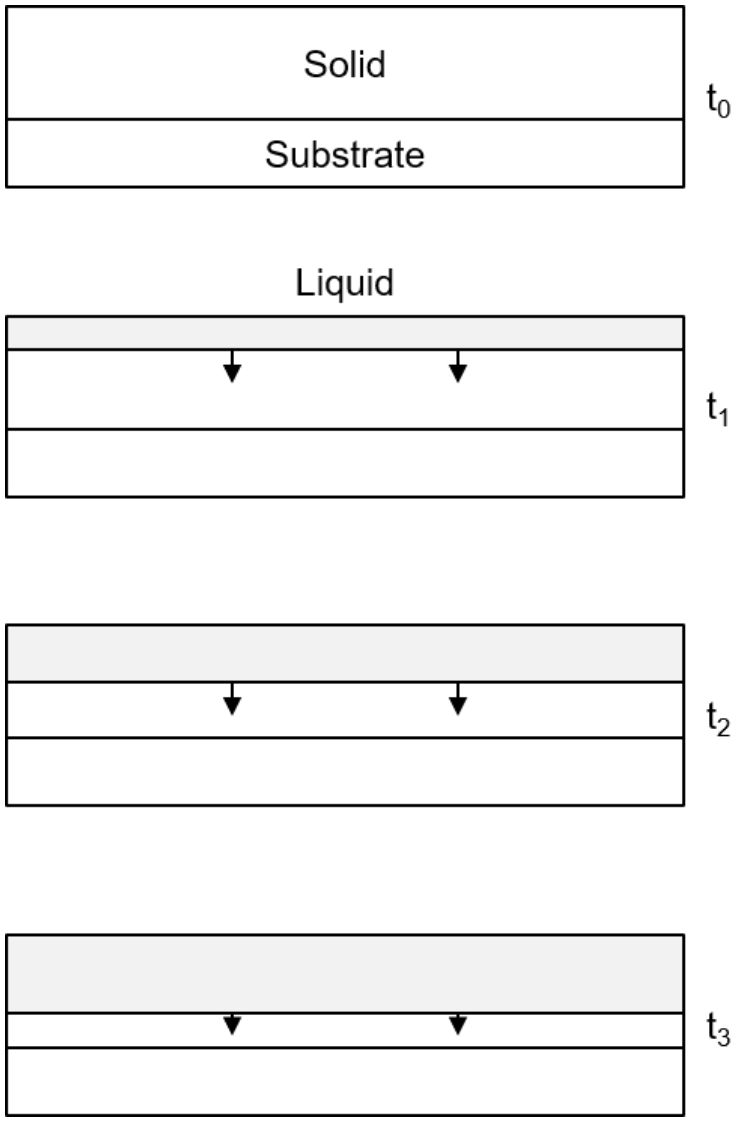

Figure 5.2: Cross-sectional schematic diagrams illustrating the time evolution of the perfect 1-D melting scenario in a film. In 1-D melting, the film surface undergoes local complete melting, followed by downward propagation of the melting front towards the unmelted bottom of the film (denoted by the small black arrows).

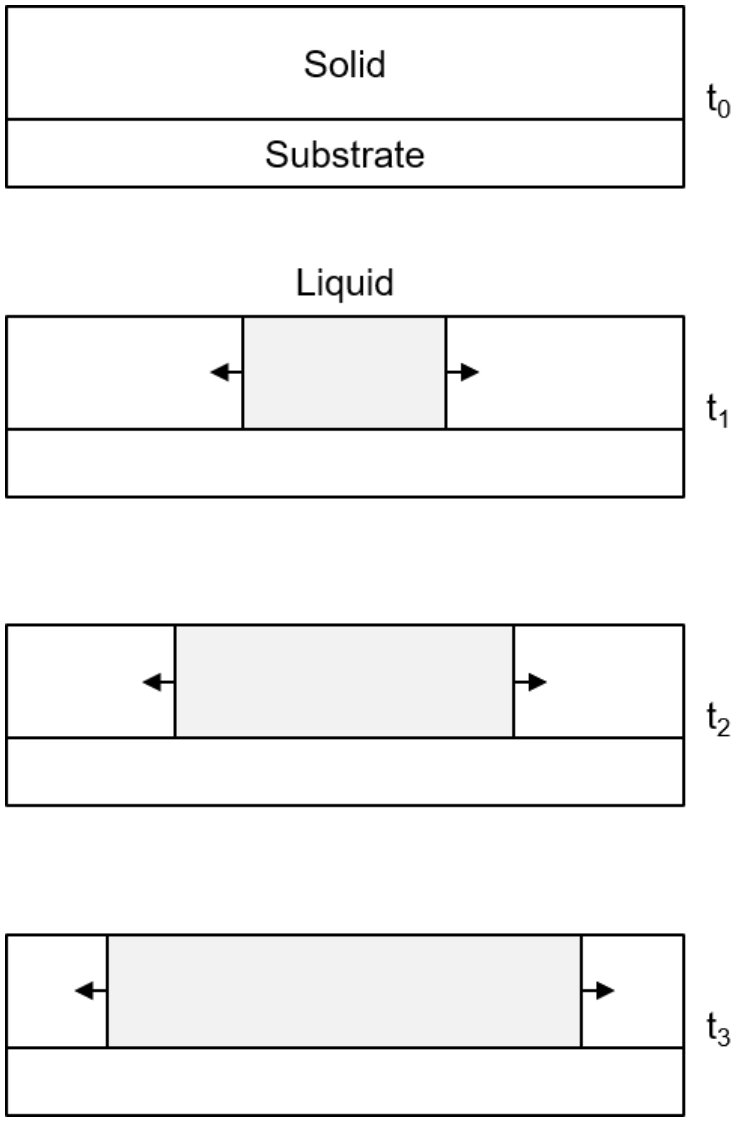

Figure 5.3: Cross-sectional schematic diagrams illustrating the time evolution of the perfect 2-D melting scenario in a film. In 2-D melting, liquid is formed throughout the thickness of the film, followed by lateral propagation of the solid/liquid melting interfaces towards the unmelted regions of the film (denoted by the small black arrows).

center of the grain). By this definition, the absolute slope (relative to the film surface normal) of the linear solid/liquid melting interface is constant and given by S:

$$S = \frac{A}{2B} \tag{5.1}$$

where A is the thickness of the grain, and B is the grain size. Figure 5.4 illustrates the time evolution of the perfect 1.5-D melting scenario in a polycrystalline film.

At this point, we can begin to establish a method that will allow us to graphically assess the melting behavior observed in pulsed-laser irradiated films. Figure 5.5 plots the melt fraction measured at the bottom surface of the film versus the total melt fraction of the film for the special cases of 1-D, 1.5-D, and 2-D melting. The curves associated with perfect 1-D, 1.5-D, and 2-D (partial) melting form a melting dimensionality diagram that maps out the 1-D-dominated and 2-D-dominated domains in the melt fraction parameter space. By projecting the experimentally measured melt fraction values obtained in irradiated ELA poly-Si films, the dimensionality of melting, and the impact of various factors that may affect the dimensionality, can be evaluated. The local melt fraction at the film surface (top or bottom) can be extracted from the transient reflectance signals measured in situ during irradiation of the films, while, the total melt fraction of the film, on the other hand, can be linearly approximated using the measured incident beam energy density (where the total melt fraction of the film is equal to 0 at the PMT, and equal to 1 at the CMT).

Figure 5.6 plots the maximum bottom and total melt fractions obtained during

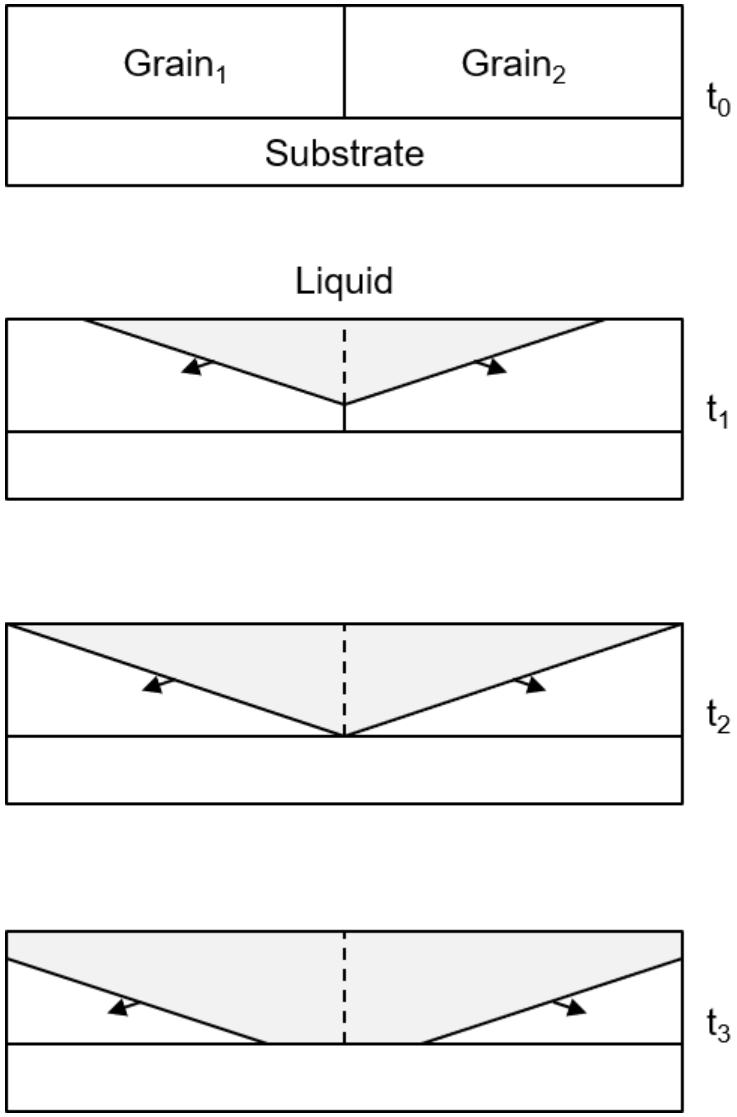

Figure 5.4: Cross-sectional schematic diagrams illustrating the time evolution of the perfect 1.5-D melting scenario in a polycrystalline film consisting of uniform columnar grains. The diagrams are centered around a representative grain boundary showing each half of its neighboring grains. The extent of melting measured along the film surface (or bottom surface of the film) is equal to the extent of melting measured along the grain boundary (or center of the grain).

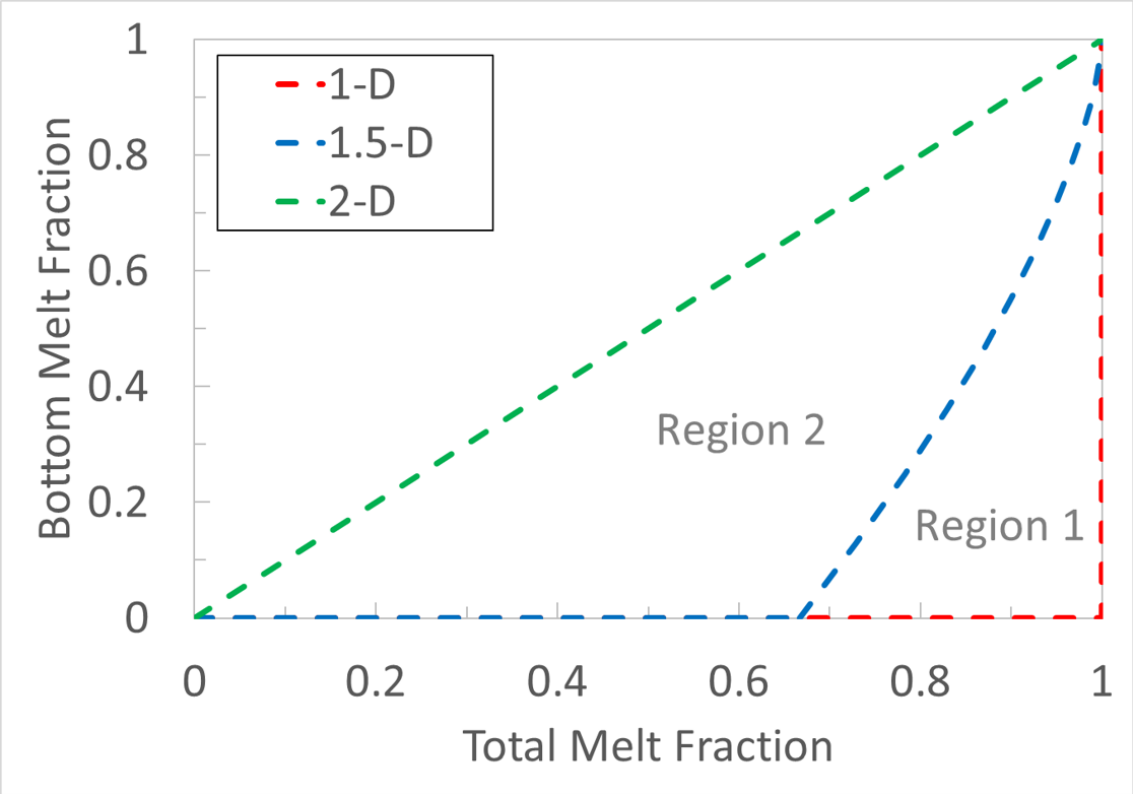

Figure 5.5: Bottom melt fraction versus total melt fraction of the film undergoing perfect 1-D (red curve), 1.5-D (blue curve), and 2-D (green curve) melting. Melting transitions plotted in region 1 (contained by the red and blue curves) are considered 1-D dominated, whereas melting transitions plotted in region 2 (contained by the blue and green curves) are considered 2-D dominated.

surface-side irradiation of the SiO_2-passivated ELA poly-Si films at various energy densities. The films were irradiated using a 30-ns and 240-ns at FWHM beam profile, as shown in Fig 5.7. The most striking feature corresponds to the fact that all the projected melt fraction values lay within the 2-D dominated region (i.e., in between the limits of perfect 1.5-D and 2-D melting), which is consistent with our repeated description of the pulsed-laser-induced melting transition in ELA poly-Si films as being a predominately 2-D process. However, the films irradiated with the 30-ns

beam (versus the 240-ns beam) exhibit a larger deviation away from the perfect 2-D melting limit. This is attributed to a greater extent of melting taking place at the film surface, which undergoes more rapid heating, when the film is irradiated with a shorter pulse duration incident beam.

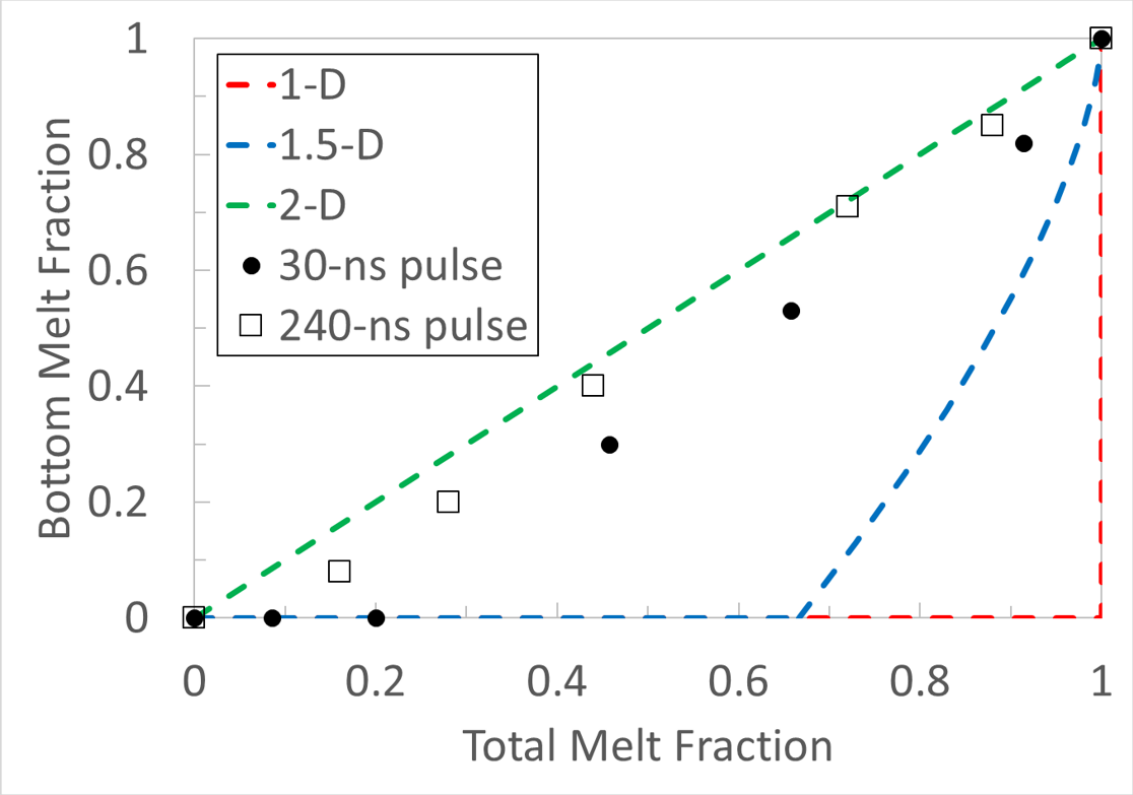

Figure 5.6: Maximum bottom melt fractions versus maximum total melt fractions obtained during surface-side irradiation of the SiO_2-passivated ELA poly-Si films. The films were irradiated using a 30-ns (closed circles) and 240-ns (open squares) at FWHM beam profile at various energy densities. The 1-D (dashed red curve), 1.5-D (dashed blue curve), and 2-D (dashed green curve) melting limits are plotted as well.

We can also investigate the role of incident beam hot spots (generated at the film surface during surface-side irradiation or avoided at the bottom film surface/substrate interface during substrate-side irradiation) in affecting the dimensionality of melting.

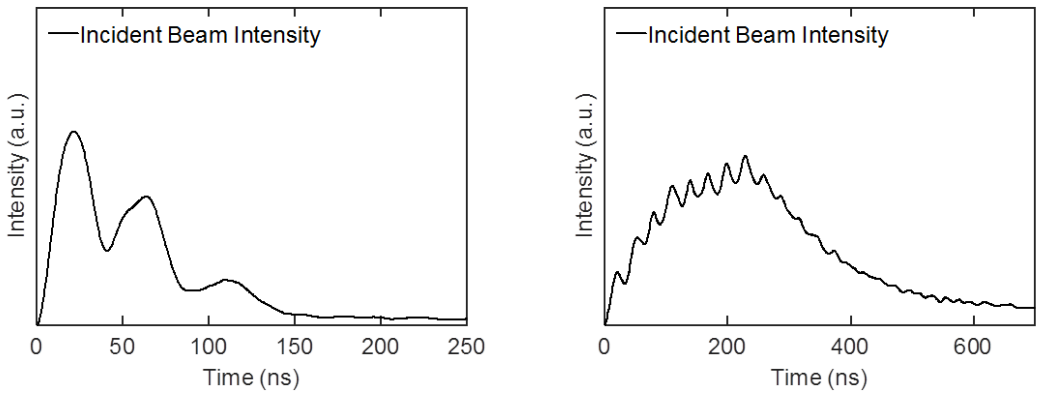

Figure 5.7: A representative profile of the incident beam with a (a) 30-ns at FWHM, or (b) 240-ns at FWHM pulse duration.

Figure 5.8 plots the maximum bottom (or top) and total melt fractions obtained during surface-side (or substrate-side) irradiation of the SiO_2-passivated ELA poly-Si films at various energy densities. In both irradiation configurations, a 30-ns at FWHM beam profile was used to heat the films, as shown in Fig 5.7(a). The melt fraction values obtained from both the surface-side and substrate-side irradiated films are projected on a near-identical trajectory in the 2-D dominated regime of melting. Such results suggest that the formation (or preclusion) of LIPSS-induced hot spots during surface-side (or substrate-side) irradiation plays a minor role in changing the overall 2-D melting behavior observed in the ELA poly-Si films.

Lastly, we examine the effect of SiO_2 passivation on melting dimensionality in ELA poly-Si films pre-treated with BHF solution (used to remove the surface oxide layer) prior to irradiation. Figure 5.9 plots the maximum bottom and total melt fractions obtained during surface-side irradiation of the "as-is" (non-treated) and BHF-treated

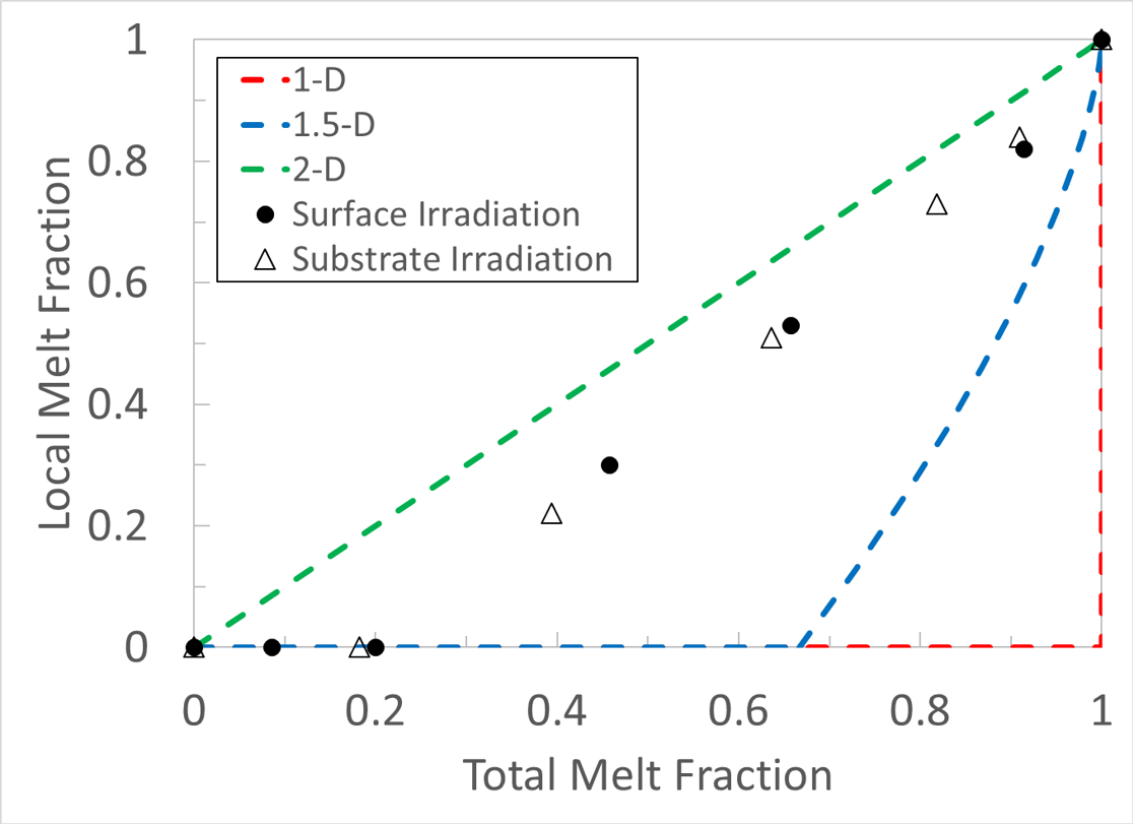

Figure 5.8: Maximum bottom (or top) melt fractions versus maximum total melt fractions obtained during surface-side (or substrate-side) irradiation of the SiO_2-passivated ELA poly-Si films. The films were surface-side (closed circles) or substrate-side (open triangles) irradiated using a 30-ns at FWHM beam profile at various energy densities. The 1-D (dashed red curve), 1.5-D (dashed blue curve), and 2-D (dashed green curve) melting limits are plotted as well.

ELA poly-Si films at various energy densities. The films were irradiated using a 30-ns at FWHM beam profile, as shown in Fig 5.7(a). While all the projected melt fraction values are plotted within the 2-D dominated regime, the removal of the surface oxide layer (and subsequent creation of a melt-prone free surface) results in a loss of 2-D melting character in the irradiated films. This is indicated by the melt fraction values of the BHF-treated films laying closer to the 1.5-D melting limit than those of the

as-is films with a SiO_2-passivated surface. Some degree of deviation from the perfect 1-D melting scenario in such films containing a free surface is expected as a result of (1) hot spot creation due to light scattering at the surface protrusions, and (2) the non-uniform heterogeneous nature of the poly-Si film surface as it contains grain boundaries and grain junctions.

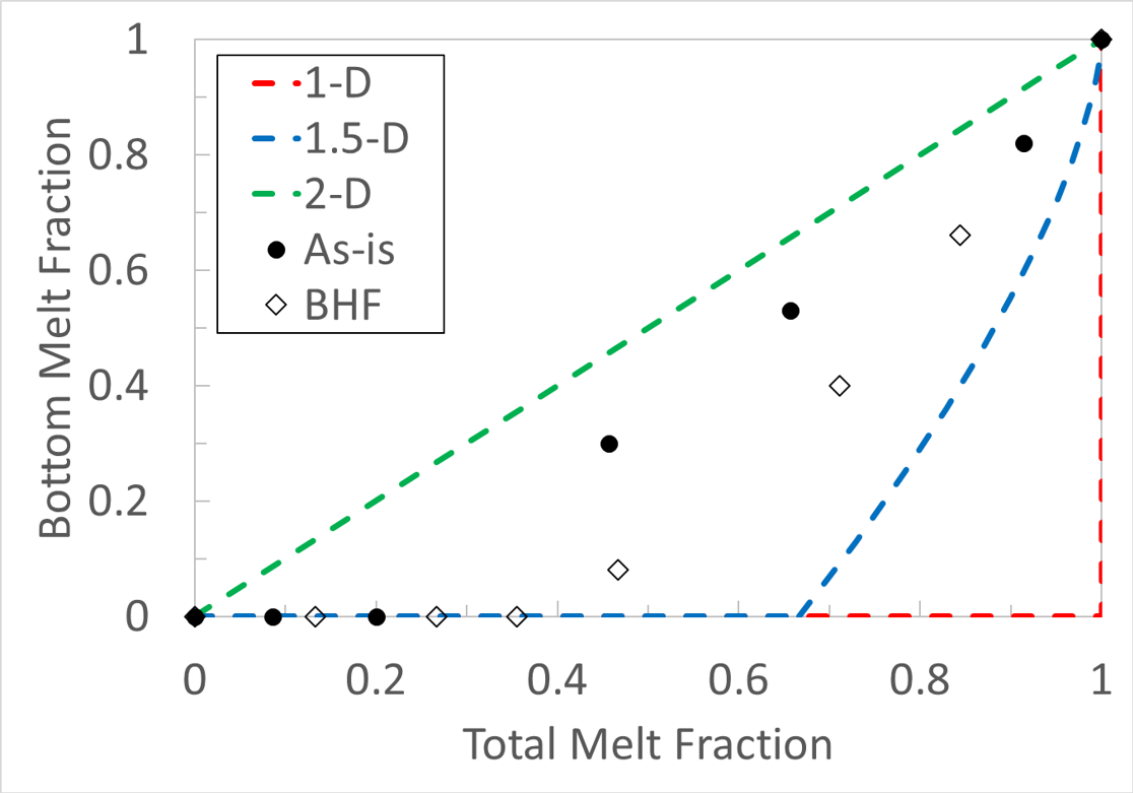

Figure 5.9: Maximum bottom melt fractions versus maximum total melt fractions obtained during surface-side irradiation of the as-is (closed circles) and BHF-treated (open diamonds) ELA poly-Si films. The films were irradiated using a 30-ns at FWHM beam profile at various energy densities. The 1-D (dashed red curve), 1.5-D (dashed blue curve), and 2-D (dashed green curve) melting limits are plotted as well.

5.5 Other Factors Affecting Melting Dimensionality

The most salient finding of this thesis corresponds to the melting (and solidification) transformations in pulsed-laser irradiated ELA poly-Si films occurring in a remarkably and largely 2-D manner. Such melting, which initiates at grain boundary regions followed by lateral melting into the transiently superheated grain center, is enabled by the presence of grain boundaries comprising the columnar-grained microstructure of the films. It is these melt-prone grain boundaries that constitute the intrinsic mechanism responsible for the observed 2-D melting behavior.

While grain boundary melting is the primary driving force behind the 2-D nature of melting in irradiated ELA poly-Si films, several ELA process-related details can also affect (albeit to a lesser degree) the tendency for the local surface of the film to melt relative to the total induced melt fraction of the film (this defines the basis for our interpretation of melting dimensionality), such as pulse duration, incident beam hot spots, and film surface passivation. We have found that those factors can enhance (e.g., increased pulse duration), reduce (e.g., removal of SiO_2 surface layer prior to irradiation), or have little effect on (e.g., preclusion of hot spots) the degree of 2-D melting taking place in the films. Nevertheless, it is important to keep in mind that the observed melting behavior always remains in the 2-D dominated regime (i.e., in between the 1.5-D and 2-D melting limits as shown in the melt fraction

diagrams above) due to the presence of columnar and melt-prone grain boundaries, which ultimately governs the manner by which pulsed-laser-induced melting proceeds in ELA poly-Si films.

Other microstructure-related details, such as film thickness and grain size, can also play an important role in determining the dimensionality of the melting transition (with all else being equal). These details, along with quantitative analysis of the thermal heating profile of the films during pulsed-laser irradiation, will be closely examined via numerical simulations in the next chapter.

5.6 Previous Melting Models

Despite the fact that ELA is a well-established process used extensively in display manufacturing, researchers have proposed several incompatible and diverging models of the critical laser crystallization method over the years [68] [69] [70] [71]. The central difference among the varying models lie in their disagreement regarding the spatiotemporal extent of melting that takes place during pulsed-laser irradiation of poly-Si films. While it is generally accepted that melting is favored to occur at more defective and high-excess-free-energy sites, the details regarding how melting initiates (i.e., location and temperature at which melting begins) and subsequently transpires, particularly within these microstructurally complex polycrystalline films that contain a variety of buried interfaces (e.g., grain boundaries and Si/SiO_2 interfaces), require further examination.

We have previously recognized that simple 1-D melting and solidification of a columnar-grained poly-Si film cannot result in a gradual evolution of the microstructure, as the continuous bottom surface of the film, which consists of unmelted portions of grains, would then simply regrow epitaxially and vertically to fully recover the initial pre-melted microstructure. Instead, we have suggested, based on the TEM-based microstructure analysis of multiple-shot irradiated poly-Si films, that localized complete melting of the film must at least take place at and near the grain boundaries [17], and furthermore, the asymmetric extent of melting and/or solidification between adjacent grains, as influenced by various physical and thermodynamic factors (e.g., grain size, crystallographic orientation, film thickness, defect density, etc.), will then eventually lead to the apparent growth of some grains and apparent shrinkage (or full elimination) of others. These are the very changes that underlie the gradual increase in the average size and gradual evolution in the overall distribution of the grain size observed during ELA processing of silicon films.

The current discovery regarding the 2-D nature of melting, based on in situ transient reflectance and transmission analysis of single-shot irradiated ELA poly-Si films, forms the basis of our proposed melting model of the ELA process that (1) is consistent with the previous suggestions made by researchers in our group [17], and (2) adds to the argument that, during the melting process, a portion of the interior of the columnar grains must remain entirely solid throughout the thickness of the film (as manifested by the striking absence of a plateau in the transient reflectance and trans-

mission signals obtained during pulsed-laser irradiation of the films). This situation may be argued (and appreciated) as stabilizing and extending the degree of lateral melting of the grains, which, in turn, will enable and facilitate the microstructure evolution observed during ELA.

5.7 Summary

In this chapter, we propose a model used to describe the 2-D melting behavior observed in pulsed-laser irradiated ELA poly-Si films. We suggest, based on the transient reflectance and transmission-based analysis of such films, as well as the various thermal, thermodynamic, and kinetic aspects of the melting-transition-relevant details, that melting of the films initiates via prompt and local complete melting at the grain boundary regions, followed by melting proceeding laterally into the transiently superheated interior of the columnar grains.

The local melt fractions measured at the film surfaces (top and bottom), relative to the total melt fraction of the film, are projected onto a melting dimensionality diagram, which maps out the 1-D-dominated and 2-D-dominated domains in the melt fraction parameter space. By projecting the experimentally measured melt fraction values obtained during irradiation of the ELA poly-Si films, we find that the melting transitions examined in this thesis can all be characterized as showing a dimensionality between the perfect 1.5-D and 2-D melting scenarios (i.e., in the 2-D-dominated melting regime).

The suggested model shares many intrinsic elements in common with, and even further builds upon, the grain-boundary-melting-based model developed previously in our group [17]; however, the model can also be recognized as being fundamentally distinct and different from various other models that have been proposed over the years to account for the ELA process [68] [69] [70] [71].

Chapter 6

Numerical Analysis of Melting

6.1 Introduction

In this chapter, we use a numerical model, called nDNS, to simulate the pulsed-laser-induced melting and solidification transitions in ELA poly-Si films. Such simulations allow us to more quantitatively study (and visualize) the rapid phase transformations, as well as estimate physical parameters critical to the ELA process that would otherwise be difficult to extract via experiment. The results of the simulations are consistent with the conclusions drawn from the transient reflectance and transmission-based experiments presented in previous chapters, and further support, and are consistent with, the 2-D melting model developed throughout this thesis.

6.2 Overview and Implementation of the nDNS Numerical Model

The melting and solidification transformations that occur in silicon films during ELA processing are highly nonlinear processes that involve several coupled temperature-dependent, phase-dependent, and material-dependent parameters. Quantitative investigations of such phase transitions are best handled via numerical simulations. In this chapter, we utilize a software package called **nDNS** to simulate and analyze rapid melting and solidification in pulsed-laser irradiated ELA poly-Si films.

nDNS is a numerical simulation program designed to investigate the first-order phase transitions in laser irradiated thin films under far-from-equilibrium conditions [85][86][87]. It uses a cellular-automata-based model to simulate melting and solidification in n-dimensional space (where $n = 1, 2,$ or 3) with nanosecond time-step resolution. Central to the implementation of nDNS is the subdivision of the thin-film system into an array of orthorhombic "nodes". This grid of nodes is used simultaneously to model laser energy absorption, heat flow, nucleation, and solid/liquid interface motion. Material types and starting phases are designated for each node (or subregion of the system), and the relevant material and phase properties are specified in the form of a set of time-dependent and temperature-dependent physical equations.

The simulations presented in this chapter are simplified to 2-dimensional space and have been shown to generate similar results as those obtained in 3-dimensional

space, which require prohibitively longer computational times and resources. Figure 6.1 schematically illustrates the simulation geometry for the case of a 50-nm-thick poly-Si film consisting of 300-nm grains on a SiO_2 substrate. The diagram is centered around a representative columnar grain showing each half of its neighboring grains. An optimum node size of $5 \times 5\ nm^2$ was selected to maximize the spatial resolution of the simulations (at the expense of required computation time).

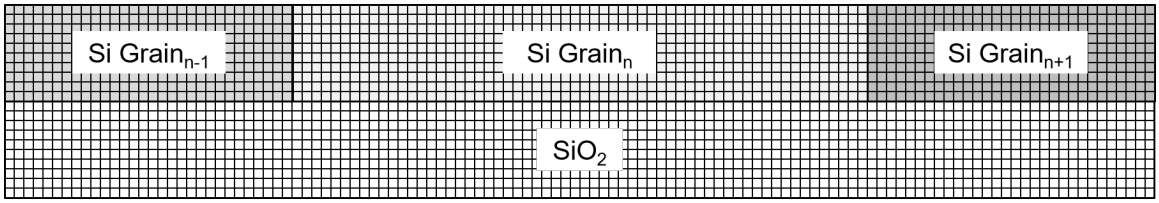

Figure 6.1: Schematic diagram of the simulation geometry for the case of a 50-nm-thick poly-Si film consisting of 300-nm grains on a 500-um-thick SiO_2 substrate (only the top 50 nm of the substrate is shown). Note that in this diagram, for the sake of simplicity, only a single representative columnar grain is shown alongside each half of its neighboring grains. In the simulations, the total film consists of hundreds of columnar grains.

The spatiotemporal profile and wavelength of the incident beam used to heat the films can be readily customized in nDNS, which allows for a wide range of energy deposition configurations. Figure 6.2 shows the time-dependent intensity profile of the incident beam used in the simulations. The simulation results obtained from using this simpler 30-ns step profile are nearly identical to those obtained from using the 30-ns at FWHM beam profile used in actual experiments (see Chapter 3 and 4). The wavelength of the simulated beam is set to 308 nm, which is the wavelength of the excimer laser used in the experiments presented in this thesis.

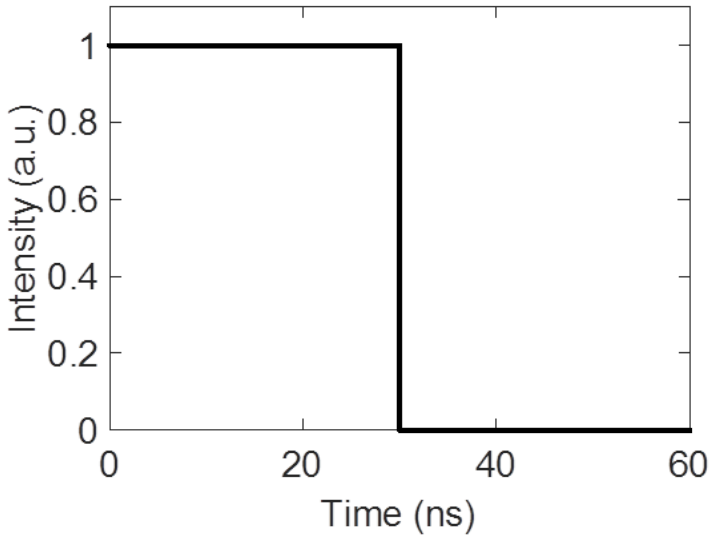

Figure 6.2: Time-dependent intensity profile of the incident beam used in the simulations. The beam energy was spatially uniformly deposited across the irradiated surface of the film.

The energy of the incident beam is uniformly deposited across the irradiated surface of the film causing the temperature of the film to rise. Subsequent heat flow in the film is calculated by solving the general anisotropic heat transport equation (shown in Equation 6.1) using the finite-differences method.

$$c_p(\phi, T)\frac{dT}{dt} = \nabla \cdot (\kappa_T(\phi, T)\nabla T) + \dot{q}_L + \dot{q}_E \tag{6.1}$$

where c_p is the heat capacity, ϕ is the phase, T is the temperature, t is the time, κ_T is the thermal conductivity, $\dot{q}_L$ is the latent heat released upon solidification (i.e. recalescence) or absorbed upon melting (i.e., decalescence) at the solid-liquid interface, and $\dot{q}_E$ is the heat generated from external heat sources, such as the incident beam. Due to the nanosecond timescale of the irradiation process, radiative and

convective heat losses to the environment are ignored.

Upon sufficient heating of the film, melting can initiate at the solid-phase nodes (i.e., transform to liquid-phase nodes) deterministically at a pre-defined temperature, or stochastically with increasing probability for liquid nucleation to occur as the measured degree of superheating increases. The nodes comprising grain boundaries are permitted to deterministically melt at the equilibrium melting point of silicon, or T_m (1685 K). On the other hand, the nodes located within the bulk of the film, or at the Si/SiO_2 interface, require a large degree of superheating (approximately >200 K) in order for any appreciable liquid nucleation to stochastically occur. Such melting restrictions are based on recent experimental findings [54] and are consistent with fundamental energy considerations [82][83][84].

The initiation of melting creates a solid/liquid interface, which can move into adjacent (1) solid-phase nodes at temperatures above T_m during film melting, or (2) liquid-phase nodes at temperatures below T_m during re-solidification of the film. The temperature-dependent velocity of the interface is described by the empirical interface response function for silicon [1], which is shown in Figure 6.3. This interface is monitored using a non-equilibrium interface tracking algorithm, which allows for deep superheating and undercooling to take place at the interface. Simpler linearized forms of the interface response function are used in the simulations presented here and, under moderate superheating and undercooling conditions (<400 K), have been shown to generate similar results as those obtained using the approximate non-linear

forms of the interface response function.

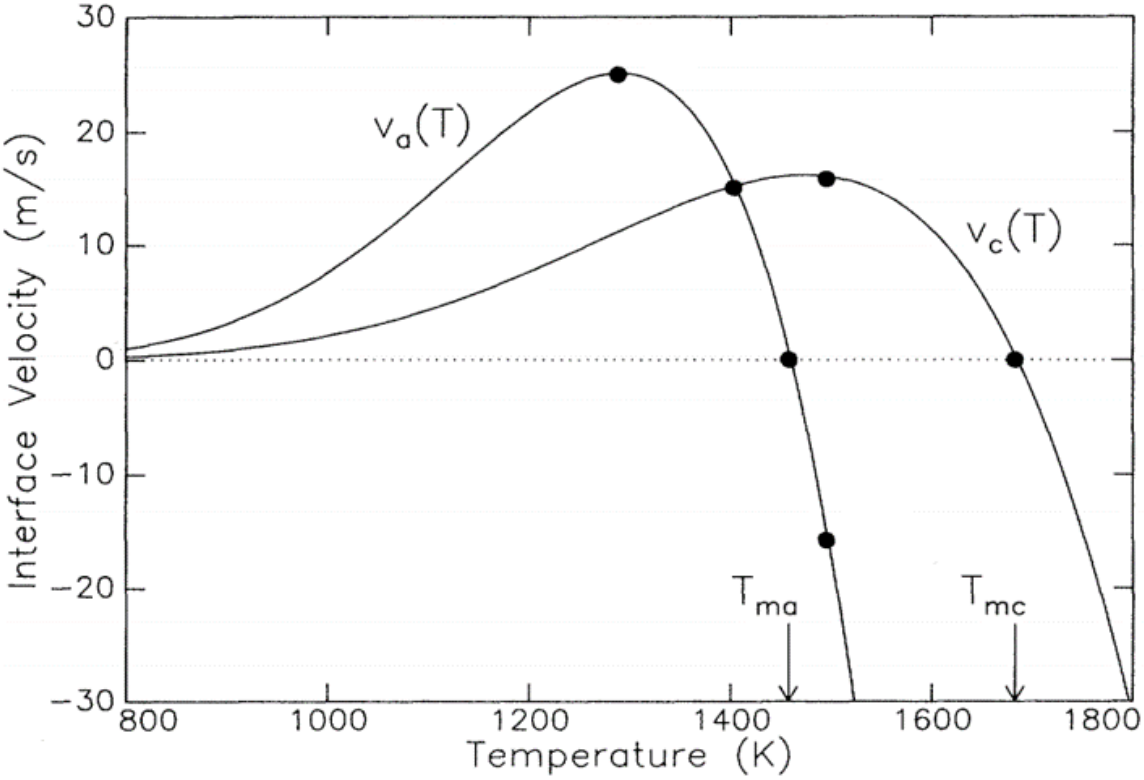

Figure 6.3: Interface response function of amorphous and crystalline silicon (adapted from [1]). Negative and positive values of the interface velocity correspond to melting and solidification, respectively.

To accurately capture the non-isothermal and transient nature of the laser irradiation process, experimental values of material properties, such as heat capacity, thermal conductivity, and absorption coefficients, for example, were defined in the simulations. Additional details of the nDNS software package can be found elsewhere [85][86][87].

6.3 Simulation Results

Here, we present the nDNS results obtained during the pulsed-laser irradiation of silicon films which contain a microstructure representing that of ELA poly-Si films. These simulated films are 50-nm-thick, consist of 300-nm grains that are passivated with a 5-nm layer of SiO_2 (i.e., single layer of SiO_2 nodes), and sit on a 500-um-thick SiO_2 substrate. We refer to such films henceforth as ELA-like poly-Si films.

As we are most interested in investigating the "intrinsic" melting scenario in which "extrinsic" incident beam hot spots do not participate in the melting process, the ELA-like poly-Si films undergo substrate-side irradiation (see Chapter 4 for a review of the formation of LIPSS-induced hot spots at the film surface), whereby the energy of the incident beam is first passed through the SiO_2 substrate and then uniformly deposited at the bottom surface of the film. The time-dependent intensity profile of the incident beam is given in Figure 6.2.

Figure 6.4 shows phase boundary diagrams that were obtained during substrate-side irradiation of the ELA-like poly-Si film at an energy density just below the CMT. The colored diagrams show the phase evolution of a representative columnar grain alongside each half of its neighboring grains throughout the pulsed-laser-induced melting-and-solidification cycle. The solid-phase individual grains are distinguished with alternating colors of red and green, while the liquid-phase melt is denoted with blue. The color of the solid/liquid interface can be orange or yellow (depending on the color of the contacting solid grain).

Figure 6.4(a) and Figure 6.4(b) show the phase boundary diagrams taken at specific time steps that capture the most notable instances of the melting and solidification transformations, respectively. The melting transition effectively begins via prompt and complete melting at the grain boundaries ($t = 0 - 17$ ns), followed by lateral melting into the interior portions of the unmelted grains ($t > 18$ ns) until the incident beam terminates and the maximum extent of (partial) melting of the film is reached soon thereafter ($t = 31$ ns). The film then rapidly quenches via thermal conduction to the substrate below, which triggers lateral growth from the unmelted grain center regions ($t > 32$ ns) until total re-solidification of the film is complete ($t = 58$ ns). The most striking feature of the simulation corresponds to the lack of complete melting at the surfaces of the film despite the relatively high energy density of the incident beam. This is consistent with the transient reflectance and transmission-based experimental results presented in Chapters 3 and 4, and further supports the notion that melting in these columnar-grained films transpires in a predominately 2-D manner.

Next, we present the thermal analysis results obtained during substrate-side irradiation of the ELA-like poly-Si film at an energy density just below the CMT. Figure 6.5 shows the temperature evolution of the top and bottom film surfaces for the time steps leading up to point at which the maximum degree of superheating is achieved. The nature of the substrate-side irradiation configuration results in (1) the temperature profile of the bottom surface always being greater than that of the top

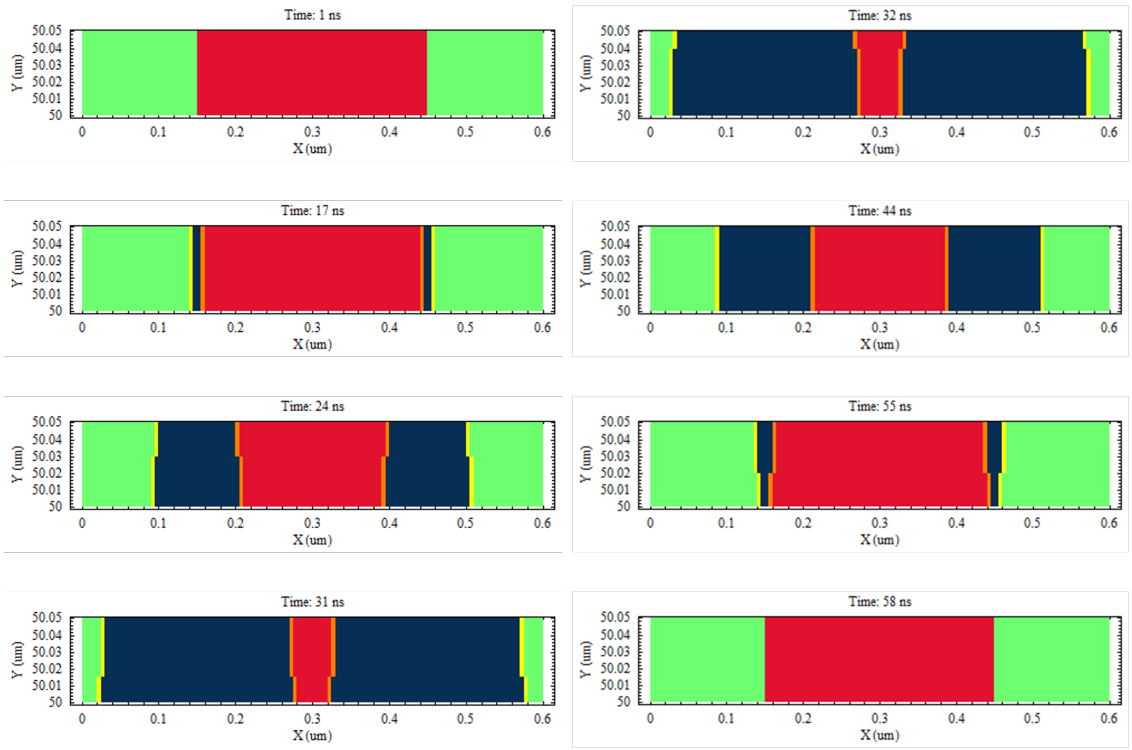

(a) (b)

Figure 6.4: Colored phase boundary diagrams showing the (a) melting, and (b) solidification evolution of a representative section of the ELA-like poly-Si film during substrate-side irradiation at 0.95 CMT. The solid-phase individual grains are distinguished with alternating colors of red and green, while the liquid-phase melt is denoted with blue. The color of the solid/liquid interface can be orange or yellow (depending on the color of the contacting solid grain).

surface during melting, and (2) the uniform irradiation of the film (as hot spots are avoided). This latter point can be seen in Figure 6.5 during solid-phase heating of the film ($t = 13$ ns) where the temperature curves associated with the top and bottom surfaces appear flat due to the spatially uniform irradiation profile of the incident beam.

As the beam heats the film to temperatures above T_m ($t > 13$ ns), melting initiates at the grain boundaries creating a heat-consuming solid/liquid melting interface (i.e.,

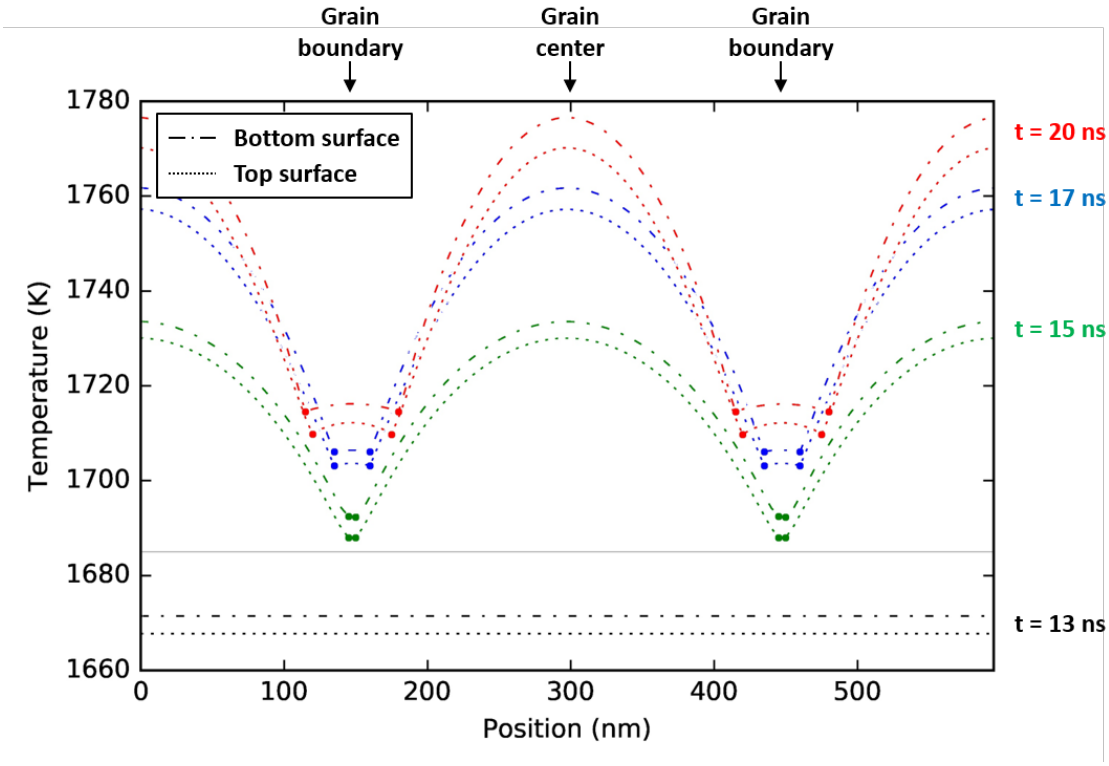

Figure 6.5: Thermal analysis of the ELA-like poly-Si film during substrate-side irradiation at 0.95 CMT. The plots, which are centered around a representative grain surrounded by each half of its neighboring grains, show the temperature versus time evolution of the top (dotted lines) and bottom (dotted-dashed lines) surfaces of the film. Select time steps of the melting process are shown, which capture the moments leading up to the maximum degree of superheating sustained in the film. The closed circles indicate the position of the solid/liquid interface. The horizontal gray line designates the equilibrium melting point of silicon, or T_m (1685 K).

interfacial decalescence transpires at the melt front as melting is an endothermic process), which, in combination with the reduced absorption of excimer-laser light for liquid silicon [88], causes the temperature of the melted regions to slowly rise compared to the unmelted regions during continued heating of the film. The unmelted grain centers far away from the endothermic melt front rapidly rise in temperature to reach a maximum degree of superheating of 90 K ($t = 20$ ns).

Figure 6.6 shows the temperature evolution of the top and bottom film surfaces for the period between the times at which the maximum degree of superheating and the maximum extent of (partial) melting are achieved. As lateral melting proceeds into the transiently superheated interior of the grain ($t > 21$ ns), and the moving endothermic melt front cools the nearby regions ahead, the temperature of the grain center starts to decline (despite ongoing irradiation of the film). All the while, the molten zones continue to slowly rise in temperature, and even surpass the temperature of the superheated grain center, until the incident beam terminates ($t = 30$ ns) and both the top and bottom surface temperatures collapse towards the T_m. Note that the temperature of the film bottom is now below that of the film top. This is due to the intimate contact, and subsequent thermal conduction, between the bottom surface of the film and the underlying substrate serving as a heat sink. At this point, the film has reached the maximum extent of (partial) melting, and, upon further cooling to temperatures below T_m, can begin to re-solidify.

Figure 6.7 shows the temperature evolution of the top and bottom film surfaces during re-solidification. After the termination of the incident beam, the film rapidly and continuously quenches via thermal conduction to the SiO_2 substrate below, where upon cooling to temperatures below the T_m ($t = 31$ ns), the onset of re-solidification is triggered in the partially melted film. As solidification initiates from the unmelted grain centers and lateral growth proceeds into the adjacent supercooled liquid regions ($t > 31$ ns), the local molten zones immediately ahead of the solidifying interface expe-

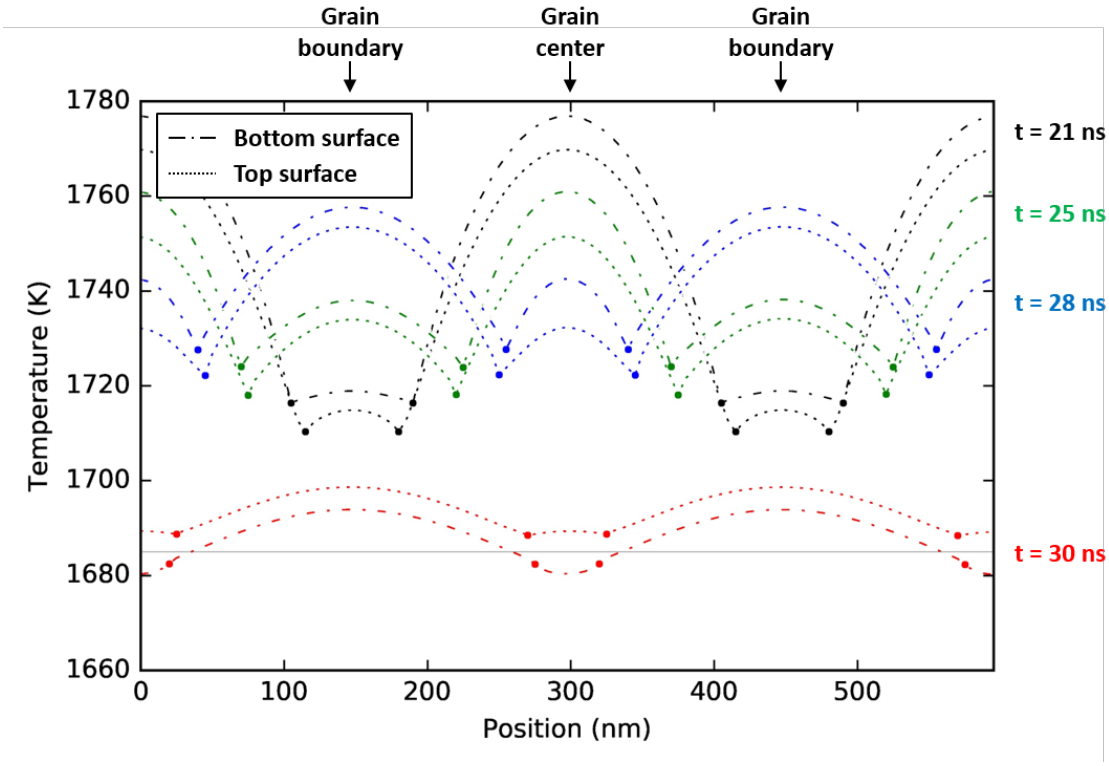

Figure 6.6: Thermal analysis of the ELA-like poly-Si film during substrate-side irradiation at 0.95 CMT. The plots, which are centered around a representative grain surrounded by each half of its neighboring grains, show the temperature versus time evolution of the top (dotted lines) and bottom (dotted-dashed lines) surfaces of the film. Select time steps of the melting process are shown, from the time at which the maximum degree of superheating is sustained within the film to the time at which the maximum extent of (partial) melting in the film is achieved. The closed circles indicate the position of the solid/liquid interface. The horizontal gray line designates the equilibrium melting point of silicon, or T_m (1685 K).

rience a slight rise in temperature due to the heat released at the moving solid/liquid solidifying interface (i.e., interfacial recalescence occurs at the interface as solidification is an exothermic process). The film eventually fully re-solidifies, and in the absence of a heat-generating solidification front, the temperature curves associated with the top and bottom surfaces of the film begin to flatten while continuing to cool ($t = 57$ ns).

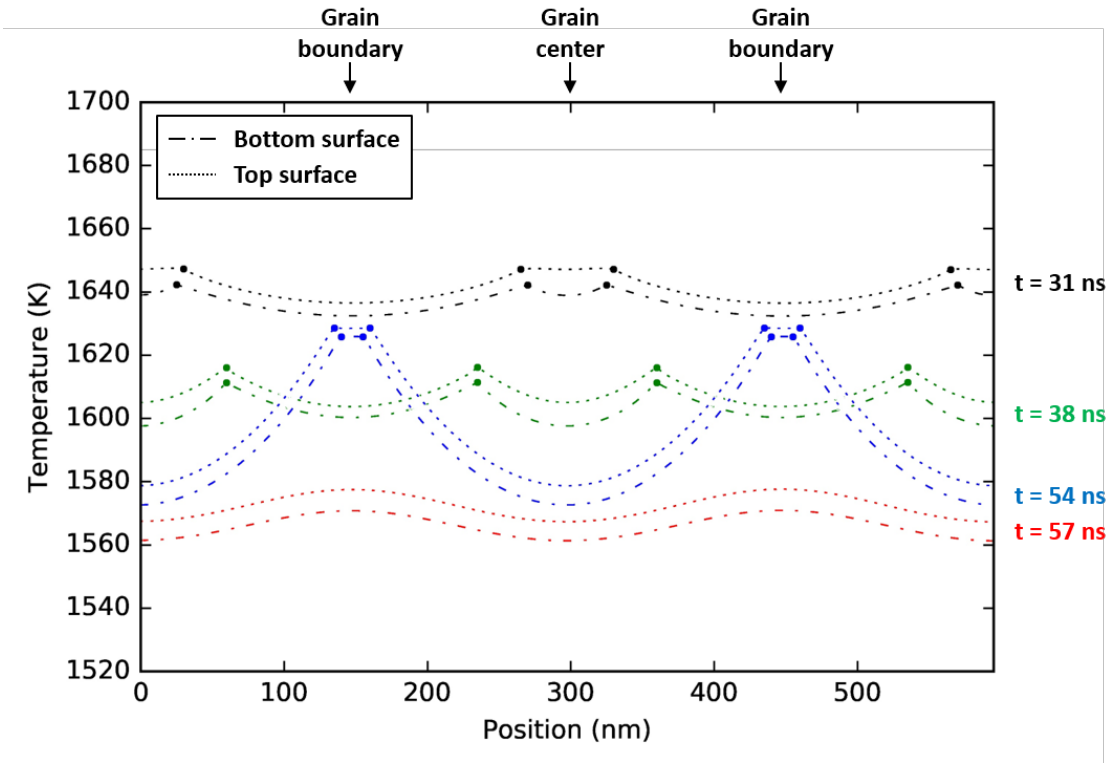

Figure 6.7: Thermal analysis of the ELA-like poly-Si film during substrate-side irradiation at 0.95 CMT. The plots, which are centered around a representative grain surrounded by each half of its neighboring grains, show the temperature versus time evolution of the top (dotted lines) and bottom (dotted-dashed lines) surfaces of the film. Select time steps of the solidification process are shown, starting from the onset of re-solidification and ending with the time at which the film is fully solidified. The closed circles indicate the position of the solid/liquid interface. The horizontal gray line designates the equilibrium melting point of silicon, or T_m (1685 K).

Finally, we perform nDNS simulations of the pulsed-laser-induced melting-and-solidification cycles in ELA-like poly-Si films irradiated at various energy densities with a focus on quantitatively investigating the extent of superheating that takes place in the films. Figure 6.8 shows the maximum degree of superheating sustained in substrate-side irradiated ELA-like poly-Si films at various energy densities. No amount of superheating is recorded at energy densities below the PMT (or 0.61 CMT) since the temperature of the unmelted films never exceed the T_m. However, with increasing energy density above the PMT, the maximum degree of superheating measured in the films doubles from 50 K (at 0.65 CMT) to 100 K (at 1.0 CMT), yet still does not exceed the superheating limit of silicon at the Si/SiO_2 interface (estimated to be at least 200 K above T_m [54]). As demonstrated in the phase boundary diagrams and thermal analysis plots presented earlier (for the case of the substrate-side irradiated ELA-like poly-Si film at 0.95 CMT), it is the silicon at the bottom Si/SiO_2 interface near the grain center that corresponds to the region in the film which experiences the greatest amount of superheating.

6.4 Discussion

Let us begin the discussion by first acknowledging that nDNS is a kinetic-based model and is not designed to minimize the total energy of the simulated system (whereas a more thermodynamic-centric model could). The present model does not consider the change in chemical potential, and subsequent depression or elevation of the local

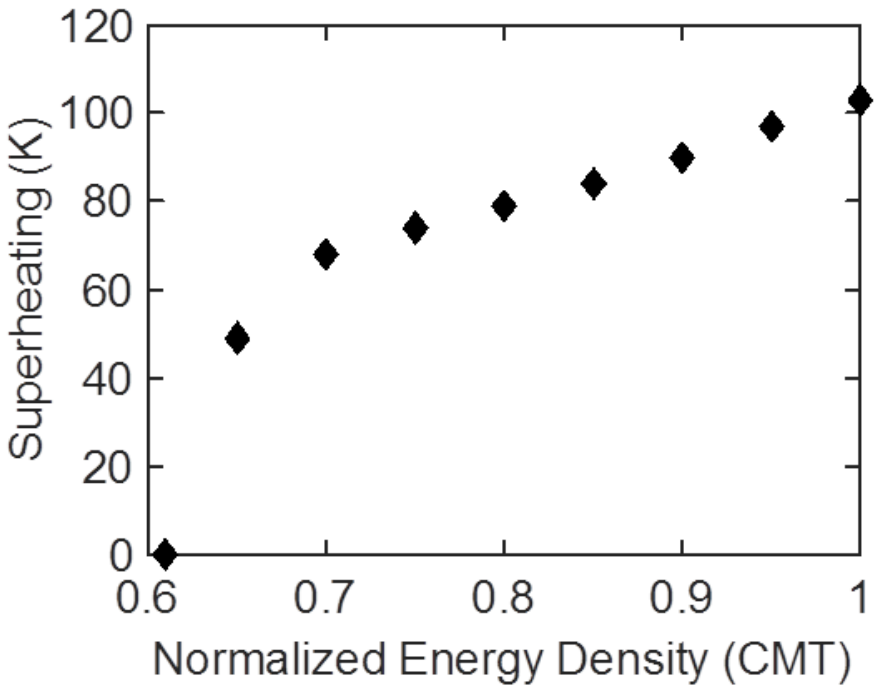

Figure 6.8: Maximum degree of superheating sustained in the substrate-side irradiated ELA-like poly-Si films at various energy densities.

equilibrium point, across an interface due to its curvature (as described by the Gibbs-Thomson effect [37]), nor does it consider the difference in melting and solidification velocities, as well as equilibrium temperatures, between dissimilar grains as manifested by crystallographic anisotropy (and resulting in a grain-orientation-dependent interface response function [89]). Such thermodynamic factors, while significant at near-equilibrium conditions, can be reasonably omitted in the current simulations of the far-from-equilibrium ELA process.

Nevertheless, we appreciate the capability afforded by the nDNS simulation package in its current state to (1) accurately model (to a satisfactory degree) the rapid

phase transformations in pulsed-laser irradiated silicon films, and (2) readily customize various process-related details critical to ELA and study their effect on melting and solidification (as doing so experimentally can be quite challenging). One exemplary case in which we leverage this unique ability of nDNS is to generate a uniform heating profile at the film surface. Doing so enables us to examine the "intrinsic" melting scenario in ELA-like poly-Si films devoid of "extrinsic" hot spots, which are typically present during actual experiments, and which inevitably alter the melting transition.

The results (which take the form of phase boundary diagrams) obtained from simulations of these uniformly heated films allow us to visualize, for the first time, the 2-D nature of melting in these columnar-grained films through a cross-sectional viewing lens. Consistent with our suggested experiment-based model of melting, we observe that the simulated melting transformations initiate via prompt and local complete melting at the grain boundaries, followed by lateral melting towards the interior portions of the unmelted grains. The observed 2-D melting behavior is permitted in accordance to the melting restrictions enacted in the nDNS program, which include (1) melt initiation at temperatures at or slightly above the T_m for silicon nodes located at grain boundaries [45][48], and (2) melt suppression for those silicon nodes located at the Si/SiO_2 interface (as well as in the bulk crystal) until significant superheating (200 K above the T_m) is reached [55].

It is the preferential and heterogenous formation of liquid at grain boundaries

(resulting in prompt and complete melting of the grain boundaries at or slightly above the T_m) that facilitates the onset of 2-D melting. However, a more subtle, but important and less self-evident, element of the 2-D melting process corresponds to the maximum degree of superheating sustained at the interior of a grain (which, in the present analysis, is positively correlated with the incident beam energy density) during lateral melting. This capacity for superheating is critical in preventing the initiation of melting from taking place at the irradiated film surface (in contact with a continuous SiO_2 layer), which would otherwise result in the melting transition becoming more 1-D in nature.

The thermal analysis performed on the irradiated ELA-like poly-Si films show that (1) the irradiated surface, especially at the center portions of the columnar grains (away from the heat-consuming melt front), corresponds to the hottest region of the film during the heating phase, and (2) the silicon located at this SiO_2-passivated surface can reach temperatures up to 100 K above the T_m during (partial) melting, which, while not insignificant, remains well below the estimated maximum limit of superheating for silicon at the Si/SiO_2 interface (200 K above the T_m) [54]. Such findings suggest that liquid nucleation (or at least any appreciable amount of nucleation) at the relatively mildly superheated grain centers should not be expected during pulsed-laser irradiation of the films. This lack of nucleation of liquids at the film surface can assist the films to melt in a more 2-D manner.

Physically and thermodynamically, this indicates that the Si/SiO_2 interface is rel-

atively stable (i.e., melt-resistant) while the high-angle grain boundaries are relatively unstable (i.e., melt-prone). It is these critical thermodynamic properties in tandem that enable the 2-D melting behavior observed (via the nDNS thermal model) in the pulsed-laser irradiated ELA-like poly-Si films. In addition, the magnitude of the interfacial energy between the silicon surface and the oxide must be less than that of either the free surface energy of silicon or the high-angle silicon grain boundary energy. Available data regarding the values of these quantities is found to be consistent with the above statement derived from our simulation, as well as experimental, results [82][83][84].

6.5 Summary

In this chapter, we employed the nDNS software program to simulate the melting and solidification transformations experimentally observed in pulsed-laser-irradiated ELA poly-Si films. The thermal model used in the nDNS program, which was initially developed within our group to study solidification in rapidly heated silicon films [85][86][87], was adapted to include additional melting criteria to account for (1) the propensity for grain boundaries to melt with little thermodynamic resistance at temperatures at or near the T_m, and (2) the ability for silicon at the Si/SiO_2 interface to resist the onset of melting (via the nucleation of liquids) at temperatures up to 200 K above the T_m [54].

Phase boundary diagrams generated using this nDNS thermal model show that

silicon films which contain a microstructure representing that of actual ELA poly-Si films can melt (and later re-solidify) in a remarkably and largely 2-D manner, whereby melting initiates via grain boundary melting, followed by melting proceeding laterally into the transiently superheated interior of the columnar grains.

Subsequent thermal analysis show (via temperature evolution plots of the film surface profile) that the hottest region of the (partially) melted films, which corresponds to the irradiated surface of the unmelted grain center, does not exceed the estimated maximum superheating limit of silicon at the SiO_2 interface. As such, we conclude that any appreciable amount of liquid nucleation within the grain is not expected to transpire during ELA processing.

The quantitative information extracted from the simulations performed here are consistent with the conclusions drawn from the experiments previously discussed in Chapters 3 and 4, and further supports, and is consistent with, the 2-D melting model suggested in Chapter 5.

Chapter 7

Implications on Laser-Induced Melt-Mediated Crystallization

7.1 Introduction

Over the years, the demand for high-performance TFT-enabling crystallized silicon films has steadily increased for their use in the backplane of advanced displays. As a result, several laser-induced melt-mediated crystallization techniques, such as SLS [7] and MPS [58], have emerged that can transform as-deposited a-Si films on SiO_2 into a variety of well-controlled polycrystalline microstructures. However, for various reasons, ELA [6] has become the single most dominant crystallization technique used in display manufacturing.

The resulting polycrystalline microstructure generated during ELA, and other

partial-melting-based laser crystallization processes, is very sensitive to the extent in which melting takes place within the films during heating [16]. The microstructure is critically important as it largely determines the material properties, namely the electrical characteristics, of the films, which, in turn, can affect the performance of the transistors fabricated on the films. Clearly, understanding the melting behavior of poly-Si films (as re-solidification simply follows in a predictable "near-equilibrium" manner from the unmelted solid regions) may lead to profound technological implications. In this chapter, we discuss the present state and knowledge regarding the ELA process in light of the 2-D melting model.

7.2 The Current State of ELA

Display manufacturers have long relied on laser-induced melt-mediated crystallization of silicon films as a way of creating polycrystalline films on low-thermal-budget substrates, such as glass or plastics. To date, the prevailing crystallization method of choice is that of the ELA process, which utilizes an excimer laser to repeatedly irradiate and subsequently transform (over the course of approximately twenty iterative pulses) an initially amorphous film into a polycrystalline film consisting of relatively large and periodic grains, as shown in Figure 7.1. With each pulsed-laser-induced (partial) melting-and-solidification cycle, the microstructure of the silicon film gradually evolves such that the grains become regularly arranged and the average grain size softly saturates towards the wavelength of the laser source (308 nm).

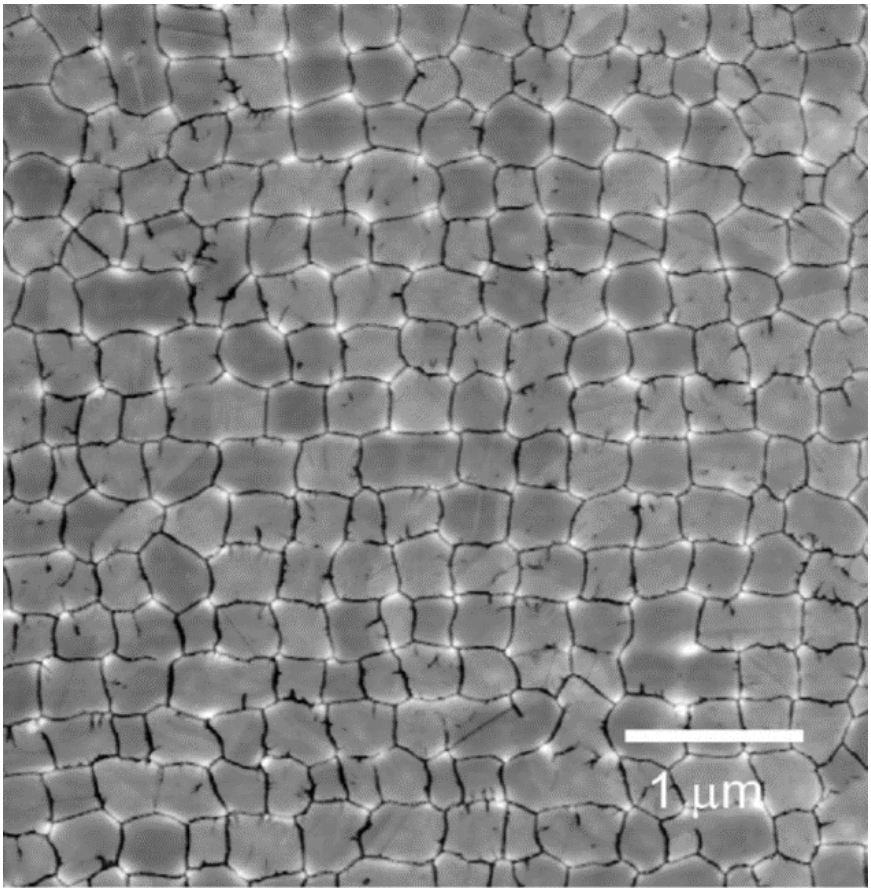

Figure 7.1: AFM surface morphology plot (adapted from [4]) of a silicon film after ELA processing. Prior to imaging, the film was defect-etched to show grain boundaries and other crystal defects.

Even though ELA is a well-developed and long-investigated crystallization technique, some of its most basic melting-transition-related details (which can determine the microstructure evolution and the subsequent microstructural quality of the resulting material) have not yet been clearly deciphered. Several incompatible models used to describe the process have been proposed in the past, however, those models are wildly diverging in regard to their position on the spatiotemporal extent of melting that occurs in the films during rapid heating [68] [69] [70] [71]. Clearly, a better under-

standing of the all-important dynamics of melting manifested during ELA-processing of poly-Si films is greatly desired for its (1) scientifically interesting merits, and (2) technological implications, as there remains a strong interest in further improving the microstructural uniformity of the ELA-generated polycrystalline films while further decreasing the operating costs associated with the process.

To this end, this thesis has focused on more closely examining the melting situation after the first few pulses (which involve the explosive crystallization of the initial amorphous material [34] [15]) in the ELA process, whereby poly-Si films consisting of columnar grains undergo pulsed-laser-induced (partial) melting.

7.3 Implications of 2-D Melting on ELA

7.3.1 Findings Related to Melting Dimensionality

We have shown via transient reflectance and transmission analysis that irradiated ELA poly-Si films can melt in a remarkably and largely 2-D manner. Based on these findings, as well as considering our previous TEM-based microstructure analysis of multiple-shot irradiated poly-Si films [17], we attribute this behavior (at least partially and intrinsically) to (1) prompt initiation of melting occurring at the melt-prone grain boundaries and grain junctions, and (2) subsequent melting of the liquid into the transiently superheated center regions of the unmelted grains. Considering these experimental results, and in conjunction with complementary simulation-based

modeling, we can now discuss the significance of the dimensionality of melting on the ELA process.

Previously, it was suggested that localized complete melting in columnar-grained poly-Si films must at least take place at and near the grain boundaries in order for microstructure evolution to proceed [17]. The apparent growth of some grains and effective shrinkage (or full elimination) of others was attributed to the asymmetric extent of melting and solidification between neighboring grains, as influenced by various physical and thermodynamic factors (e.g., grain size, crystallographic orientation, film thickness, defect density). This argument was made to account for the gradual increase in the average grain size and evolution in the overall grain size distribution observed during ELA.

If, however, the columnar grain boundaries do not undergo complete melting throughout the thickness of the film, then no displacement of those grain boundaries (nor subsequent evolution of the grain size) is possible as the boundaries are affixed to their initial locations by the unmelted portions of the film. This realization can be inversely applied by suggesting that the total measured displacement of the fully melted grain boundary is correlated to the extent of localized melting transpiring at the bottom Si/SiO_2 interface.

The above considerations lead us to recognize that one way to capture the microstructure-evolution-related details regarding pulsed-laser-induced (partial) melting of columnar-grained poly-Si films is to track the maximum local melt fraction measured at the

bottom Si/SiO_2 interface as a function of the total melt fraction of the film (the value of which should approximately scale linearly with the energy density of the incident beam). The bottom melt fraction can be treated as an indirect measure of the extent of melting transpiring at grain boundaries (which is to also say, a measure of the extent of microstructure evolution that one can expect) if liquid nucleation at the interior of the grain is not triggered (as is the case in ELA processing according to the simulation-based thermal analysis results obtained in Chapter 6). Such melt fraction-centric plots demonstrate how the dimensionality of the melting transition can affect the energy-utilization efficiency of the ELA crystallization technique, as well as the robustness of the technique to inevitable process fluctuations (e.g., pulse-to-pulse energy density variations or non-uniformities in the incident beam spatiotemporal profile) that are detrimental to the microstructural uniformity of the resulting material. Furthermore, the plots, as we will show below, help us to identify and appreciate the observed 2-D melting behavior in irradiated ELA poly-Si films as being an important process-enabling element of ELA since this 2-D melting scenario permits microstructure evolution of the grains to transpire more effectively than when melting takes place in a less 2-D manner (i.e., 1-D melting).

7.3.2 Melting Dimensionality in Films of Varying Thicknesses

As an example to showcase the correlation between the dimensionality of melting and the extent of melting happening at and near the columnar grain boundaries

(and hence the degree of microstructure evolution during ELA processing), we have employed nDNS to simulate (partial) melting in ELA-like poly-Si films at 20, 50, and 200-nm film thicknesses. The films sit on a SiO_2 substrate and consist of 300-nm grains passivated with a SiO_2 surface layer. A 30-ns at FWHM beam profile is used to uniformly irradiate the surface of the films at 0.95 CMT, and under these heating conditions, the grain boundaries correspond to the only sites where melting initiates. The details of the implementation of the nDNS model are described at length in Chapter 6.

Here, it is important to point out that the manner in which we have defined "melting dimensionality" in these columnar-grained films captures the competition between the extent of localized vertical melting transpiring at the grain boundary (which depends on, among other things, the thickness of the film) versus the extent of lateral melting taking place at the surface of the films (which depends on the size of the grains provided that melting is simply initiated only at grain boundaries and grain junctions). In addition to the thickness and grain size of the films, several other experimental and physical factors (e.g., laser pulse duration, incident beam hot spots, surface passivation layer) can influence the dimensionality of the melting transition, as was shown in previous chapters.

The stark differences in melting behavior between thinner and thicker films (with all else being equal), as shown in Figure 7.2, are compelling when viewed from the perspective of melting dimensionality as defined above. Figure 7.2(a) shows the evolu-

tion of melting in the 20-nm-thick film where the melting transition can be described as proceeding in an almost perfect 2-D (or lateral melting) manner. Here, prompt and complete localized melting is attained at the grain boundary regions as soon as the film begins to melt (i.e., at energy densities just above the PMT). On the other hand, complete melting of the film surface is realized only upon complete melting of the total film (i.e., at energy densities near the CMT). The situation for the 200-nm-thick film, as shown in Figure 7.2(c), is markedly different. The observed melting behavior can be characterized as proceeding in a near 1-D manner, whereby the solid/liquid melting interface propagates vertically downwards and full melting of the columnar grain boundaries is avoided even at relatively high energy densities up to the CMT. Lastly, Figure 7.2(b) shows the melting transformation in a 50-nm-thick film (the typical film thickness employed in ELA). The dimensionality of melting can be categorized as being predominately 2-D, although not quite to the same degree as was observed in the ultra-thin film case.

Figure 7.3 plots the maximum bottom melt fraction (measured at the bottom Si/SiO_2 interface) versus the total melt fraction for the 20, 50, and 200-nm-thick films. Such a plot, which also shows the melt fraction values expected for the perfect 1-D and 2-D melting scenarios, captures and demonstrates the points made earlier regarding the impact of the melting dimensionality on the ELA process. The plot shows that, as far as microstructural evolution of the grains is concerned, the ELA process should become more efficient in terms of beam-energy utilization when melting of the films

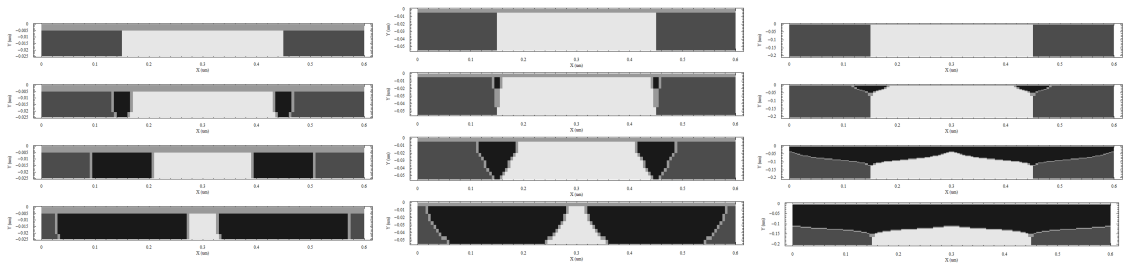

(a) (b) (c)

Figure 7.2: Phase boundary diagrams showing the melting evolution of a representative section of the (a) 20-nm-thick, (b) 50-nm-thick, and (c) 200-nm-thick ELA-like poly-Si films (consisting of 300-nm grains) during surface-side irradiation at 0.95 CMT. The solid-phase individual grains are distinguished with alternating colors of dark and light gray, while the liquid-phase melt is denoted with the color black. The results reveal that melting proceeds increasingly in a 1-D manner as the thickness of the film increases for a given grain size.

transpires in an increasingly 2-D manner, as a greater portion of the incident beam is utilized to selectively melt the regions of the film at and near the grain boundaries. As a consequence, smaller grains in the heated films, on average, are more effectively melted away (i.e., eliminated in the grain-size-distribution space) creating regions of liquid for surviving grains to expand into upon re-solidification (i.e., permitting larger net displacements of the grain boundaries between the unmelted grains to take place).

The plot in Figure 7.3 also helps us to conceptualize how 2-D melting behavior diminishes the sensitivity of the ELA process to certain process fluctuations, including pulse-to-pulse variations or beam-profile non-uniformities, especially at relatively high energy densities where the crystallization technique is performed. Note that the slope of the 2-D melting curve (just below the CMT) is much less than that of the 1-D melting curve. This allows for changes in the total melt fraction of the film (resulting

from the aforementioned fluctuations) to lead to commensurately reduced changes in the bottom melt fraction (i.e., extent of melting at grain boundaries), and thus resulting in lessened variations in the final ELA-generated poly-Si film microstructure. This particular benefit of the 2-D nature of melting on ELA cannot be understated, as it can also be directly correlated to (1) the increased width of the optimal processing energy density window, and (2) the increased manufacturing yields of the displays employing ELA poly-Si films. These points correspond to exceedingly important and costly factors in the manufacture of advanced displays.

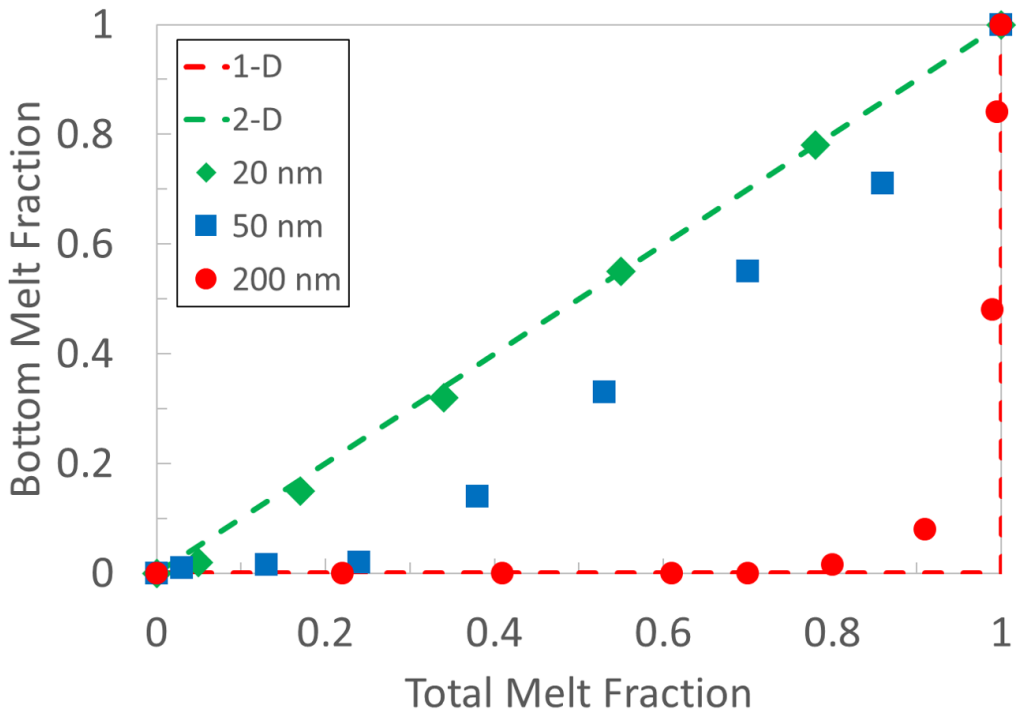

Figure 7.3: Maximum bottom melt fraction versus total melt fraction are plotted for the perfect 1-D and 2-D melting cases (dashed red, blue, and green lines, respectively). Simulated melting in pulsed-laser irradiated 20-, 50-, and 200-nm-thick polycrystalline Si films (as shown in Fig. 2) consisting of 300-nm grains are also plotted (diamond, square, and circles, respectively).

7.3.3 Dimensionality of Melting and Hot Spots

One final point to appreciate in regards to the dimensionality of melting is the role that it should play in the generation of hot spots during ELA. The present 2-D melting model can provide a comprehensive and consistent explanation for how the creation of local hot spots can assist, and be also assisted by, the 2-D nature of melting.

Recall that the hot spots are manifested at the irradiated film surface due to scattering of the incident beam at pre-existing protrusions or other non-planar surface morphological features [73]. Furthermore, that such protrusions appear during the ELA process at the last-to-solidify regions of the film [90] (because of the difference in material density between solid and liquid silicon), which correspond to the grain boundaries and grain junctions [4].

By considering the way these protrusions are formed (as a result of the mass accumulation of silicon during 2-D lateral solidification [72]), we identify that the very formation of the protrusions must at least be further assisted by 2-D melting taking place in the film. This is a point with a significant consequence as it highlights the propensity for 2-D melting to encourage the development of incident beam hot spots, which are recognized as a critical and beneficial factor in enabling the evolution of an unusual and periodic 300-nm-grained microstructure unique to ELA, as shown in Figure 7.1.

Chapter 8

Conclusions

8.1 Summary

The melting of silicon films in contact with SiO_2 is a critical step in partial-melting-based laser crystallization techniques, such as the ELA process used extensively in the manufacture of displays. Although studies on laser-induced melting of amorphous films [15], as well as crystal films [55], have been actively pursued in the past, the transformation-relevant details related to melting in polycrystalline films, especially under ELA processing conditions, have not yet been fully established. We suggest that these all-important dynamics of melting are scientifically interesting and technologically relevant, as further characterization of the melting transition in rapidly heated poly-Si films is necessary in order for ELA to advance to the next level of productivity and capability.

To this end, we have investigated how columnar-grained poly-Si films are partially melted upon being irradiated with excimer-laser pulses. This task is achieved by again irradiating an "ELA poly-Si film" that has previously been optimally prepared using a state-of-the-art ELA system and examining the transformation dynamics using in situ transient reflectance and transmission analysis. The measured signals reveal how melting transpires in a largely and remarkably 2-D manner, which we attribute to (1) the prompt initiation of melting taking place at grain boundaries, and (2) the melting proceeding laterally into the transiently superheated interior of the grains. Numerical simulations of the temperature evolution in the grains show that the hottest regions (i.e., the center of the grains at the SiO_2-passivated surface) remain well below the superheating limit of silicon at the Si/SiO_2 interface [54], and as a result, the nucleation of liquids should be avoided during (partial) melting of the films.

Assuming that grain boundaries correspond to the only sites where melting initiates, we can define the "dimensionality of melting" in these columnar-grained films in such a way as to capture the competition between the extent of melting taking place at the grain boundaries versus the film surface. We advocate that this dimensionality can figure considerably in terms of dictating the efficiency with which the ELA process can generate microstructurally uniform polycrystalline materials.

The current discovery regarding the 2-D nature of melting in ELA poly-Si films is consistent with our previously proposed grain boundary melting model [17], and

furthermore builds on the foundational framework laid by others [58][89][54] in regards to the study of laser-induced melting in polycrystalline microstructures.

8.2 Suggestions for Future Work

We have experimentally investigated the 2-D manner in which ELA poly-Si films melt in great detail. Future work, however, may include examining the melting transition in similar columnar-grained poly-Si films of varying thicknesses where we expect melting to proceed in an increasingly 1-D manner with greater film thicknesses for a given grain size, as was predicted by our numerical simulation-based results. Such experiments would serve as an excellent test of validation for the suggested 2-D melting model, as well as the implementation of the current nDNS software package.

As was previously acknowledged, the nDNS program employs a kinetic-based model that does not account for the change in chemical potential across an interface due to the formation of local curvature, nor does it consider the anisotropic nature of the interface response function for different crystallographic grains. The addition of such thermodynamic factors to the nDNS platform would surely benefit the model in regards to its ability to more accurately simulate experimentally observed melting phenomena.

The findings presented in this thesis can also be leveraged to guide the ongoing development of a new quasi-continuous-wave-laser-based melt-mediated crystallization technique referred to as the spot-beam crystallization method (SBC). While some

process-related challenges remain to be sorted out (e.g., the mitigation of the severity of "thermal spikes", or sudden and prohibitively large increases in film temperature, intrinsic to the method due to the short-pulse nature of the quasi-continuous-wave laser), the fundamental melting-transition-relevant lessons ascertained from this work can be applied to expedite the process development of SBC.

Bibliography

[1] P. Stolk, A. Polman, and W. Sinke, "Experimental test of kinetic theories for heterogeneous freezing in silicon," *Physical Review B*, vol. 47, no. 1, p. 5, 1993.

[2] C. Thompson, "Secondary grain growth in thin films of semiconductors: Theoretical aspects," *Journal of Applied Physics*, vol. 58, no. 2, pp. 763–772, 1985.

[3] D. A. Porter, K. E. Easterling, and M. Sherif, *Phase Transformations in Metals and Alloys, (Revised Reprint)*. CRC press, 2009.

[4] P. C. Wilt, "13.1: Invited paper: Excimer-laser annealing: Microstructure evolution and a novel characterization technique," in *SID Symposium Digest of Technical Papers*, vol. 45, pp. 149–152, Wiley Online Library, 2014.

[5] N. Basov, V. Danilychev, Y. M. Popov, and D. Khodkevich, "Laser operating in the vacuum region of the spectrum by excitation of liquid xenon with an electron beam," *JETP lett*, vol. 12, no. 10, pp. 329–331, 1970.

[6] T. Sameshima, S. Usui, and M. Sekiya, "Xecl excimer laser annealing used in the fabrication of poly-si tft's," *IEEE Electron Device Letters*, vol. 7, no. 5, pp. 276–278, 1986.

[7] R. S. Sposili and J. S. Im, "Sequential lateral solidification of thin silicon films on sio2," *Applied Physics Letters*, vol. 69, no. 19, pp. 2864–2866, 1996.

[8] R. Ishihara, P. C. Van der Wilt, B. D. van Dijk, A. Burtsev, J. Metselaar, and C. Beenakker, "Advanced excimer-laser crystallization process for single-

crystalline thin film transistors," *Thin Solid Films*, vol. 427, no. 1, pp. 77–85, 2003.

[9] P. van der Wilt, B. Turk, A. Limanov, A. Chitu, and J. S. Im, "A hybrid approach for obtaining orientation-controlled single-crystal si regions on glass substrates," in *Lasers and Applications in Science and Engineering*, pp. 61060B–61060B, International Society for Optics and Photonics, 2006.

[10] S. Uchikoga and N. Ibaraki, "Low temperature poly-si tft-lcd by excimer laser anneal," *Thin Solid Films*, vol. 383, no. 1, pp. 19–24, 2001.

[11] M.-K. Kang, H. J. Kim, J. K. Chung, D. B. Kim, S. K. Lee, C. H. Kim, W. S. Chung, J. W. Hwang, S. Y. Joo, H. S. Maeng, *et al.*, "Development of world's largest 21.3" ltps lcd using sequential lateral solidification (sls) technology," *Journal of Information Display*, vol. 4, no. 4, pp. 4–7, 2003.

[12] N. Yamauchi and R. Reif, "Polycrystalline silicon thin films processed with silicon ion implantation and subsequent solid-phase crystallization: Theory, experiments, and thin-film transistor applications," *Journal of Applied Physics*, vol. 75, no. 7, pp. 3235–3257, 1994.

[13] T. Noguchi, "Appearance of single-crystalline properties in fine-patterned si thin film transistors (tfts) by solid phase crystallization (spc)," *Japanese journal of applied physics*, vol. 32, no. 11A, p. L1584, 1993.

[14] J. Tsao and P. Peercy, "Crystallization instability at the amorphous-silicon/liquid-silicon interface," *Physical review letters*, vol. 58, no. 26, p. 2782, 1987.

[15] Q. Hu, *Dynamics of melt-mediated crystallization of amorphous silicon films*. PhD thesis, Columbia University, 2011.

[16] J. S. Im, H. Kim, and M. O. Thompson, "Phase transformation mechanisms involved in excimer laser crystallization of amorphous silicon films," *Applied*

Physics Letters, vol. 63, no. 14, pp. 1969–1971, 1993.

[17] H. Kim and J. S. Im, "Multiple pulse irradiation effects in excimer laser-induced crystallization of amorphous si films," in *MRS Proceedings*, vol. 321, p. 665, Cambridge Univ Press, 1993.

[18] F. A. Lindemann *Phys. Z.*, vol. 11, pp. 609–614, 1910.

[19] M. Born, "Thermodynamics of crystals and melting," *The Journal of Chemical Physics*, vol. 7, no. 8, pp. 591–603, 1939.

[20] H. Fecht and W. Johnson, "Entropy and enthalpy catastrophe as a stability limit for crystalline material," *Nature*, vol. 334, no. 6177, pp. 50–51, 1988.

[21] K. Lu and Y. Li, "Homogeneous nucleation catastrophe as a kinetic stability limit for superheated crystal," *Physical review letters*, vol. 80, no. 20, p. 4474, 1998.

[22] Z. Jin, P. Gumbsch, K. Lu, and E. Ma, "Melting mechanisms at the limit of superheating," *Physical Review Letters*, vol. 87, no. 5, p. 055703, 2001.

[23] Q. Mei and K. Lu, "Melting and superheating of crystalline solids: From bulk to nanocrystals," *Progress in Materials Science*, vol. 52, no. 8, pp. 1175–1262, 2007.

[24] G. Jaeger, "The ehrenfest classification of phase transitions: introduction and evolution," *Archive for history of exact sciences*, vol. 53, no. 1, pp. 51–81, 1998.

[25] D. Auston, C. Surko, T. Venkatesan, R. Slusher, and J. A. Golovchenko, "Time-resolved reflectivity of ion-implanted silicon during laser annealing," *Applied Physics Letters*, vol. 33, no. 5, pp. 437–440, 1978.

[26] G. Galvin, M. O. Thompson, J. Mayer, P. Peercy, R. Hammond, and N. Paulter,

"Time-resolved conductance and reflectance measurements of silicon during pulsed-laser annealing," *Physical Review B*, vol. 27, no. 2, p. 1079, 1983.

[27] D. Turnbull, "Kinetics of heterogeneous nucleation," *The Journal of Chemical Physics*, vol. 18, no. 2, pp. 198–203, 1950.

[28] M. Volmer, "Über keimbildung und keimwirkung als spezialfälle der heterogenen katalyse," *Berichte der Bunsengesellschaft für physikalische Chemie*, vol. 35, no. 9, pp. 555–561, 1929.

[29] R. Becker and W. Döring, "Kinetische behandlung der keimbildung in übersättigten dämpfen," *Annalen der Physik*, vol. 416, no. 8, pp. 719–752, 1935.

[30] B. Rethfeld, K. Sokolowski-Tinten, D. Von der Linde, and S. Anisimov, "Ultrafast thermal melting of laser-excited solids by homogeneous nucleation," *Physical review B*, vol. 65, no. 9, p. 092103, 2002.

[31] R. W. Cahn, "Crystal defects and melting," *Nature*, vol. 273, pp. 491–492, 1978.

[32] J. Poate, *Laser annealing of semiconductors*. Elsevier, 2012.

[33] E. Donovan, F. Spaepen, D. Turnbull, J. Poate, and D. Jacobson, "Heat of crystallization and melting point of amorphous silicon," *Applied Physics Letters*, vol. 42, no. 8, pp. 698–700, 1983.

[34] M. O. Thompson, G. Galvin, J. Mayer, P. Peercy, J. Poate, D. Jacobson, A. Cullis, and N. Chew, "Melting temperature and explosive crystallization of amorphous silicon during pulsed laser irradiation," *Physical Review Letters*, vol. 52, no. 26, p. 2360, 1984.

[35] T. Eiumchotchawalit and J. S. Im, "The mechanism of excimer laser-induced amorphization of ultra-thin si films," *MRS Online Proceedings Library Archive*, vol. 321, 1993.

[36] P. Buffat and J. P. Borel, "Size effect on the melting temperature of gold particles," *Physical review A*, vol. 13, no. 6, p. 2287, 1976.

[37] J. W. Gibbs, *The scientific papers of J. Willard Gibbs*, vol. 1. Longmans, Green and Company, 1906.

[38] R. W. Cahn, "Melting and the surface," *Nature*, vol. 323, no. 6090, pp. 668–669, 1986.

[39] W. Tyson and W. Miller, "Surface free energies of solid metals: Estimation from liquid surface tension measurements," *Surface Science*, vol. 62, no. 1, pp. 267–276, 1977.

[40] J. W. Frenken and J. Van der Veen, "Observation of surface melting," *Physical review letters*, vol. 54, no. 2, p. 134, 1985.

[41] J. Herman and H. Elsayed-Ali, "Superheating of pb (111)," *Physical review letters*, vol. 69, no. 8, p. 1228, 1992.

[42] H. Hakkinen and U. Landman, "Superheating, melting, and annealing of copper surfaces," *Physical review letters*, vol. 71, no. 7, p. 1023, 1993.

[43] B. Chalmers, "Crystal boundaries in tin," *Proceedings of the Royal Society of London. Series A, Mathematical and Physical Sciences*, pp. 100–110, 1940.

[44] R. Kikuchi and J. W. Cahn, "Grain-boundary melting transition in a two-dimensional lattice-gas model," *Physical Review B*, vol. 21, no. 5, p. 1893, 1980.

[45] T. Hsieh and R. Balluffi, "Experimental study of grain boundary melting in aluminum," *Acta Metallurgica*, vol. 37, no. 6, pp. 1637–1644, 1989.

[46] R. Raj, "Premelting at triple grain junctions," *Acta Metallurgica et Materialia*, vol. 38, no. 8, pp. 1413–1416, 1990.

[47] A. M. Alsayed, M. F. Islam, J. Zhang, P. J. Collings, and A. G. Yodh, "Premelting at defects within bulk colloidal crystals," *Science*, vol. 309, no. 5738, pp. 1207–1210, 2005.

[48] S. R. Phillpot, S. Yip, and D. Wolf, "How do crystals melt?," *Computers in physics*, vol. 3, no. 6, pp. 20–31, 1989.

[49] M. Kronberg and F. Wilson, "Secondary recrystallization in copper," *AIME TRANS*, vol. 185, pp. 501–514, 1949.

[50] W. Fan and X.-G. Gong, "Superheated melting of grain boundaries," *Physical Review B*, vol. 72, no. 6, p. 064121, 2005.

[51] T. Frolov and Y. Mishin, "Liquid nucleation at superheated grain boundaries," *Physical review letters*, vol. 106, no. 15, p. 155702, 2011.

[52] L. Zhang, Z. Jin, L. Zhang, M. Sui, and K. Lu, "Superheating of confined pb thin films," *Physical review letters*, vol. 85, no. 7, p. 1484, 2000.

[53] Q. Mei, Z. Jin, and K. Lu*, "The kinetic limit of superheating induced by semicoherent interfaces," *Philosophical magazine letters*, vol. 85, no. 4, pp. 203–211, 2005.

[54] J. J. Wang, A. B. Limanov, Y. Wang, and J. S. Im, "Observation of superheating of si at the si/sio 2 interface in pulsed-laser irradiated si thin films," in *MRS Proceedings*, vol. 1770, pp. 43–48, Cambridge Univ Press, 2015.

[55] J. Wang, *Melting in Superheated Silicon Films Under Pulsed-Laser Irradiation*. PhD thesis, Columbia University, 2016.

[56] R. W. Cahn, "Materials science: Melting from within," *Nature*, vol. 413, no. 6856, pp. 582–583, 2001.

[57] J. L. Tallon, "A hierarchy of catastrophes as a succession of stability limits for the crystalline state," *Nature*, vol. 342, no. 6250, pp. 658–660, 1989.

[58] J. S. Im, M. Chahal, P. Van der Wilt, U. Chung, G. Ganot, A. Chitu, N. Kobayashi, K. Ohmori, and A. Limanov, "Mixed-phase solidification of thin si films on sio 2," *Journal of Crystal Growth*, vol. 312, no. 19, pp. 2775–2778, 2010.

[59] M. A. Crowder, A. T. Voutsas, S. R. Droes, M. Moriguchi, and Y. Mitani, "Sequential lateral solidification processing for polycrystalline si tfts," *IEEE Transactions on Electron Devices*, vol. 51, no. 4, pp. 560–568, 2004.

[60] S. Hazair, P. van der Wilt, Y. Deng, U.-J. Chung, A. Limanov, and J. S. Im, "Nucleation-initiated solidification of thin si films," in *MRS Proceedings*, vol. 979, pp. 0979–HH11, Cambridge Univ Press, 2006.

[61] V. K. Wong, A. Chitu, A. Limanov, and J. S. Im, "Epitaxial growth following crystal nucleation in laser-quenched si films on sio 2," in *MRS Proceedings*, vol. 1770, pp. 67–72, Cambridge Univ Press, 2015.

[62] J. S. Im and H. Kim, "On the super lateral growth phenomenon observed in excimer laser-induced crystallization of thin si films," *Applied Physics Letters*, vol. 64, no. 17, pp. 2303–2305, 1994.

[63] M. Chahal, P. van der Wilt, D. Van Gestel, A. Limanov, A. Chitu, and J. S. Im, "Effect of film thickness variation on (100)-surface texturing of mps processed polycrystalline si films," *MRS Online Proceedings Library Archive*, vol. 1426, pp. 257–262, 2012.

[64] Y. Wang, "Investigation of melting and solidification of thin polycrystalline silicon films via mixed-phase solidification," 2016.

[65] A. Marmorstein, A. T. Voutsas, and R. Solanki, "A systematic study and optimization of parameters affecting grain size and surface roughness in excimer

laser annealed polysilicon thin films," *Journal of applied physics*, vol. 82, no. 9, pp. 4303–4309, 1997.

[66] K. Yoneda, "Recent progress of low temperature poly si tft technology," *MRS Online Proceedings Library Archive*, vol. 508, 1998.

[67] H. Kuriyama, S. Kiyama, S. Noguchi, T. Kuwahara, S. Ishida, T. Nohda, K. Sano, H. Iwata, H. Kawata, M. Osumi, *et al.*, "Enlargement of poly-si film grain size by excimer laser annealing and its application to high-performance poly-si thin film transistor," *Japanese journal of applied physics*, vol. 30, no. 12S, p. 3700, 1991.

[68] H. Kuriyama, T. Nohda, S. Ishida, T. Kuwahara, S. Noguchi, S. Kiyama, S. Tsuda, and S. Nakano, "Lateral grain growth of poly-si films with a specific orientation by an excimer laser annealing method," *Japanese journal of applied physics*, vol. 32, no. 12S, p. 6190, 1993.

[69] G. Anderson, J. Boyce, D. Fork, R. Johnson, P. Mei, and S. Ready, "Characterization of the substrate interface of excimer laser crystallized polycrystalline silicon thin films," in *MRS Proceedings*, vol. 343, p. 709, Cambridge Univ Press, 1994.

[70] D. P. Gosain, A. Machida, T. Fujino, Y. Hitsuda, K. Nakano, and J. Sato, "Formation of (100)-textured si film using an excimer laser on a glass substrate," *Japanese journal of applied physics*, vol. 42, no. 2B, p. L135, 2003.

[71] M. He, R. Ishihara, W. Metselaar, and K. Beenakker, "¡ 100¿-textured self-assembled square-shaped polycrystalline silicon grains by multiple shot excimer laser crystallization," *Journal of applied physics*, vol. 100, no. 8, p. 083103, 2006.

[72] D. Fork, G. Anderson, J. Boyce, R. Johnson, and P. Mei, "Capillary waves in pulsed excimer laser crystallized amorphous silicon," *Applied physics letters*, vol. 68, no. 15, pp. 2138–2140, 1996.

[73] J. Sipe, J. F. Young, J. Preston, and H. Van Driel, "Laser-induced periodic surface structure. i. theory," *Physical Review B*, vol. 27, no. 2, p. 1141, 1983.

[74] J. F. Young, J. Preston, H. Van Driel, and J. Sipe, "Laser-induced periodic surface structure. ii. experiments on ge, si, al, and brass," *Physical Review B*, vol. 27, no. 2, p. 1155, 1983.

[75] R. Carluccio, J. Stoemenos, G. Fortunato, D. Meakin, and M. Bianconi, "Microstructure of polycrystalline silicon films obtained by combined furnace and laser annealing," *Applied physics letters*, vol. 66, no. 11, pp. 1394–1396, 1995.

[76] W. Dash and R. Newman, "Intrinsic optical absorption in single-crystal germanium and silicon at 77 k and 300 k," *Physical review*, vol. 99, no. 4, p. 1151, 1955.

[77] K. Murakami, K. Takita, and K. Masuda, "Measurement of lattice temperature during pulsed-laser annealing by time-dependent optical reflectivity," *Japanese Journal of Applied Physics*, vol. 20, no. 12, p. L867, 1981.

[78] S. Stiffler, M. O. Thompson, and P. Peercy, "Supercooling and nucleation of silicon after laser melting," *Physical Review Letters*, vol. 60, no. 24, p. 2519, 1988.

[79] V. K. Wong and J. S. Im, "to be submitted,"

[80] G. Hasson, J.-Y. Boos, I. Herbeuval, M. Biscondi, and C. Goux, "Theoretical and experimental determinations of grain boundary structures and energies: Correlation with various experimental results," *Surface Science*, vol. 31, pp. 115–137, 1972.

[81] J. F. Young, J. Sipe, and H. Van Driel, "Laser-induced periodic surface structure. iii. fluence regimes, the role of feedback, and details of the induced topography in germanium," *Physical Review B*, vol. 30, no. 4, p. 2001, 1984.

[82] R. Jaccodine, "Surface energy of germanium and silicon," *Journal of The Electrochemical Society*, vol. 110, no. 6, pp. 524–527, 1963.

[83] S. R. Phillpot and D. Wolf, "Grain boundaries in silicon from zero temperature through melting," *Journal of the American Ceramic Society*, vol. 73, no. 4, pp. 933–937, 1990.

[84] Y. Tu and J. Tersoff, "Structure and energetics of the si-sio 2 interface," *Physical review letters*, vol. 84, no. 19, p. 4393, 2000.

[85] V. V. Gupta, H. Jin Song, and J. S. Im, "Numerical analysis of excimer-laser-induced melting and solidification of thin si films," *Applied physics letters*, vol. 71, no. 1, pp. 99–101, 1997.

[86] J. P. Leonard, *Nucleation rate measurement in the Si-SiO2 thin film system*. 2000.

[87] J. Leonard and J. S. Im, "Stochastic modeling of solid nucleation in supercooled liquids," *Applied Physics Letters*, vol. 78, no. 22, pp. 3454–3456, 2001.

[88] G. Jellison Jr and D. Lowndes, "Measurements of the optical properties of liquid silicon and germanium using nanosecond time-resolved ellipsometry," *Applied Physics Letters*, vol. 51, no. 5, pp. 352–354, 1987.

[89] Y. Wang, M. D. Chahal, J. J. Wang, A. B. Limanov, A. M. Chitu, and J. S. Im, "Analysis of si-sio2 interfacial-energy hierarchy via mixed-phase solidification of si films on sio2," *MRS Proceedings*, vol. 1770, p. 55–60, 2015.

[90] H. Kim and J. S. Im, "Optimization and transformation analysis of grain-boundary-location-controlled si films," *MRS Online Proceedings Library Archive*, vol. 397, 1995.